Transition of Solar Wind Turbulence from MHD to Kinetic Scales

by

Daniel Vech

A dissertation submitted in partial fulfillment
of the requirements for the degree of
Doctor of Philosophy
(Climate and Space Sciences and Engineering)
in The University of Michigan
2020

Doctoral Committee:

Professor Justin C. Kasper, Chair
Professor Mark Kushner
Associate Research Scientist Jim Raines
Professor James A. Slavin

Daniel Vech
dvech@umich.edu
ORCID iD: 0000-0003-1542-1302

ACKNOWLEDGMENTS

Firstly, I would like to thank my advisor Justin Kasper for giving me this opportunity to join his research group and supporting me throughout my graduate studies. It was a very exciting period to work under his guidance as I could follow the final preparation of Parker Solar Probe and learn about what it actually takes to build and launch a spacecraft. He provided critical feedback and constructive ideas, which significantly helped to improve the quality of my papers, and at the same time he gave me a lot of freedom to spend a significant amount of time on ideas I found promising.

I am also grateful to Kristopher Klein who was always available to help me with my questions and provided many excellent ideas. I am thankful for Alfred Mallet for offering me an exciting project to test the predictions of his recent paper, which has turned out to be potentially the most important result in this dissertation. I would like to thank the assistance of Mike Stevens and Tony Case for providing support with Parker Solar Probe data analysis. As for the mentors prior to my PhD, I would like to thank Chris Chen for introducing me to the study of solar wind turbulence, which ultimately led me to Michigan. Finally, I would like to acknowledge the financial support of the Regents Fellowship and the NASA Earth and Space Science and Technology Program Grant (80NSSC19K1430).

TABLE OF CONTENTS

LIST OF FIGURES

FIGURE

LIST OF TABLES

TABLE

ABSTRACT

Turbulence is a ubiquitous process in space plasmas that could potentially explain the large temperatures in many astrophysical systems such as the solar corona and solar wind. Turbulent fluctuations of the magnetic field occur over a wide range of spatial scales, which are usually classified as the outer scale, magnetohydrodynamic (MHD) scale and kinetic scale (including ion and electron scales). The outer scale feeds energy into the turbulent cascade that is transferred through MHD scales without dissipation. At kinetic scales the fluctuations undergo a major transition: conservation of energy across scales breaks down, heating mechanisms start operating and the dispersion relation of fundamental wave modes change. In this dissertation we analyze *in situ* solar wind observations from Wind and Parker Solar Probe to characterize the physical mechanisms that operate in the turbulent cascade at the connection of MHD and kinetic scales.

1) We present the first statistical study on stochastic proton heating in the solar wind and identify the critical gyroscale turbulence amplitude when the first adiabatic invariant is violated and perpendicular heating takes places. Our results suggest that stochastic heating operates 76% of the time at 1 AU meaning that it has significant contribution to the non-adiabatic temperature profile of the solar wind.

2) The precise scale where MHD turbulence transitions into the kinetic range is a matter of considerable debate. Recent turbulence models suggested that current sheetlike structures form in the inertial range and get disrupted when the timescale of the tearing mode instability is shorter than the eddy turnover time. Our results suggest that these models can explain the ion-scale spectral break of the magnetic energy spectrum in 41% of the time. We also find that the disruption process may generate large amplitude ion-scale coherent structures.

3) Very little is known about the transition of proton velocity fluctuations from MHD to kinetic scales due to the scarcity of available measurements. We use a special operation mode of the Faraday Cup onboard Parker Solar Probe and develop a novel approach to study high frequency (> 1 Hz) velocity fluctuations and their correlation with magnetic fields. Our results imply that the highly Alfvénic nature of the turbulence breaks down near the ion-scale spectral break potentially due to the demagnetization of protons and the onset of kinetic effects.

CHAPTER 1

Introduction

1.1 Turbulent cascade theory

Turbulence is a ubiquitous process in the Universe, which refers to the chaotic motion of fluid elements in time and space. Some of the basic properties of turbulence such as formation of unsteady vortex structures were recognized even by da Vinci, however centuries later turbulence is still among the most important unsolved problems in classical physics (Matthaeus and Velli, 2011).

The onset of turbulence in neutral fluids was first quantitatively studied by Reynolds (1883) using a simple water-pipe experiment. Reynolds parameterized the geometry of the flow using the ratio of the inertial and viscous forces ($Re = uL/\nu$, where u is the speed of the fluid element, L is the characteristic scale and ν is the kinematic viscosity). When Re was around 2000 the stream lines were stationary and ran parallel to the axis of the pipe. Once Re reached approximately 4000, the flow became time dependent, the injected stream of dye mixed with the water in a chaotic manner and vortices formed at many size scales, which marked the onset of turbulence.

The next milestone in our understanding of turbulence was the idea of the energy cascade, which was proposed by Richardson (1922). In this concept turbulence is made of eddies, which are broadly defined as turbulent motion at a particular size scale. Kinetic energy is injected into the turbulent cascade through a production mechanism at the scale of the largest eddies. These eddies break up and continuously transfer their energy by inviscid processes to smaller eddies. This process continues until the Reynolds number becomes small enough, and the kinetic energy

of the eddies can dissipate at the smallest scales (Pope, 2001).

A few decades later Kolmogorov developed a more rigorous concept of turbulence and presented his findings known as the "Kolmogorov hypotheses" (Kolmogorov, 1941), which are summarized based on Pope (2001) and are illustrated in Figure 1.1. The first Kolmogorov hypothesis suggests that at sufficiently high Reynolds number, the small-scale turbulent motions ($l << l_0$, where l_0 is the size of the largest eddies, which are comparable to the scale of the flow itself) are statistically isotropic. In hydrodynamic turbulence the large eddies are anisotropic and are affected by the mean flow field and boundary conditions, however this directional bias is lost as the energy of the fluctuations is transferred to successively smaller scales.

The statistically universal state of the small-scale turbulence is controlled by the kinematic viscosity and the rate of energy transfer toward smaller scales. It is important to point out that the rate of dissipation (ϵ) is determined by the energy, which is injected into the turbulent system (τ) hence $\epsilon \approx \tau$. If the constant rate of energy across scales was not true, energy would accumulate on a specific scale. Kolmogorov's second hypothesis states that in every turbulent flow at sufficiently high Reynolds number, the statistics of the small-scale motions ($l < l_{EI}$, where is l_{EI} a length scale that is between the anisotropic eddies and the smallest isotropic eddies) have a universal form that is uniquely determined by ν and ϵ. In the universal equilibrium range the timescale of the eddies (defined by the ratio of their characteristic scale and velocity) is small compared to the time scale of the anisotropic eddies therefore these small eddies adopt rapidly to maintain balance with the energy-transfer rate from the injection scale. As the bulk of the kinetic energy is contained in eddies with $l > l_{EI}$, it is called the energy-containing scale.

Finally, Kolmogorov's third hypothesis proposes that in every turbulent flow at sufficiently high Reynolds number, the statistics of the motions of scale l in the range of $l_0 \gg l \gg \eta$ (where η is the smallest dissipative scale) have a universal form that is uniquely determined by ϵ, independent of ν. The universal equilibrium range is split into two subranges at l_{DI}, which are the dissipation range and the inertial range. In the inertial range the motion of eddies is controlled by inertial effects and the role of viscous effects is negligible. In contrast, eddies in the dissipation range are

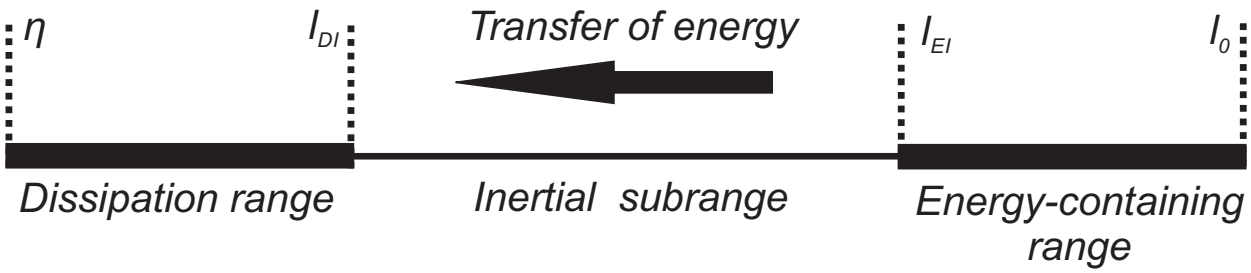

Figure 1.1: Illustration of the energy cascade and relevant length scales based on Pope (2001).

affected by viscosity. Kolmogorov predicted that the distribution of kinetic energy in the inertial range is $E(k) \sim \epsilon^{2/3} k^{-5/3}$ where k is the wavenumber ($k = 2\pi/l$). This scaling is widely observed in hydrodynamic turbulence and is one of the cornerstone assumptions of turbulence theory.

More than half a century after the seminal works of Kolmogorov, several fundamentally important questions about the turbulent cascade are still debated. In particular, what mechanisms operate at l_{DI} that lead to dissipation and what set the scale that separates the inertial and dissipation ranges in neutral fluids? Understanding the transition of turbulence from the inertial to the dissipation range represents a major challenge since at these small scales the signal of measurements is weak and is easily contaminated by the background noise. Furthermore, high Reynolds number fluids requires significant computation capabilities, which are often far beyond those available today (Martinez et al., 1997; Vassilicos, 2015).

1.2 Space plasma turbulence

Turbulence has been found to be fundamentally important beyond the terrestrial environment as well: space plasma turbulence influences a wide range of physical processes such as angular momentum transport in accretion disks (Balbus and Hawley, 1998), it plays a role in galactic magnetic field amplification (Kulsrud and Zweibel, 2008), it affects the thermal conduction in galaxy clusters (Schekochihin et al., 2008) and formation of stars (McKee and Ostriker, 2007). Turbulence on scales much larger than the proton gyroradius ($\rho_i = v_\perp/\Omega_i$ where $v_\perp$ is the ion's perpendicular thermal speed and Ω_i is the ion's gyrofrequency) is generally described with the framework of

magnetohydrodynamics (MHD), which is a single fluid, low frequency, long wavelength description of the plasma dynamics of the solar wind, magnetosphere, corona and interstellar medium (e.g Matthaeus and Velli, 2011; Biskamp, 2003). When the scale of the turbulent fluctuation is comparable to ρ_i known as kinetic scales, the conservation of energy across scales breaks down and heating takes place. The dissipation of the energy carried by turbulent fluctuations could potentially explain the large temperatures in many astrophysical systems in particular the solar corona and solar wind (see review by Chen, 2016) therefore understanding the dynamics of the turbulent cascade at the connection of MHD and kinetic scales is an outstanding problem in space plasma physics.

The energy cascade and Kolmogorov hypotheses described in Chapter 1.1 are important concepts in both hydrodynamic and space plasma turbulence as well, however some of the underlying assumption of these theories do not apply to MHD plasmas. One of the striking differences is that in space plasmas the eddies become progressively more anisotropic toward smaller scales, which has fundamentally important implications for the dynamics of the cascade (see review by Horbury et al., 2012). This feature of the turbulence is important for the results discussed in Chapter 5 and 6. Another major difference is that hydrodynamic systems can be treated locally since the large-scale velocity can be removed with the Galilean transformation. In contrast, in MHD turbulence the magnetic field of large-scale eddies cannot be removed by transforming into a moving reference frame. This means that the small-scale eddies experience the effect of the large-scale magnetic field acting as a guide field (e.g. Mason et al., 2006).

The solar wind is an excellent laboratory to study space plasma turbulence for several reasons. First of all, *in situ* measurements are available from the solar wind thus a wealth of electromagnetic and plasma data could be used to test various turbulence models. Second, in the solar wind at 1 AU the relevant wave modes (such as parallel propagating Alfvén waves) are typically much slower than the bulk speed of the flow therefore the Taylor's hypothesis (Taylor, 1938) is used to interpret fluctuations of the magnetic field, velocity and other physical quantities as spatial changes in the convected plasma. Another important feature of the solar wind is that the plasma parameters such

as magnitude of the magnetic field and proton thermal speed show significant variations hence statistical studies allow us to distinguish competing theories more easily and the obtained results can also be extrapolated to other astrophysical systems (such as galaxy clusters), where *in situ* measurements are not possible (Chen, 2016).

1.3 Spectra of solar wind turbulence

Magnetic field fluctuations in the solar wind occur on a very broad frequency range spanning from 10^{-6} to several hundreds of Hz. The origin of the turbulent spectrum is not well understood: remote sensing observations from the Hinode spacecraft suggest the presence of Alfvén waves in the chromosphere, which have sufficient wave power to drive the solar wind (De Pontieu et al., 2007). However, the typical wave periods and amplitudes are in the ranges of 100-500 seconds and 20-50 km/s, which cannot explain the observations of a broadband turbulent spectrum with frequencies as low as 10^{-5} Hz. Matthaeus and Goldstein (1986) and Matthaeus et al. (2007) argued that magnetic reconnection related processes in the photosphere and lower corona may results in the observed low frequency spectrum. In contrast, several studies suggested that nonlinear interaction between inward and outward propagating waves may generate the broadband turbulent spectrum (Velli et al., 1989; Verdini and Velli, 2007; Perez and Chandran, 2013).

An example of the power spectra of magnetic fluctuations in the solar wind is shown Figure 1.2 (Kiyani et al., 2015), which illustrates the amount of magnetic energy at each scale. In the figure the frequency axis can be converted into a spatial scale as $l = V_{sw}/2\pi f$ where V_{sw} is the speed of the solar wind and f is frequency in the spacecraft frame. The energy spectrum of the magnetic fluctuations is divided into four different ranges where different physical mechanisms are responsible for the transfer of energy toward smaller scales.

Outer scale

The outer scale is an energy reservoir that continuously feeds the turbulent cascade. The typical frequency range of the outer scale is $f < 10^{-3}$ Hz at 1 AU. The spectral index of the power

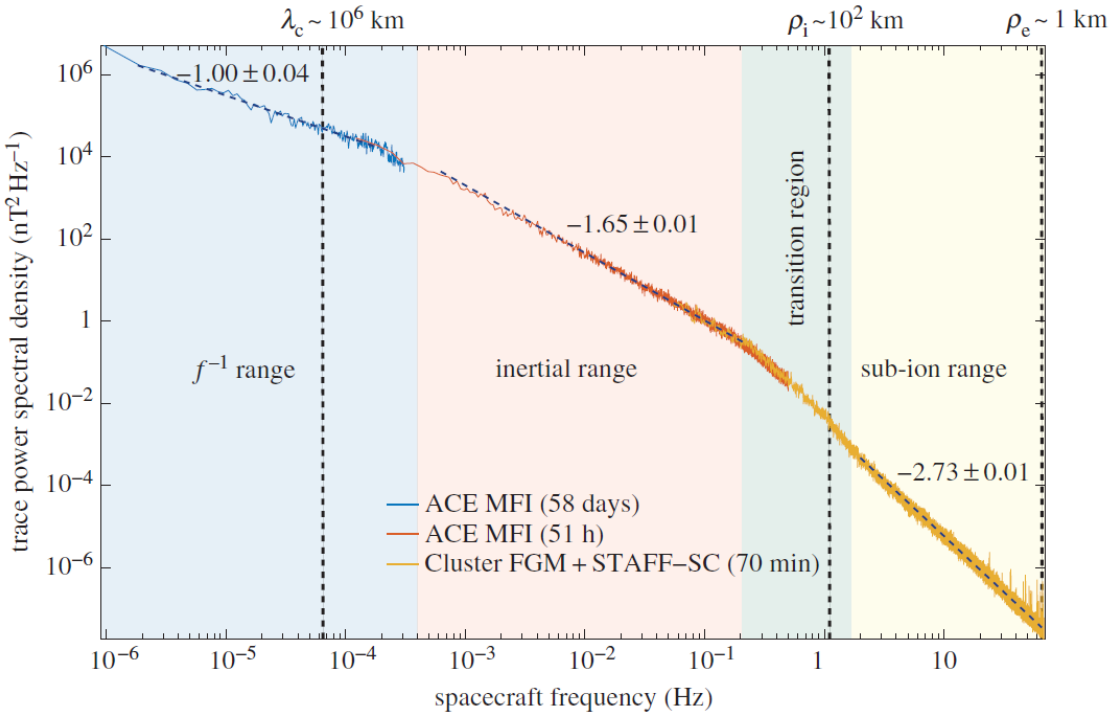

Figure 1.2: Example of the turbulent spectra of magnetic fluctuations in the solar wind (Kiyani et al., 2015).

spectrum is -1 in this range hence it is frequently called 1/f spectrum. In the 1/f spectrum the correlation length (λ_c) corresponds to the spatial scale above which the fluctuations are entirely disconnected from their solar origin and are produced by the in situ dynamics of the turbulent cascade. The typical value of λ_c at 1 AU is approximately $6 \cdot 10^{-5}$ Hz (Kiyani et al., 2015).

Inertial range

At approximately 10^{-3} Hz the spectrum steepens and the turbulent fluctuations reach the inertial range, where the turbulent energy cascades toward small scales without dissipation (e.g. Podesta and Bhattacharjee, 2010). The spectral index of the inertial range is close to -5/3 corresponding to the Kolmogorov energy spectrum. The inertial range includes a mixture of incompressible and compressible fluctuations where incompressible ones have over 90% contribution to the total wave power (Horbury et al., 1995). The incompressible fluctuations are Alfvénic while the compressible fluctuations are primarily slow mode waves with only minor contribution coming from fast mode waves, which damp more rapidly than slow mode waves as the solar wind

propagates away from the Sun (e.g. Barnes, 1968; Howes et al., 2012).

A fundamentally important property of MHD scale magnetic fluctuations is the anisotropy. Early models of MHD turbulence were derived upon the assumption that the magnetic fluctuations are isotropic, in which case the corresponding spectral index of the inertial range is -3/2 and the energy of the magnetic and velocity fluctuations are equal (Iroshnikov, 1964; Kraichnan, 1967). It was first established by Montgomery and Turner (1981) that MHD turbulence is anisotropic with respect to the mean (DC) magnetic field. Goldreich and Sridhar (1995) quantified the anisotropy of the eddies and suggested that the scaling between parallel (l, field aligned) and perpendicular (λ) components is $\lambda^{-3/2} \sim l$ (see Figure 1.3a). In this model the shape of the eddy resembles to a filament in the $\lambda \Rightarrow 0$ limit. Numerous spacecraft observations showed good agreement with the Goldreich and Sridhar (1995) model (e.g. Horbury et al., 2008; Podesta et al., 2009; Chen et al., 2011)

Boldyrev (2006) argued that filamentlike eddies are, in fact, nonrealizable and suggested that the eddies have three-dimensional anisotropy thus their shape resembles to ribbons or current sheets (see Figure 1.3b). The anisotropy is measured along the magnetic field (l), in the direction of the perpendicular field fluctuations (η) and perpendicular to both (λ). Their magnitudes are $l > \eta > \lambda$ and $\eta \sim \lambda^{3/4}$ implying that the eddies become sheet-like structures when $\lambda \Rightarrow 0$. Both numerical (Dong et al., 2014; Verdini and Grappin, 2015) and observational studies (Chen et al., 2012; Vech and Chen, 2016) have found evidence for the three-dimensional nature of the eddies.

Current sheets whose aspect ratio decreases toward smaller scales are not sustainable and tend to be tearing-unstable (e.g. Schekochihin, 2019). The onset of the tearing mode instability depends on the eddy turnover time (τ_{nl}, the time it takes for an eddy to transfer its energy toward smaller scales) and the time scale on which the fastest growing tearing mode can be triggered (τ_d). If the tearing mode can develop ($\tau_{nl} > \tau_d$) then it breaks up the forming current sheets into islands (Uzdensky and Loureiro, 2016). Mallet et al. (2017) and Loureiro and Boldyrev (2017) parameterized the scale where the disruption may occur and argued that it causes a break in the turbulent spectrum and abruptly ends the inertial range. Chapter 5 and 6 will present a detailed discussion of these

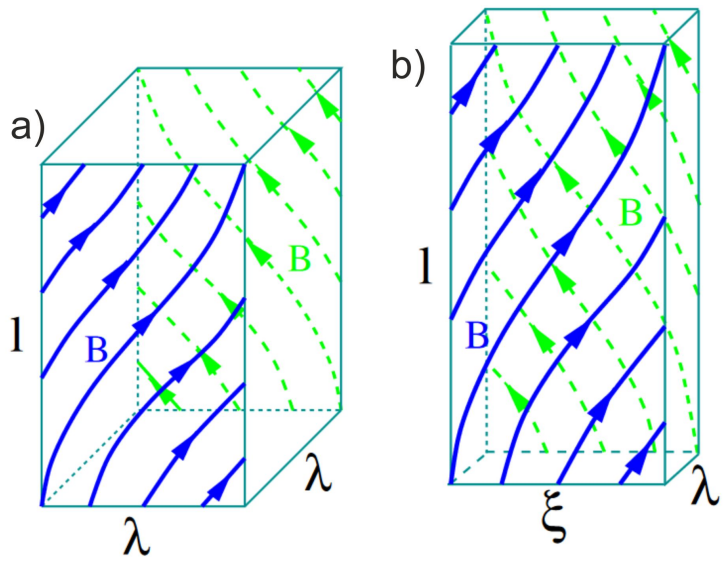

Figure 1.3: Illustration of the shape of the eddies in the (a) Goldreich & Sridhar (1995) and (b) Boldyrev (2006) models, respectively (Boldyrev, 2006).

models and the predictions will be tested based on a statistical approach.

Transition region

When the turbulent fluctuations reach the scales comparable to the ion inertial length ($d_i = V_A/\Omega_i$ where V_A is the Alfvén speed) and ρ_i (approximately 0.1-1 Hz in the spacecraft frame at 1 AU), the fluid picture of MHD breaks down and the turbulent spectrum undergoes a transition into the kinetic range where dissipation takes place. Although d_i and ρ_i are the most frequently cited parameters to explain the steepening of the turbulent spectra (e.g. Galtier et al., 2000; Bruno and Telloni, 2015), previous studies (Chen et al., 2014) showed that the break scale has good agreement with ρ_i and d_i only in the $\beta \gg 1$ and $\beta \ll 1$ limits (where β is the ratio of proton thermal pressure to magnetic pressure), respectively, which rarely occur in the solar wind at 1 AU where $\beta \approx 1$. Therefore it has remained an open question what controls the break scale in typical solar wind conditions.

In the transition range fast mode waves become whistler waves, perpendicular Alfvén waves become kinetic Alfvén waves (KAW) and parallel Alfvén waves become the ion cyclotron waves. Some previous simulations found signatures of whistler waves in the kinetic range (Stawicki et al., 2001; Saito et al., 2008), however the vast majority of solar wind studies agree that KAW turbu-

lence has the main contribution to the total wave power (e.g Bale et al., 2005; Chen et al., 2013). In particular, recent high frequency measurements by the Magnetospheric Multiscale Mission (MMS) found anti-correlation between electron density and the magnitude of magnetic field fluctuations, which is consistent with kinetic Alfvén wave turbulence (Chen and Boldyrev, 2017).

In contrast to the inertial range where the spectral index shows minor variations, the spectral index in the kinetic scale is clearly non-universal and is in the range of -2 and -4 (e.g. Alexandrova et al., 2009). The solar wind dependence of the spectral index is not well understood. For example, early studies suggested that the spectral index has anti-correlation with the energy of the turbulent cascade thus higher energy cascade rate leads to steeper spectra (Smith et al., 2006). The presence of wave activity (e.g. Jian et al., 2009; Wicks et al., 2016) and coherent structures can significantly distort the shape of the magnetic field spectra on kinetic scales. A recent case study by Lion et al. (2016) suggested that the presence of large amplitude ion-scale coherent structures may lead to unusually steep (≈ -4) spectral indices. The mechanism that generates those structures is a matter of considerable debate: several studies argued that coherent structures are passively advected from the Sun (e.g. Borovsky, 2008) while others argued the importance of local generation by non-linear processes (e.g Salem et al., 2009). Disruption of current sheetlike structures may locally generate coherent structures in the solar wind. In Chapter 6 we will study the correlation between the parameter regime where the Mallet et al. (2017) reconnection model may operate, the occurrence of ion-scale coherent structures and the steepening of the turbulent spectra.

In addition to electromagnetic field measurements, studying high frequency velocity fluctuations is also necessary to reveal the mechanisms that operate near the ion-scale spectral break. Previously, the Spektr-R spacecraft (Šafránková et al., 2013, 2015, 2016) provided reliable velocity spectra in the solar wind up to 2 Hz, however the spacecraft did not have an operating magnetic field instrument therefore it was not possible to measure the coupling between kinetic and magnetic energy across the ion-scale spectral break. More recently, the Fast Plasma Investigation (FPI, Pollock et al., 2016) of MMS measures power spectra of proton velocity in the magnetosheath up to approximately 1 Hz before reaching the noise floor (e.g. Chen and Boldyrev, 2017). It is

important to note that the plasma instruments of MMS were optimized for high temperature magnetospheric plasmas and measurements of cold solar wind protons typically include artifacts (see Bandyopadhyay et al., 2018). In Chapter 7 we present a novel data analysis technique with Parker Solar Probe data, which allows us to resolve proton velocity fluctuations in the solar wind above the ion-scale spectral break and measure its correlation with the electromagnetic field. This technique is fundamentally important to understand kinetic scale turbulence in the inner heliosphere and solar corona.

Electron scale

Electron scale ($f > 30$ Hz) is the least well understood part of the turbulent spectrum, which is due to the fact few high cadence magnetic field observations are available from the solar wind. Sahraoui et al. (2009) presented the first results on the high frequency part (up to 100 Hz) of the turbulent spectrum using merged fluxgate and search coil magnetometer data from the Cluster spacecraft. The obtained turbulent spectrum for the parallel (compressive) and perpendicular (incompressible) components of the fluctuations are shown in Figure 1.4. Sahraoui et al. (2009) found for the first time that the magnetic energy continues cascading nearly two decades after the ion-scale spectral break; they also found evidence for a second break point in the spectrum, which showed good agreement with the electron gyroradius (and also the electron inertial length). The observations were consistent with the hypothesis that the energy of the fluctuations is carried by oblique kinetic Alfvén waves as opposed to whistler waves.

The search coil magnetometers of current and future missions such as MMS, Parker Solar Probe, Solar Orbiter and Debye will make it possible to study the final stage of the turbulent fluctuations and understand in detail how dissipation mechanisms operate at electron scale.

1.4 Heating mechanisms

Following the transition from MHD to kinetic scales the energy of magnetic fluctuations is dissipated by several heating mechanisms including Landau and transit-time damping, cyclotron

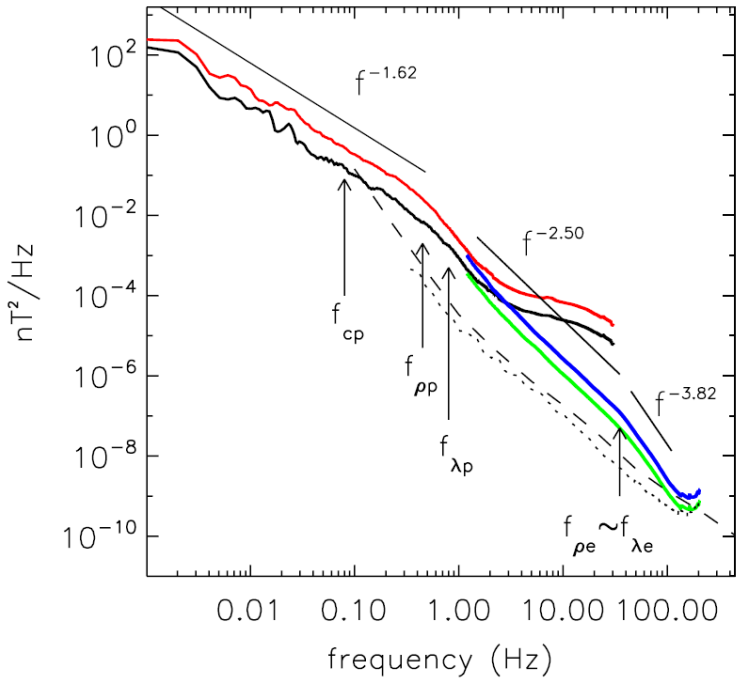

Figure 1.4: First measurements of the electron scale magnetic fluctuations in the solar wind for the parallel (black and green lines) and perpendicular spectrum (red and blue lines), respectively (Sahraoui et al., 2009)

damping, stochastic heating and magnetic reconnection. These mechanisms usually operate simultaneously therefore it is difficult to quantify their relative contribution to heating of the solar wind and solar corona. In the following sections four main heating mechanisms are briefly described.

Landau and transit-time damping

Landau damping (also known as phase mixing) is a mechanism that absorbs the energy of electromagnetic oscillations in a collisionless plasma (Landau, 1946). The physical basis of this mechanisms is the following: a first-order linearly or elliptically polarized Alfvén generates a second-order gradient in the magnetic field pressure. This pressure gradient drives a second-order ion sound wave and an associated longitudinal electric field (Hollweg, 1971). Wave-particle interaction occurs when the phase speed of the particles can resonate with this longitudinal electric field. Particles whose phase speed is slightly above the phase speed of the electric field perturbation will lose energy and the opposite is true for particles slightly slower than the phase speed of the wave. In Maxwellian plasmas there are more particles whose phase speed is slightly below

the phase speed of the electric field perturbation therefore on average the electric field is damped (Fitzpatrick, 2008). Direct measurement of Landau damping in space plasmas was first reported by Chen et al. (2019) using MMS data in Earth's magnetosheath.

Transit-time damping is due to resonance of particles with the parallel magnetic field (e.g. the compressible perturbation) of magnetosonic fast mode waves and is electromagnetic in nature (Aschwanden, 2006). This process is the magnetic equivalent of Landau damping and is called transit-time damping because the transit time of a particle across a wavelength is equal to the period of the wave. Similar to Landau damping, transit-time damping leads to increase of the parallel energy of particles at the expense of wave damping. It is important to note that the operation of both Landau and transit-time damping depend on β: for plasmas with $\beta \ll 1$, ion thermal speeds $\ll V_A$ thus ions cannot satisfy the resonance condition for these heating mechanisms (Chandran et al., 2010).

Cyclotron damping

In the case of cyclotron damping the electric field of the wave is perpendicular to the direction of the magnetic field and the particle drift and accelerates the particle perpendicularly to the drift direction (Miyamoto, 2006). Several early studies suggested that cyclotron damping may be the leading mechanism for heating of protons and heavy ions in the solar wind and solar corona (e.g. Coleman Jr, 1968; Schwartz et al., 1981). These findings were supported by remote sensing observations suggesting that heavy ions such as O^{+5} in the solar corona (Kohl et al., 1998) have significantly larger perpendicular temperatures than parallel in agreement with the predictions of ion cyclotron damping. However, it is important to note that the resonant ion-wave interactions gradually decrease if the parallel wavevector component ($k_{||}$) of an Alfvén-cyclotron wave becomes smaller (e.g. Marsch, 2006). Several numerical studies (e.g. Cranmer and Van Ballegooijen, 2003) argued that in the solar corona the energy cascade is highly anisotropic meaning that the perpendicular fluctuations have significantly higher power than the parallel ones ($k_\perp \gg k_{||}$), which is insufficient to heat protons and heavy ions. Solar wind observations at 1 AU (Chen et al., 2010) imply that at the scale where Alfvén waves undergo cyclotron damping (approximately the

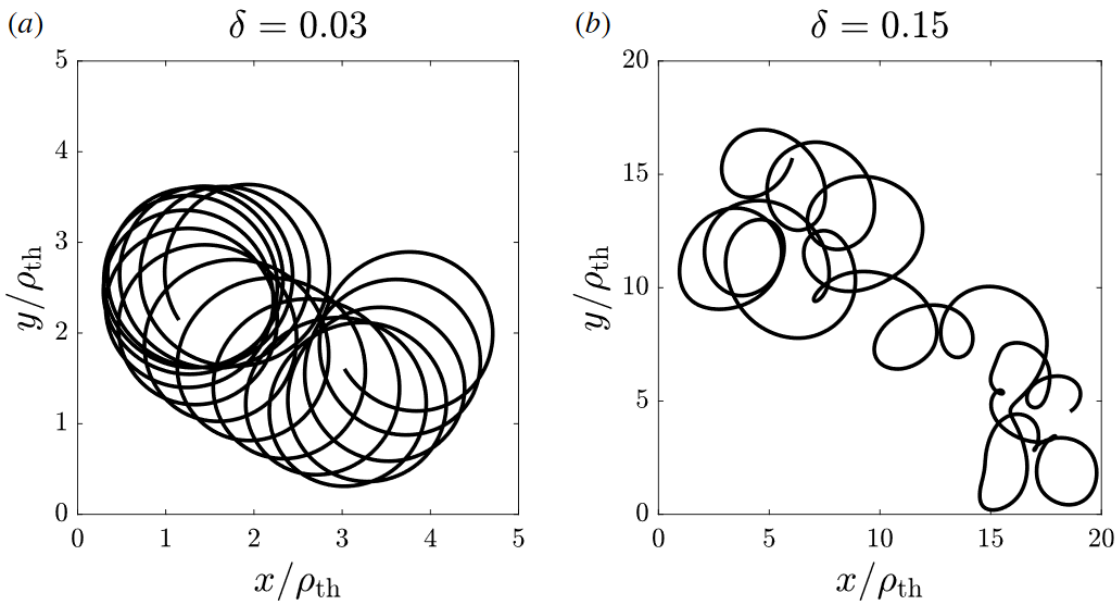

Figure 1.5: Simulation of a proton's trajectory for (a) low and (b) high gyroscale turbulence amplitude ($\delta = \delta B_\rho / B_0$) (Hoppock et al., 2018).

ion-scale spectral break) the energy cascade is highly anisotropic in the perpendicular direction thus cyclotron damping is not expected to be an efficient mechanism removing energy from the magnetic fluctuations.

Stochastic heating

Stochastic ion heating occurs when the amplitude of electromagnetic fluctuations at gyroscale exceed a critical threshold and the first adiabatic invariant of particle motion is violated (e.g. McChesney et al., 1987), which results in diffusion of energy perpendicular to the magnetic field (Chandran et al., 2010). Figure 1.5 shows the trajectory of a proton interacting with randomly phased Alfvén waves and kinetic Alfvén waves, where $\delta = \delta B_\rho / B_0$ is the ratio of the gyroscale turbulence amplitude to the background DC magnetic field (Hoppock et al., 2018). When δ reaches a critical amplitude, the periodic gyromotion of the proton is disrupted and the particle's trajectory becomes chaotic. Several aspects of stochastic heating in the solar wind are not well understood. In particular, what is the critical gyroscale turbulence amplitude? What fraction of the time does stochastic heating operate in the solar wind? Previous studies (e.g. Bourouaine and Chandran, 2013) analyzed stochastic heating in only a few solar wind streams thus a comprehensive statis-

tical study is still missing. In Chapter 3 and 4 we test the stochastic heating model of Chandran et al. (2010), which makes predictions about the relevant heating mechanisms as a function of β and gyroscale turbulence amplitude.

Magnetic Reconnection

Magnetic reconnection is a universal process leading to energy conversion in plasmas (Yamada et al., 2010). The idea that thin current sheets naturally form and reconnect in MHD turbulence was proposed over 30 years ago by Matthaeus and Lamkin (1986) and Politano et al. (1989). However, direct measurements of turbulent reconnection in space plasmas presented a major challenge and it was finally achieved with the Cluster spacecraft launched in 2004. Retinò et al. (2007) showed the first evidence for magnetic reconnection in the turbulent magnetosheath downstream Earth's bow shock. Several signatures of reconnection were identified such as conversion of magnetic energy into kinetic energy, super-Alfvénic jets of ions and electrons. Later, Sundkvist et al. (2007) suggested that reconnecting current sheets are abundant in the magnetosheath and heating rate from reconnecting thin current sheets may exceed the significance of wave damping. More recently, Phan et al. (2018) used high cadence measurements from MMS and showed the first evidence for electron-only reconnection, which is not embedded in a larger ion-scale current layer. Near the reconnecting current sheet they found signatures of oppositely directed super-ion-Alfvénic electron jets, parallel electric fields and enhanced magnetic-to-particle energy conversion. Electron-only reconnection may play an important role in turbulent energy transfer and dissipation below ion-scales.

In addition to the observational studies, analysis of numerical simulations has also made significant progress toward the characterization of turbulent reconnection (e.g. Servidio et al., 2009, 2011), however the physical mechanisms that lead to the formation of current sheetlike structures in turbulent plasmas are still not well understood. A potential explanation is that MHD scale magnetic fluctuations have the tendency to align themselves into current sheetlike structures with increasing aspect ratio toward smaller scales as predicted by Boldyrev (2006). This idea served as the basis of the turbulent models of Mallet et al. (2017); Loureiro and Boldyrev (2017) making

predictions about the scale where the forming current sheets reconnect. In Chapters 5 and 6 we will test these models and study the effect of turbulent reconnection on the magnetic energy spectra.

1.5 Guiding Science Questions

Understanding the dissipation of turbulent energy is one of the central problems in space plasma physics. In this dissertation new results are presented about the connection between the MHD and kinetic ranges of the turbulent cascade based on Wind and Parker Solar Probe measurements. Below are the three main science questions that we address in the subsequent chapters to improve our understanding of solar wind turbulence.

Q1. How does stochastic ion heating operate in the solar wind?

Both remote sensing and *in situ* measurements have suggested that stochastic heating is among the leading candidates to explain heating of the solar corona and solar wind. Despite its importance, the critical gyroscale turbulence amplitude at which the ion's orbit becomes chaotic has not been measured in the solar wind previously. We will conduct the first comprehensive study of stochastic ion heating in the solar wind using more than 14 years of Wind measurements, which will allow us to study proton and electron temperature variations both as a function of β and the turbulence amplitude and therefore distinguish stochastic heating from other dissipation mechanisms such as Landau damping.

Q2. What controls the ion-scale break of the turbulent power spectrum?

There is no well accepted model predicting the ion-scale spectral break as a function of solar wind parameters. Previous studies have tested the ion inertial length (Galtier et al., 2000; Chen et al., 2014), proton gyroradius (Chen et al., 2014) and proton cyclotron resonance scale (Bruno and Trenchi, 2014; Woodham et al., 2018). Very recently, the concept of tearing mode instability has gained significant interest and several numerical studies argued that disruption of current

sheetlike structure in the inertial range may induce a break in the turbulent spectrum (Mallet et al., 2017; Loureiro and Boldyrev, 2017), however no observational studies have been conducted to test these predictions. For the first time, we will study the correlation between the ion-scale spectral break and the disruption scale predicted by Mallet et al. (2017). Furthermore, we will identify signatures of small-scale, large-amplitude magnetic structures, which might be generated during the disruption process.

Q3. What are the capabilities of Parker Solar Probe's Faraday Cup instrument to study kinetic scale velocity fluctuations?

Studying the transition of velocity fluctuations from MHD to kinetic scales is a challenging problem, which requires high cadence (at least a few Hz) velocity measurements, which was only achieved by the Spektr-R and MMS spacecraft. The Faraday Cup instrument onboard Parker Solar Probe measures full proton velocity distributions with 1.14 Hz in typical operation mode and 19.6 Hz in burst mode. In the Flux Angle mode the Faraday Cup measures phase space density fluctuations in a single energy/charge window with 293 Hz cadence. This operation mode has not been used in previous missions thus the characteristic of the measurements are not well understood. We develop a new data analysis technique to convert these measurements into vector velocity components and study proton velocity fluctuations around the ion-scale spectral break. We demonstrate that this technique provides an invaluable tool to understand kinetic scale turbulence in the solar wind and solar corona.

CHAPTER 2

Methodology

In order to address the Guiding Science Questions outlined in Chapter 1.5, we have utilized *in situ* measurements from Wind and Parker Solar Probe.

2.1 Wind spacecraft

The NASA's Wind spacecraft was launched on November 1, 1994; the spacecraft orbit initially passed through the terrestrial magnetosphere until early 2004 when Wind was placed in a halo orbit around the L1 Lagrange point approximately 1.5 million km upstream of Earth (Lin et al., 1995). In the past over 25 years Wind has provided the most comprehensive set of solar wind measurements including proton, electron thermal properties and magnetic fields with only minor data gaps. In this work we used measurements of the fluxgate magnetometer, electron electrostatic analyzers and the Faraday Cup to study high frequency magnetic fluctuations and to identify the background solar wind conditions such as parallel and perpendicular (with respect to the magnetic field) proton temperatures.

2.2 Wind Faraday Cup and Electron Electrostatic Analyzer

The Solar Wind Experiment (SWE) of Wind includes two Faraday Cups pointing with 15° southward and northward from the plane of ecliptic, respectively (Ogilvie et al., 1995). The Faraday Cup measures the currents due to positive ions reaching the four collector plates. The discrim-

ination of charged particles and energy determination is based on a time-varying positive potential, which chops a selected portion of the charged particle flux. The time-varying potential is a dc-biased, 200 Hz square wave, which is generated by a modulator. The resulting waveform ranges from 150 V - 8.0 kV with 64 logarithmically-spaced bins. A capacitor integrates the chopped current from each collector plate in a fixed time interval and the resulting voltage is then converted to a digital signal. The measurement resolution of the Faraday Cup varies between 6.5% and 13%. The key parameters of the energy/charge distributions (velocity components, density, temperature) are derived with fitting to the convected bi-Maxwellian function (Kasper et al., 2006). The typical cadence of the three-dimensional velocity distributions is 92-second; 3-second onboard moments are available as well.

The electron temperature data is provided by the low and high energy electron electrostatic analyzers (EESA-L and EESA-H), which are included in the Wind 3DP experiment (Lin et al., 1995). The two instruments measure electrons in the range of a few eV to 30 keV with approximately 20% energy resolution in 20 logarithmically spaced bins. During each 3-second spin of the spacecraft the instruments cover 88 angular bins to obtain full three-dimensional energy distribution of electrons. The cadence of the onboard computed moments (velocity, temperature and density) is between 45 and 90 second (Pulupa et al., 2014; Wilson III et al., 2018).

2.3 Wind Magnetic Field Investigation

The Magnetic Field Investigation (MFI, Lepping et al., 1995) of Wind includes a dual triaxial fluxgate magnetometer, which is mounted at the tip of a 12-m boom where the noise from the spacecraft is expected to be less than 0.1 nT. The inboard sensor is at approximately 2/3 of the distance to the outboard sensor. The dual configuration provides redundancy and it allows subtraction of the dipolar part of the spacecraft field contribution to the measured magnetic field. The basic measurement principle of MFI is the following: a 15 KHz signal drives the fluxgate sensors to cyclical saturation. In the absence of an external magnetic field, no signal is generated

by the sensor. In the presence of an external field a current containing even harmonics of the drive frequency appears at the output of the sensors. From this signal a high gain integrating amplifier generates a voltage, which is proportional to the magnitude, direction and polarity of the ambient magnetic field along each of the three orthogonal sensor's axis. The typical measurement cadence of MFI is 92 ms (90% of the time) and occasionally 46 ms (8% of the time) and 184 ms (2% of the time) (Koval and Szabo, 2013). In this dissertation the calibration of Koval and Szabo (2013) was used, which removed spin tone harmonics from the time series. Studying high frequency magnetic field fluctuations requires some caution therefore in Chapter 3 we present an analysis to filter out intervals where measurements above approximately 0.3 Hz of the magnetic turbulent spectra are affected by the instrument's noise floor.

2.4 Parker Solar Probe

Parker Solar Probe (PSP) is the first spacecraft to fly into the solar corona: through the 7-year nominal mission the perihelion of the spacecraft's orbit will gradually decrease to < 10 R_S, which will allow the spacecraft to measure the young solar wind close to its source regions, which has been top-priority science goal for over five decades. The primary science objectives of the mission are to *"determine the structure and dynamics of the Suns coronal magnetic field and to understand how the corona is heated, the solar wind accelerated, and how energetic particles are produced and their distributions evolve"* (Fox et al., 2016). To accomplish these goals the spacecraft carries four instrument suites to study electromagnetic fields (Bale et al., 2016), solar energetic particles (McComas et al., 2016), thermal properties of solar wind electron, protons and α-particles (Kasper et al., 2016) and a wide-field imager to capture the three-dimensional structure of the large-scale corona (Vourlidas et al., 2016). The first perihelion of PSP was on 4^{th} November 2018 at approximately 35 R_S distance from the Sun. In Chapter 7 we analyze data from the Solar Probe Cup (SPC) and fluxgate magnetometers (MAG) therefore these instruments are briefly described in the subsequent sections.

2.5 Solar Probe Cup

SPC is a Sun-viewing Faraday Cup, which is mounted at the edge of the PSP heat shield. SPC is one of the four sensors of the SWEAP instrument suite and it measures fluxes and flow angles as a function of energy from 50 eV/q to 8 keV/q for ions and 50 eV to 2 keV for electrons with energy and angular resolution of less than 10% and 1°, respectively. The measurements are solved for velocity, density and temperature of protons and α-particles, which is crucial to determine the sources of slow and fast solar wind, trace the flow of energy heating the corona and solar wind and to understand transport and acceleration of energetic particles (Kasper et al., 2016).

SPC has three operation modes, which are the Proton Tracking (PT), Full Scan (FS) and Flux Angle mode (FA). In PT mode SPC measures the center of the proton velocity distribution function and produces 8 energy/charge measurements for each collector plate 16 times every 0.874 second. In FS mode SPC scans through 128 energy/charge windows in 0.874 seconds over the full range of SPC voltages. In Flux Angle (FA) mode the the size of the window is increased to at least 10% and is placed over the center of the proton velocity distribution function. In this operation mode the flow angle and total flux are measured 293 times per second. The FA mode has not been used in prior missions, however it has the potential to provide key measurements from the kinetic range of flow angle and total flux fluctuations, which cannot be measured in other operation modes of SPC. In Chapter 7, we describe a method to process the FA mode measurements and convert them into vector velocity fluctuations to study their correlation with the magnetic field.

2.6 FIELDS

The goal of the FIELDS instrument package is to measure DC and fluctuating components of electromagnetic fields, plasma wave spectra and polarization properties, the spacecraft floating potential and solar radio emissions (Bale et al., 2016). The magnetic fields are measured from DC to beyond the electron cyclotron frequency by two fluxgate and a search coil magnetometers. These instruments will determine the dynamics and structure of magnetic fields at the origin of

slow and fast solar wind and provide key measurements to understand the coronal processes that heat the plasma; they will also contribute to revealing the roles of shocks, magnetic reconnection and turbulence in the acceleration of energetic particles.

The fluxgate magnetometers of PSP are triaxial, wide-range, low-power and low-noise sensors, which are significantly based on the heritage from MAVEN, Van Allen Probes and STEREO missions. The bandwidth of the measurements is $\approx$ 140 Hz and the typical sampling rate is 293 Hz. The dynamic range of the instruments is +/- 65536 nT with a resolution of 16 bits. The two fluxgate magnetometers are located on a deployable boom at 1.9 m (MAGi) and 2.72 m (MAGo) from the rear deck of the spacecraft. Due to the proximity of the spacecraft the gradiometric ability of the sensors is limited to accurately remove magnetic fields generated by the spacecraft. Therefore magnetic cleanliness testing of the spacecraft and payload is particularly important.

CHAPTER 3

Nature of Stochastic Ion Heating in the Solar Wind: Testing the Dependence on Plasma Beta and Turbulence Amplitude

This chapter is taken from Vech, D., K. G. Klein, J. C. Kasper, Nature of stochastic ion heating in the solar wind: testing the dependence on plasma beta and turbulence amplitude, Astrophysical Journal Letters, DOI: 10.3847/2041-8213/aa9887, 2017.

The solar wind undergoes significant heating as it propagates away from the Sun; the exact mechanisms responsible for this heating are not yet fully understood. We present for the first time a statistical test for one of the proposed mechanisms, stochastic ion heating. We use the amplitude of magnetic field fluctuations near the proton gyroscale as a proxy for the ratio of gyroscale velocity fluctuations to perpendicular (with respect to the magnetic field) proton thermal speed, defined as ϵ_p. Enhanced proton temperatures are observed when ϵ_p is larger than a critical value ($\sim 0.019 - 0.025$). This enhancement strongly depends on the proton plasma beta ($\beta_{||p}$); when $\beta_{||p} \ll 1$ only the perpendicular proton temperature $T_\perp$ increases, while for $\beta_{||p} \sim 1$ increased parallel and perpendicular proton temperatures are both observed. For ϵ_p smaller than the critical value and $\beta_{||p} \ll 1$ no enhancement of T_p is observed while for $\beta_{||p} \sim 1$ minor increases in $T_\parallel$ are measured. The observed change of proton temperatures across a critical threshold for velocity fluctuations is in agreement with the stochastic ion heating model of Chandran et al. (2010). We find that

$\epsilon_p > \epsilon_{\rm crit}$ in 76% of the studied periods implying that stochastic heating may operate most of the time in the solar wind at 1 AU.

3.1 Introduction

The solar wind is a hot, tenuous plasma propagating away from Sun's surface. The radial expansion of the solar wind is highly non-adiabatic with the proton temperature cooling significantly slower than a spherically expanding ideal gas (e.g. Wolfe et al., 1966; Hundhausen et al., 1970). The radial dependence of proton temperature T_p as a function of the heliocentric distance r is measured on the average as $r^{-0.74}$ compared to $r^{-4/3}$ corresponding to adiabatic expansion (Hellinger et al., 2011). This slow decay of the temperature is consistent with the solar wind undergoing significant heating. Identifying the physical mechanisms responsible for this heating and quantifying their contribution as a function of plasma and solar wind parameters is fundamentally important to describing the solar corona and solar wind and to characterizing heating in plasma systems more generally. Several mechanisms have been proposed to heat the solar wind as it expands, including cyclotron damping (Cranmer, 2000), magnetic reconnection (Drake et al., 2009; Osman et al., 2012, 2014; Mistry et al., 2017), Landau damping (Leamon et al., 1999; Cranmer et al., 2007; Gary and Nishimura, 2004) and stochastic heating (McChesney et al., 1987; Johnson and Cheng, 2001; Chaston et al., 2004; Voitenko and Goossens, 2004; van der Holst et al., 2014).

This Chapter focuses on stochastic ion heating: such heating occurs when the motion of ions becomes chaotic as the amplitude of electromagnetic field fluctuations at scales comparable to the ion gyroscale exceed a critical value. Under these conditions, the magnetic moment of ions is not conserved, allowing diffusion in energy perpendicular to the magnetic field and leading to perpendicular heating of the ions. Stochastic heating may have a significant contribution to the ion heating in coronal holes and the solar wind, however its importance relative to other mechanisms is an open question. Coronagraph measurements have shown that minor ions such as O^{+5} originating from coronal holes have significantly larger perpendicular temperature $T_\perp$ (with respect to the

magnetic field) than parallel $T_{||}$ Kohl et al. (1998); Antonucci et al. (2000). In situ observations of the fast solar wind frequently find similar proton temperature anisotropy of $T_{\perp}/T_{||} > 1$ (Marsch et al., 2004; Hellinger et al., 2006, e.g).

Chandran et al. (2010) modeled ion stochastic heating by low frequency ($\omega < \Omega_p$, where ω and Ω_p denote the wave and proton cyclotron frequencies, respectively) Alfvén (AW) and kinetic Alfvén waves (KAW). They proposed that the heating rate of this mechanism is very sensitive to the amplitude of the turbulent velocity fluctuations, which they characterized by the dimensionless parameter $\epsilon_i = \delta v_\rho / v_\perp$ where δv_ρ denotes the amplitude of root-mean-square velocity fluctuations at scales comparable to the ion gyroscale while $v_\perp$ is the ion's thermal speed perpendicular to the background magnetic field. When the velocity fluctuations are smaller than some critical value, $\epsilon_i \ll \epsilon_{\rm crit}$, the magnetic moment of the ions is conserved and any stochastic heating is suppressed. When $\epsilon_i \gtrsim \epsilon_{\rm crit}$ magnetic moment conservation is violated,leading to energy diffusion perpendicular to the magnetic field and an increase in $T_\perp$. In test particle simulations from Chandran et al. (2010) $\epsilon_{\rm crit}$ was reported as 0.19. Chandran et al. (2010) predicted that depending on the values of $\beta_{||p}$ (ratio of parallel thermal pressure to magnetic pressure; $n_p k_B T_{||p}/(B_0^2/2\mu_0)$, where n_p denotes the proton density, k_B is the Boltzmann constant, $T_{||p}$ is the parallel proton temperature, B_0 is the magnitude of the magnetic field, and μ_0 is the permeability of free space) the following proton heating behaviors are expected under the assumption of low-frequency, KAW-like turbulence:

1. If $\beta_{\|p} \ll 1$ and $\epsilon_p \ll \epsilon_{\rm crit}$, electrons absorb the vast majority of the cascade power and proton heating is negligible as the Landau resonance condition ($\omega - k_\| v_\| = 0$, where $k_\|$ and $v_\|$ denote the parallel wavenumber and particle velocity along the magnetic field direction, respectively) is not satisfied for protons (Quataert, 1998; Gruzinov, 1998).

2. If $\beta_{\|p} \ll 1$ and $\epsilon_p \gtrsim \epsilon_{\rm crit}$, stochastic ion heating operates and AW/KAW turbulence causes both electron and perpendicular proton heating while the parallel proton heating is negligible.

3. If $\beta_{\|p} \sim 1$ and $\epsilon_p \ll \epsilon_{\rm crit}$, electron and parallel proton heating occurs due to Landau damping and transit-time damping of KAWs. Stochastic heating is suppressed producing no increase

in the perpendicular proton temperature.

4. If $\beta_{\|p} \sim 1$ and $\epsilon_p \gtrsim \epsilon_{\rm crit}$, stochastic heating operates and the electrons and protons both receive significant fractions of the cascade power, with similar energy transferred to both perpendicular and parallel proton temperatures.

Bourouaine and Chandran (2013) tested the predictions of Chandran et al. (2010) studying 3 days of Helios-2 measurements with radial distances ranging from 0.29-0.64 AU, focusing on fast solar wind with low plasma beta ($\beta < 0.3$). Stochastic heating by low-frequency AW/KAW turbulence was consistent with the observed perpendicular temperature in the solar wind for the three selected intervals. Xia et al. (2013) performed further tests of the model of Chandran et al. (2010), describing test particles interacting with strong reduced magnetohydrodynamic (RMHD) turbulence. RMHD was found to be much more effective at stochastic heating than randomly phased waves used in previous studies. They suggested that stochastic heating can occur not only under $\beta \ll 1$ conditions of the solar corona but also when $\beta \sim 1$, typically occurring at 1 AU. Klein and Chandran (2016) modeled the evolution of proton distributions due to stochastic heating in the range of 4 to 30 solar radii, finding that the proton distributions developed non-Gaussian structures characterized with a flat core and steep tail.

Despite these works, the role of stochastic heating in the solar wind is not yet fully understood. In particular no statistical study using solar wind observations has been carried out to test the effect of low-frequency AW/KAWs on proton heating. In this Chapter, we present the analysis of 13 years of Wind data to investigate scalar proton and electron temperatures and proton temperature anisotropy as a function of β and turbulence amplitude. We expect and find positive correlation between the turbulence amplitude and T_p, in agreement with previous studies (e.g. Grappin et al., 1990; Wu et al., 2013; Matthaeus et al., 2016), suggesting that the damping mechanism requires a higher amplitude of the fluctuations in order to operate. We explicitly compare the observed features to the expected behavior of stochastic heating and find the proton temperature depends on a critical turbulence amplitude in agreement with the predictions of Chandran et al. (2010).

3.2 Method

3.2.1 Background

The goal of the data analysis was to organize temperature measurements as a function of (ϵ_p, $\beta_{||p}$) and compare the temperature dependence of these parameters with the predictions of stochastic ion heating. Following the methodology of Bourouaine and Chandran (2013), we define the velocity fluctuations at the proton gyroscale, δv_p, as

$$\delta v_p = \sigma v_A \delta B_p / B_0 \tag{3.1}$$

where $\sigma = 1.19$ is a dimensionless constant arising from the KAW dispersion relation, $v_A = B_0/\sqrt{\mu_0 \rho}$ denotes the Alfvén speed, ρ is the mass density of the solar wind, and δB_p is the amplitude of magnetic field fluctuations at proton gyroscale. This approximation is necessary as observations of velocity fluctuations have not yet been made at sufficiently high cadences to resolve δv_p except in unusual solar wind conditions. In Equation 3.1, δB_p is obtained by evaluating

$$\delta B_p = \frac{\pi}{C_\gamma} \left[\int_{e^{-0.5} f_\rho}^{e^{0.5} f_\rho} P_f(f) df \right]^{1/2} \tag{3.2}$$

where $P_f(f)$ denotes the observed turbulent spectrum of magnetic fluctuations, f_ρ is the frequency corresponding to the proton gyroradius defined as $V_{SW} \sin(\Theta_{VB})/2\pi\rho_p$, where V_{SW} is the speed of the solar wind, Θ_{VB} is the angle between the solar wind velocity vector and the magnetic field and ρ_p is the proton gyroradius. The dimensionless parameter C_γ arises from the integral $\int_0^{\pi/2} (\cos\phi)^{\gamma-1} d\phi$, and is defined as

$$C_\gamma = \frac{\sqrt{\pi}\Gamma\left[\frac{\gamma}{2}\right]}{2\Gamma\left[\frac{\gamma+1}{2}\right]} \tag{3.3}$$

where γ is the absolute value of the spectral index of the turbulent spectrum within the integration limits. An extensive discussion of using magnetic fluctuation frequency spectra as a proxy for gyroscale velocity fluctuations can be found in Appendices A and B of Bourouaine and Chandran

(2013).

Equation 3.2 assumes that C_γ is constant within the integration limits, meaning that the spectral index γ does not change in the given frequency range. This requirement is violated when the break frequency f_b is within the integration limits, $e^{-0.5f_\rho} < f_b < e^{0.5f_\rho}$. Bourouaine and Chandran (2013) restricted their analysis to 3 intervals when the integration limits were above the break of the turbulent spectrum, $f_b < e^{-0.5f_\rho}$. As we aim to use a statistical approach, we employ the following approximation when f_b is within the integration limits of Equation 3.2. We replace C_γ in Equation 3.2 with $\bar{C_\gamma}$, the weighted average of C_γ below and above f_b:

$$\bar{C_\gamma} = \frac{C_{\gamma 1} \int_{e^{-0.5}f_\rho}^{f_b} P_f(f)df + C_{\gamma 2} \int_{f_b}^{e^{0.5}f_\rho} P_f(f)df}{\int_{e^{-0.5}f_\rho}^{f_b} P_f(f)df + \int_{f_b}^{e^{0.5}f_\rho} P_f(f)df} \tag{3.4}$$

where $C_{\gamma 1,2}$ is calculated separately for the spectral indices above and below f_b using Equation 3.3. This approximation is used in 31% percent of the intervals. Given δB_p calculated from Equations 3.2 and 3.4, we calculate $\epsilon_p = \delta v_p / v_\perp$ using Equation 3.1 and the perpendicular proton thermal speed $v_\perp = \sqrt{2k_B T_\perp / m_p}$.

3.2.2 Application

In this study, high resolution Wind magnetic field data (92 ms cadence) (Lepping et al., 1995) were used together with onboard ion moments and ion parameters (92 second cadence) from the Faraday cup instrument (Lin et al., 1995; Ogilvie et al., 1995). Data from January 2004 to December 2016 were selected to ensure Wind was in the pristine solar wind. For the analysis, the magnetic field and plasma data were split in 10-minute intervals. The power spectral density (PSD) of the magnetic field components were calculated separately using Fourier transform and then the component PSDs were added to obtain the total PSD (Koval and Szabo, 2013). The time series of $\beta_{||p}$, $T_{||}$, $T_\perp$ and electron temperature (T_e) were averaged over the 10-minute periods. Overall, $\sim 5.8 \cdot 10^5$ turbulent spectrums and corresponding average solar wind parameters were computed. Due to gaps in the data, only $\sim 5.2 \cdot 10^5$ average electron temperatures were obtained.

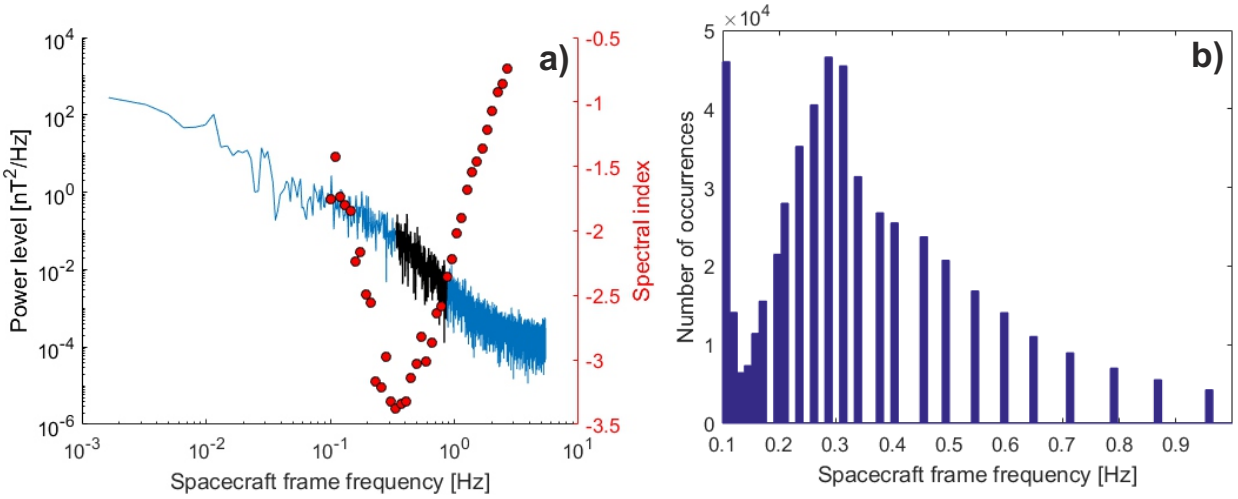

Figure 3.1: (a) an example of the measured magnetic turbulent spectrums and the measured spectral indices (red marks) in the 0.1-5.17 Hz range; (b) histogram of the low frequency end of the measured dissipation ranges (black part of the spectrum in panel a) for all the $\sim 5.8 \cdot 10^5$ periods.

For the correct calculation of C_γ and $\bar{C}_\gamma$ (Equations 3.3-3.4), it was necessary to estimate f_b, which shows some variability ranging from 0.1-1 Hz (Markovskii et al., 2008; Chen et al., 2014; Franci et al., 2016; Telloni and Bruno, 2016) making its parameterization difficult. To automatically estimate this frequency, we developed the following algorithm: starting from 0.1 Hz until 5.17 Hz a grid of 43 logarithmically spaced frequencies was generated. For each PSD, 33 linear fits were made in the frequency range between the ith and i+10th element of the grid. From the ensemble of fits, the steepest spectral index and the corresponding frequency range were selected. The average and standard deviation of the measured spectra indices are -2.99 ± 0.65, in very good agreement with previous studies on the dissipation range from Leamon et al. (1998) and Smith et al. (2006).

The frequency range corresponding to the steepest part of the spectrum can be used very effectively to estimate f_b, which is shown in Figure 3.1a and b. A typical magnetic field turbulent spectrum is presented in Figure 3.1a. The steepest part of the spectrum (corresponding to the dissipation range) was detected automatically with our algorithm and is marked with a black line. The red circles denote the 33 spectral indices in the range of $0.1 - 5.17$ Hz. In Figure 3.1b, we investigate how well this method could be used as a proxy for f_b on a statistical basis. A histogram of the

low frequency end of the dissipation range is illustrated, based on all the available $\sim 5.8 \cdot 10^5$ data points. The distribution has a peak at around 0.3 Hz, decaying rapidly toward larger frequencies with only 0.8% of the distribution having f_b larger than 1 Hz (not shown). There is a secondary peak between 0.1-0.126 Hz, the majority of these spectrums did not display a well-defined high frequency break because the spectrum flattened immediately after the inertial range due to reaching the noise floor (Koval and Szabo, 2013). This occurs when the amplitude of the inertial scale magnetic field fluctuations are very small, reducing the power level of the spectrum. The measurements in the range of 0.1-0.126 Hz ($\sim 11\%$ of the overall spectrums) shown in Figure 3.1b were excluded from the study. The remaining frequencies had a median value of 0.3 Hz, which is in very good agreement with the study of Markovskii et al. (2008) who manually inspected 454 magnetic turbulent spectrums and found that the median of f_b was approximately 0.3 Hz. They also found that f_b was larger than 1 Hz in 2.1% of the cases and it was lower than 0.1 Hz in 4.3% of the cases.

To accurately evaluate the integral in Equation 3.2, the unphysical flattening of the high frequency part of the spectrum must be considered. In the cases when the high frequency end of the integration limit $e^{0.5} f_\rho$ was outside the dissipation range (black region in Figure 3.1a) linear extrapolation was used to estimate the power of the turbulent spectrum at f_ρ (Bourouaine and Chandran, 2013). When f_b was within the integration limits of Equation 3.2, linear fits were used in the ranges of [$e^{-0.5} f_\rho$, f_b] and [f_b, $e^{0.5} f_\rho$] to calculate $\gamma_{1,2}$ and $\bar{C}_\gamma$. The integration of Equation 3.2 was done with trapezoid technique to obtain δB_p. Table 1 compares the results of Bourouaine and Chandran (2013) in the range of $0.29 - 0.64$ AU with the median values calculated from our study.

Parameter	Measurements at 0.29, 0.4 and 0.64 AU	Median value of our study at 1 AU
δB_p [nT]	1.16; 0.70; 0.32	0.20
δv_p [km/s]	5.15; 4.13; 3.21	2.34
ϵ_p	0.0471; 0.0486; 0.0480	0.0520

Table 3.1: Comparison of δB_p, δv_p and ϵ_p from Bourouaine et al. (2013) with the values presented in our study

3.3 Results

In order to study the proton temperature distribution, a grid with 50 x 25 equally logarithmic spaced bins was generated in the (ϵ_p, $\beta_{||p}$) space. The scalar proton temperature ($(T_{||} + 2T_{\perp})/3$), proton temperature anisotropy ($T_{\perp}/T_{||}$) and ratio of the scalar proton and electron temperature (T_p/T_e) were binned in the defined grid. The median value of each bin was selected and sparse bins with less than 10 data points were excluded from the study. To avoid the possible effect of outliers, we excluded the lowest and highest 1% of ϵ_p values.

Figure 3.2a shows the distribution of the data peaking at $\beta_{||p} = 0.99$ and $\epsilon = 0.0520$. The color bars in Figure 3.2b, c and d show the binned scalar proton temperature (on logarithmic scale), proton temperature anisotropy (on linear scale) and proton-electron temperature ratio (on linear scale), respectively. Cross sections of Figure 3.2b, c and d along $\beta_{||p}$ =0.2, 1 and 2 (marked with vertical lines) as a function of ϵ_p are shown in Figure 3.3a, b and c, respectively. The scalar proton temperature in Figure 3.2b shows a clear dependence on ϵ_p and a sharp increase in the temperature can be seen at approximately $\epsilon_p = 10^{-1.6}$, marked with a black line. When ϵ_p is smaller than $10^{-1.6}$ the temperature is around $5 \cdot 10^4$ K while for $\epsilon_p > 10^{-1.6}$ the peak temperature is $3.1 \cdot 10^5$ K. $\epsilon_p > 10^{-1.6}$ occurred in 76% of the $\sim 5.8 \cdot 10^5$ studied intervals. The $\beta_{||p}$ dependence of the scalar proton temperature is shown in Figure 3.3a: in all cases a sudden temperature enhancement can be seen when ϵ_p is in the range of $10^{-1.72}$ and $10^{-1.6}$ (marked with vertical lines).

In Figure 3.2c, the proton temperature anisotropy increases as a function of ϵ_p when $\beta_{||p} < 1$ while no significant systematic trend can be seen for $\beta_{||p} > 1$. In Figure 3.3b the cross section at $\beta_{||p} > 0.2$ shows some variations around $T_{\perp}/T_{||} = 1$ when $\epsilon_p < 10^{-1.6}$. For $\epsilon_p > 10^{-1.6}$ there is a significant increase in the perpendicular proton temperature, resulting in $T_{\perp}/T_{||} \sim 1.20$. In the case of $\beta_{||p} = 1$ and $\epsilon_p < 10^{-1.6}$, $T_{\perp}/T_{||}$ shows minor preference for an enhanced parallel temperature ($T_{\perp}/T_{||} \sim 0.96$) while for $\epsilon_p > 10^{-1.6}$ $T_{\perp}/T_{||}$ approaches unity.

The T_p/T_e distribution in Figure 3.2d shows similarities to the scalar proton temperature in Figure 3.2b, with the ratio strongly depending on ϵ_p, having its lowest values for $\epsilon_p < 10^{-1.6}$. Similar to Figure 3.3a and b, the cross sections in panel c show a sudden increase of the T_p/T_e ratio

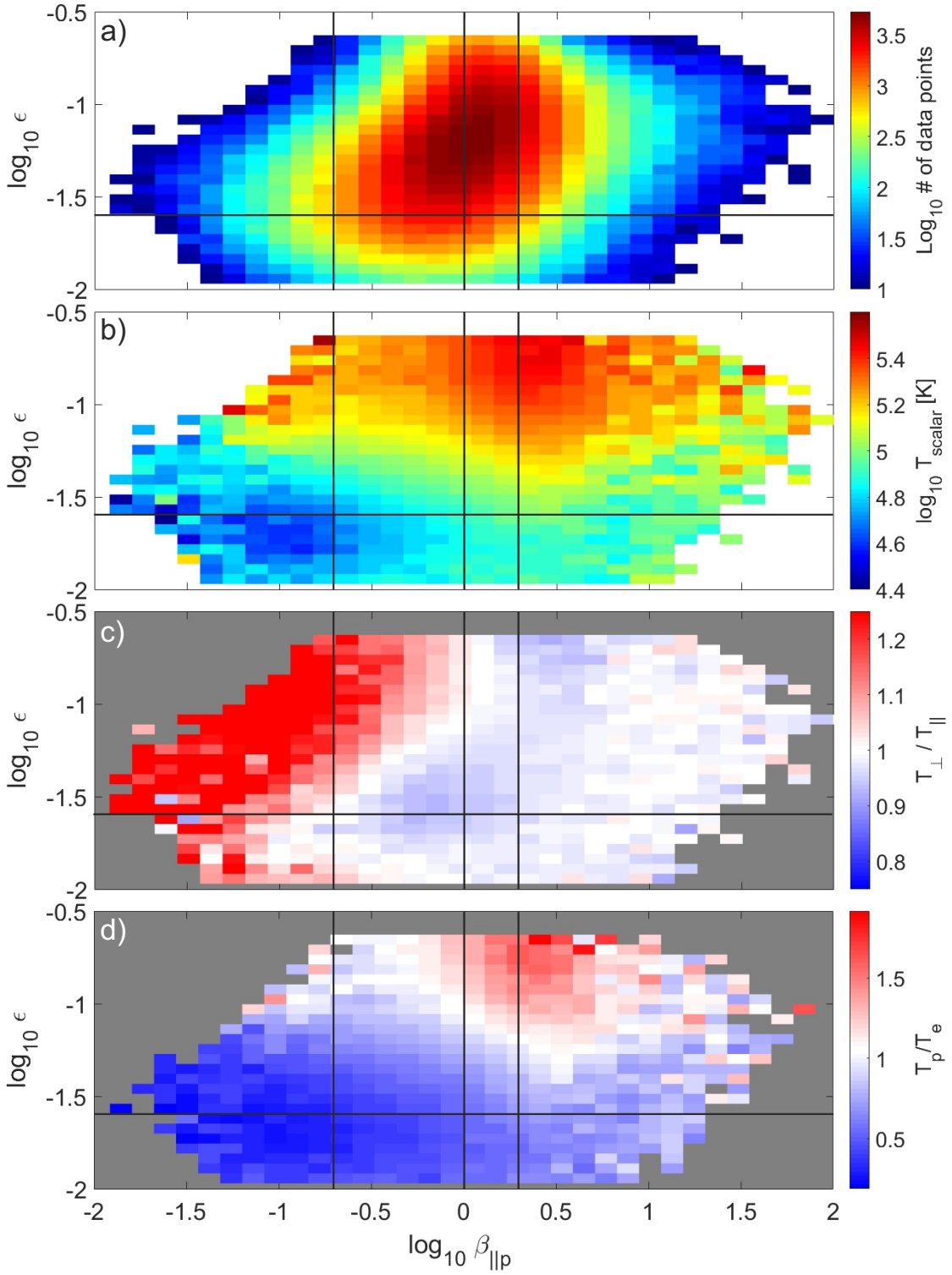

Figure 3.2: Data distribution (a), median values of the scalar proton temperature (b), proton temperature anisotropy (c) and proton-electron temperature ratio (d) in the (ϵ_p, $\beta_{||p}$) space. Horizontal line at $\epsilon_p = 10^{-1.6}$ denotes the point where stochastic heating starts operating. Vertical lines at β =0.2, 1 and 2 mark the cross sections, which are highlighted in Figure 3.3.

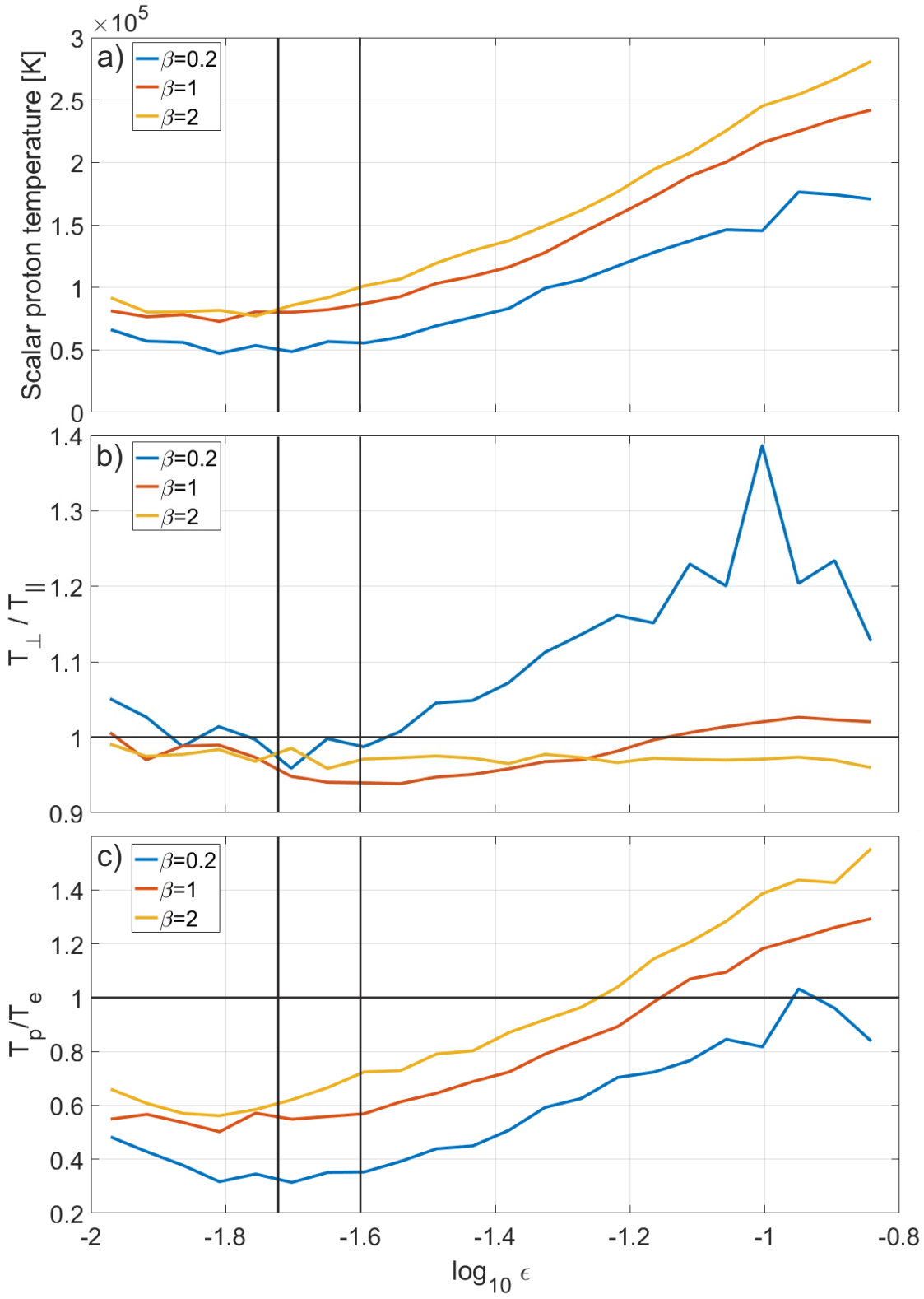

Figure 3.3: Cross sections of Figure 3.2a, b and c along $\beta_{||p}$ =0.2, 1 and 2, respectively.

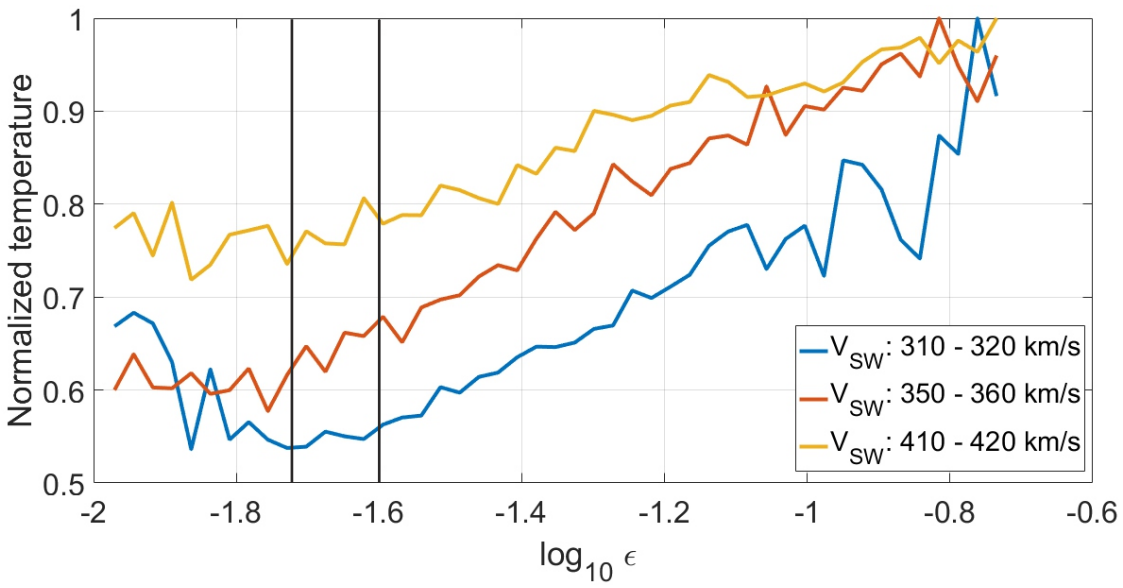

Figure 3.4: Cross sections of the binned T_p data in the (ϵ_p, V_{SW}) space along three solar wind speed intervals. Each T_p line was normalized to its peak value.

at $\epsilon_p = 10^{-1.6}$. When $\beta_{||p}$= 0.2 the proton and electron temperatures are in equilibrium ($T_p/T_e = 1$) for the largest ϵ_p values while for $\beta_{||p} = 1$, protons have a factor of 1.2 higher temperature than electrons.

T_p is known to be a strong function of the solar wind speed (e.g. Burlaga and Ogilvie, 1973; Richardson and Smith, 2003), which may affect the observed temperature variations in the $(\epsilon_p, \beta_{||p})$ space. To investigate this speed dependence the T_p data was binned in the (ϵ_p, V_{SW}) space and cross sections were taken along three solar wind speed intervals. The results are shown in Figure 3.4 where each line was normalized to its peak T_p value. The temperature variations as a function of ϵ_p are consistent with Figures 3.2-3.3 and show a sudden enhancement at approximately $\epsilon_p = 10^{-1.6}$ indicating that T_p does have a dependence on ϵ_p in addition to the dependence on V_{SW}.

We note that $\epsilon_p \propto 1/\sqrt{T_\perp}$ and $\beta_{||p} \propto T_{||}$. If only this intrinsic dependence of the variables was significant we would expect the highest T_p at the lowest ϵ_p, and for a fixed $\beta_{||p}$, $T_\perp/T_{||}$ would decrease as a function of ϵ_p. Neither of these tendencies are observed in Figures 3.2 or 3.3, implying that the amplitude of the turbulent fluctuations is the primary driver of the magnitude of ϵ_p.

3.4 Conclusion

In this Chapter, we have provided the first statistical test for the presence of stochastic ion heating of the type predicted by Chandran et al. (2010). Our findings are consistent with the prediction that stochastic heating becomes effective once gyroscale velocity fluctuations surpass a critical amplitude leading to perpendicular proton heating. We found that the critical ϵ_p value in our study is in the range of 0.019 and 0.025 and that 76% of the studied intervals had an ϵ_p value larger than 0.025, consistent with stochastic ion heating operating nearly continuously in the solar wind at 1 AU. Based on the distribution of the temperature data in the (ϵ_p, $\beta_{||p}$) space, we make the following conclusions:

1. If $\beta_{||p}$ = 0.2 and $\epsilon_p \ll \epsilon_{\rm crit}$ the lowest scalar proton temperatures ($\sim 5 \cdot 10^4$ K) were measured. The majority of the turbulent energy is absorbed by electrons as shown by the low T_p/T_e ratios observed for this case.

2. If $\beta_{||p}$ = 0.2 and $\epsilon_p \gtrsim \epsilon_{\rm crit}$, an increase in the perpendicular proton temperature was identified, with $T_\perp/T_{||} \sim 1.20$ for the largest values of ϵ_p. The scalar proton temperature increased by a factor of 3 compared to the $\beta_{||p}$ = 0.2, $\epsilon_p \ll \epsilon_{\rm crit}$ case.

3. If $\beta_{||p}$ = 1 and $\epsilon_p \ll \epsilon_{\rm crit}$, no preferential perpendicular heating was observed ($T_\perp/T_{||} \sim$ 0.96), consistent with non-stochastic heating from AW/KAW turbulence.

4. If $\beta_{||p}$ = 1 and $\epsilon_p \gtrsim \epsilon_{\rm crit}$, no preferential increase in $T_\perp$ was identified ($T_\perp/T_{||} \sim 1.01$) and the scalar proton temperature reached $1.58 \cdot 10^5$ K, a factor of 3 increase compared to the $\beta_{||p}$ = 1, $\epsilon_p \ll \epsilon_{\rm crit}$ case.

The findings above qualitatively agree with the predictions of Chandran et al. (2010), which is the main result of this Chapter. We do note that our observed value of $\epsilon_{\rm crit}$ is an order of magnitude smaller than that reported by Chandran et al. (2010), which arises from a prediction for when more than half of the cascade power near $k_\perp \rho_p = 1$ is absorbed by stochastic heating; see their Equations 25, 30, and 31. Their calculation depends sensitively on several dimensionless parameters

characterizing the turbulent fluctuations. Variation in these parameters may be sufficient to explain the discrepancy in the value of $\epsilon_{\rm crit}$.

Another potential explanation for this discrepancy arises from Kasper et al. (2017) suggesting that a majority of preferential minor ion heating occurs within a zone some tens of solar radii from the Sun's surface. It is plausible that the same mechanism preferentially heating the minor ions also heats the protons and a significant fraction of the energy transfer occurs within the preferential heating zone. Thus, the $\epsilon_{\rm crit}$ observed at 1 AU may not be the actual threshold for the onset of stochastic heating, but rather a value to which $\epsilon_{\rm crit}$ has decayed. Similarly, the observed correlation between ϵ_p and T may be a remnant of heating closer to the Sun, with plasma which underwent stochastic heating and retained relatively high values of temperature and ϵ_p compared to other plasma measured at 1 AU.

CHAPTER 4

Large-scale Control of Kinetic Dissipation in the Solar wind

This Chapter is taken from Vech, D., K. G. Klein, J. C. Kasper, Large-scale control of kinetic dissipation in the solar wind, Astrophysical Journal Letters, DOI: 10.3847/2041-8213/aad329, 2018.

In this Chapter we study the connection between the large-scale dynamics of the turbulence cascade and particle heating on kinetic scales. We find that the inertial range turbulence amplitude (δB_i; measured in the range of 0.01-0.1 Hz) is a simple and effective proxy to identify the onset of significant ion heating and when it is combined with $\beta_{||p}$, it characterizes the energy partitioning between protons and electrons (T_p/T_e), proton temperature anisotropy ($T_\perp/T_{||}$) and scalar proton temperature (T_p) in a way that is consistent with previous predictions. For a fixed δB_i, the ratio of linear to nonlinear timescales is strongly correlated with the scalar proton temperature in agreement with Matthaeus et al., though for solar wind intervals with $\beta_{||p} > 1$ some discrepancies are found. For a fixed $\beta_{||p}$, an increase of the turbulence amplitude leads to higher T_p/T_e ratios, which is consistent with the models of Chandran et al. and Wu et al. We discuss the implications of these findings for our understanding of plasma turbulence.

4.1 Introduction

A crucial factor characterizing the energy cascade rate and the relative heating of protons and electrons is the nonlinear timescale at which the energy is transferred to smaller scales (see review by Horbury et al., 2012). Goldreich and Sridhar (1995) proposed the critical balance theory predicting that the linear timescale corresponding to the propagating Alfvénic fluctuations and their nonlinear decay are comparable at each scale: $\tau_A(k_\perp) \sim \tau_{CB}(k_\perp)$ where $k_\perp$ is the perpendicular (with respect to the magnetic field) wavenumber. The Alfvén time and the nonlinear "critical balance" time are estimated for a given spatial scale perpendicular to the background magnetic field ($\lambda \sim 2\pi/k_\perp$) as

$$\tau_A(\lambda) \sim \frac{l_\parallel}{V_A} \sim \left(\frac{L}{\lambda}\right)^{1/3} \frac{\lambda}{V_A} \tag{4.1}$$

$$\tau_{CB}(\lambda) \sim \frac{\lambda}{\delta z_\lambda} \tag{4.2}$$

where $l_{||}$ is the spatial scale along the magnetic field, V_A is the Alfvén speed ($B_0/(\rho\mu_0)^{1/2}$), L is the size of the outer scale of the cascade and $\delta z = \delta v + \delta b$, δv, and δb are the Elsässer, velocity and magnetic fluctuations at scale λ, respectively. The perpendicular scale of the eddies decreases at a faster rate than the parallel scale, with the scaling $k_\parallel \propto k_\perp^{2/3}$. Both observational (e.g. Horbury et al., 2008; Podesta, 2009; Wicks et al., 2010; Chen et al., 2011) and numerical (e.g. Cho and Vishniac, 2000; Maron and Goldreich, 2001; TenBarge and Howes, 2012) studies are consistent with critical balance scalings; see Chen (2016) for a detailed review.

In contrast to critical balance theory, Matthaeus et al. (2014) argued that the most significant contributions to nonlinear spectral transfer are independent of τ_A. They proposed that at kinetic scales the relevant time scale ratio is between the gyroperiod,$\tau_{ci} \sim \Omega_{ci}^{-1}$, and nonlinear turnover time (e.g. the time it takes until an eddy at scale l passes all of its energy to a smaller scale) at scale

$l \sim d_i$,

$$\tau_{nl}(d_i) = \frac{V_A}{Z\Omega_{ci}} \left(\frac{L}{d_i}\right)^{1/3}, \tag{4.3}$$

which determines how the dissipated energy is partitioned in proton and electron heating ($Q_p/Q_e \sim 1/(\tau_{nl}\Omega_{ci})$). The ion inertial length is $d_i = c/\omega_{pi}$, $\omega_{pi} = \sqrt{n_i q_i^2/\epsilon_0 m_i}$ is the ion plasma frequency, $\Omega_{ci} = qB_0/m$ is the proton gyrofrequency. The total energy per unit mass is given as $Z = \sqrt{u^2 + b^2}$ where u and b denote the root-mean-square velocity and magnetic field fluctuations, the latter measured in velocity units ($b = b_{rms}/\sqrt{\mu_0 \rho}$).

In addition to the nonlinear timescales, the magnitude of the gyroscale velocity fluctuations also plays an important role in controlling the proton and electron heating. When the electromagnetic field fluctuations at gyroscale surpass a critical amplitude the first adiabatic invariant of particle motion is not conserved allowing perpendicular heating of the particles known as stochastic ion heating (e.g. McChesney et al., 1987; Johnson and Cheng, 2001). Chandran et al. (2010) proposed that stochastic heating depends on the dimensionless parameter $\epsilon = \delta v_\rho / v_\perp$ where δv_ρ is the root-mean-square velocity fluctuations at gyroscale and $v_\perp$ is the ion's thermal speed perpendicular to the magnetic field. The perpendicular proton heating rate per unit mass ($Q_\perp$) at $k_\perp \rho_p \sim 1$ (where $\rho_p = v_{th\perp i}/\Omega_i$ is the proton gyroscale) as a fraction of the turbulent cascade power per unit mass (Γ), assuming a balanced spectrum of kinetic Alfvén waves (KAWs) can be given in the form of

$$\frac{Q_\perp}{\Gamma} = 3.0 \exp\left(\frac{-0.34}{\epsilon}\right). \tag{4.4}$$

Equation (4.4) implies that half of the total cascade power is directed into perpendicular proton heating at $k_\perp \rho_p \sim 1$ when $\epsilon = 0.19$.

Another significant parameter affecting the dissipation process is $\beta_{||p}$, which enhances or completely restricts the operation of certain heating mechanisms. When $\beta_{||p} \ll 1$ electron Landau damping dominates while proton Landau damping is negligible since the thermal ions are too slow to satisfy the Landau resonance condition (Quataert, 1998). On the other hand, when $\beta_{||p} \sim 1$ Landau and transit time damping of kinetic Alfvén waves lead to significant parallel proton heating

(Gary and Nishimura, 2004). Heating due to reconnection may also depend on $\beta_{||p}$: Mistry et al. (2017) found that the temperature increase of the exhaust region is a function of the inflow $\beta_{||p}$ and reconnection guide field. The onset of stochastic heating is thought to be independent of $\beta_{||p}$ for $\beta_{||p} \lesssim 1$ (Chandran et al., 2010).

Electron and proton heating by solar wind turbulence have been investigated by both observational (e.g. Cranmer et al., 2009; Coburn et al., 2012; He et al., 2015; Sorriso-Valvo et al., 2018) and numerical studies (e.g. Breech et al., 2009; Servidio et al., 2012; Wan et al., 2015, 2016; Gary et al., 2016). Wu et al. (2013) used particle-in-cell simulation in the presence of a strong magnetic field to study how the decaying energy in the turbulent cascade is partitioned between protons and electrons and concluded that as the turbulence energy increases protons are heated more. The crossover value ($T_e = T_p$) occurred when the initial turbulence amplitude ($\delta b/B_0$) reached 2/5. They suggested that the correlation between the proton heating and turbulence amplitude is primarily due to the increased involvement of coherent structures in the kinetic processes (e.g. Parashar et al., 2009; Markovskii and Vasquez, 2010; Greco et al., 2012).

Cerri et al. (2017) compared a two-dimensional (2-D) hybrid Vlasov-Maxwell simulation of externally driven turbulence and a hybrid 2-D particle-in-cell simulation of freely decaying turbulence. Despite the fundamental differences between the two simulations, the kinetic scale turbulence was remarkably similar: the root-mean-square amplitudes of the density, parallel and perpendicular magnetic field fluctuations showed less than a factor of two difference and depended only on β. Cerri et al. (2017) concluded that regardless how the large-scale fluctuations are injected, the system continuously "reprocesses" the turbulent fluctuations as they are cascading towards smaller scales and the response of the system is primarily driven by β.

In this Chapter, we continue this general line of inquiry and study how the dissipated energy is partitioned between protons and electrons in the solar wind as a function of the strength of the cascade. To quantify the strength of the cascade we use a directly measurable proxy, the average inertial range amplitude (δB_i) of the turbulence spectrum of magnetic fluctuations. We find that the ($\beta_{||p}$, δB_i) space organizes the solar wind plasma measurements in a way that is consistent

with current theories about solar wind heating in particular with Chandran et al. (2010), Wu et al. (2013), Matthaeus et al. (2016), and characterizes the proton-electron temperature ratio (T_p/T_e), proton temperature anisotropy ($T_\perp/T_{||}$) and scalar proton temperature (T_p). Finally, we aim to identify the timescale ratio that has the best correlation with T_p. For this purpose we test $\tau_{ci}/\tau_{nl}(d_i)$, $\tau_A(\rho_p)/\tau_{CB}(\rho_p)$ and a "hybrid" timescale ratio defined as $\tau_A(\rho_p)/\tau_{CB}(\rho_p) \times \exp(-0.34/\epsilon)$ incorporating the effect of stochastic ion heating.

4.2 Method

We selected Wind magnetic field (Lepping et al., 1995) (92 ms cadence), ion (SWE FC, 92 second cadence) and electron (45 second cadence) data (Lin et al., 1995; Ogilvie et al., 1995) from January 2004 to December 2016 and split the time series into 10-minute intervals. For each of the $\sim 5.8 \cdot 10^5$ intervals $T_{||}$, $T_\perp$ (with orientations defined based on the average magnetic field direction during each 92 second interval), $\beta_{||p}$ and T_e were averaged. The power spectral density (PSD) of the magnetic field components were calculated separately via Fourier transform and the component PSDs were summed up to obtain the total PSD (Koval and Szabo, 2013). The spectral index in the inertial range was calculated by fitting the PSD between $0.01 - 0.1$ Hz; δB_i corresponds to the average (in log space) power level measured in this frequency range. The average and standard deviation of the measured spectral indices are -1.68 $\pm$ 0.26, respectively in excellent agreement with previous studies (e.g. Leamon et al., 1999; Smith et al., 2006; Alexandrova et al., 2009).

To estimate τ_A (Equation 4.1) and τ_{nl} (Equation 4.3) we assume that the spectral break between the outer and inertial ranges of the turbulence cascade is at a constant frequency of 10^{-4} Hz (e.g. Podesta, 2009; Wicks et al., 2011) and calculate the size of the outer scale L as $V_{sw}/(2\pi 10^{-4})$ where V_{sw} is the solar wind speed. Matthaeus et al. (2014) suggested that under typical solar wind conditions Z/V_A is expected to be in the range of 0.5-1. We calculated Z based on the root-mean-square velocity and magnetic field fluctuations during each 10 min interval and found that the median Z/V_A ratio is 0.42.

Measuring the gyroscale velocity fluctuations with current instruments is only possible under exceptional solar wind conditions. To be able to conduct a statistical study we use the approach of Bourouaine and Chandran (2013) to estimate δv_ρ in Equation (4.2) based on the spectrum of magnetic field fluctuations as $\delta v_\rho = \sigma V_A \delta B / B_0$ where $\sigma = 1.19$ is a dimensionless constant arising from the kinetic Alfvén dispersion relation and δB is the gyroscale turbulence amplitude. For details of the technique and its application for a statistical study see Bourouaine and Chandran (2013) and Vech et al. (2017). For the calculation of δb in Equation (4.2) we used the gyroscale turbulence amplitude expressed in Alfvén units: $\delta b = \delta B / (\mu_0 \rho)^{1/2}$.

4.3 Results

The distributions of T_p, $T_\perp / T_{||}$ and T_e were studied in 2-D histograms with 50x50 logarithmically spaced bins in the $(\beta_{||p}, \delta B_i)$ space. The median of each bin was selected and sparse bins with fewer than 10 data points were discarded. In our data set the medians of $\beta_{||p}$ and δB_i are 0.99 and 0.72 nT^2/Hz, respectively.

The scalar proton temperature in Figure 4.1a increases as a function of δB_i and when δB_i is larger than 0.2 nT^2/Hz the peak temperature is around $4 \cdot 10^5$ K while for $\delta B_i < 0.1$ nT^2/Hz the temperature is around $3 \cdot 10^4$ K. The δB_i dependence of the scalar proton temperature is shown in Figure 4.2a for three values of $\beta_{||p}$ as dashed lines: in all cases the temperature increases nearly exponentially as a function of $\log_{10} \delta B_i$.

In Figure 4.1b, the proton temperature anisotropy is significantly different for the $\beta_{||p} < 1$ and $\beta_{||p} > 1$ regions: for small $\beta_{||p}$ the anisotropy increases as a function of δB_i while for large $\beta_{||p}$ no obvious systematic trend can be seen. In Figure 4.2b, the temperature anisotropy for $\beta_{||p} = 0.2$ is nearly constant when $\delta B_i < 0.2$ nT^2/Hz while for $\delta B_i > 0.2$ nT^2/Hz there is a clear indication of perpendicular proton heating ($T_\perp / T_{||} \sim 1.15$). In the case of $\beta_{||p}$=1, for low δB_i values minor parallel heating is observed ($T_\perp / T_{||} \sim 0.95$) and the temperature anisotropy reaches unity in the high δB_i limit.

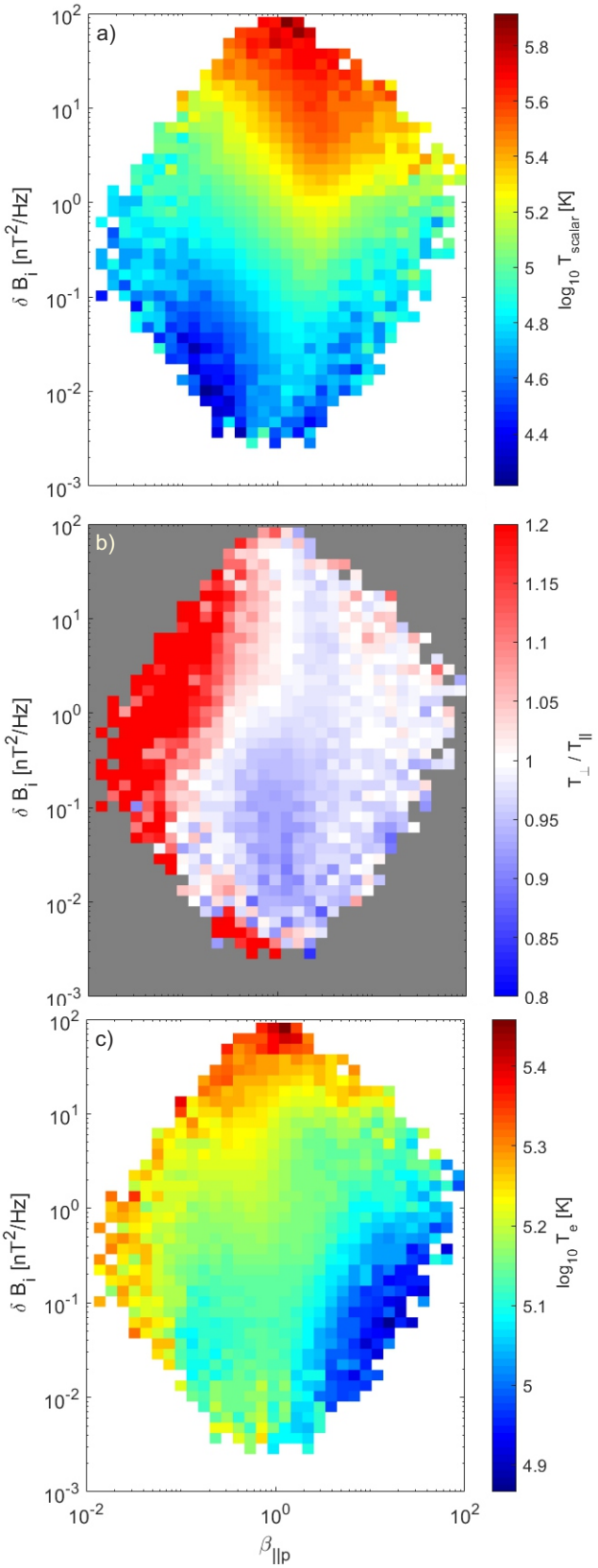

Figure 4.1: Median values of the scalar proton temperature (a), proton temperature anisotropy (b) and electron temperature (c) in the ($\beta_{||p}$, δB_i) space.

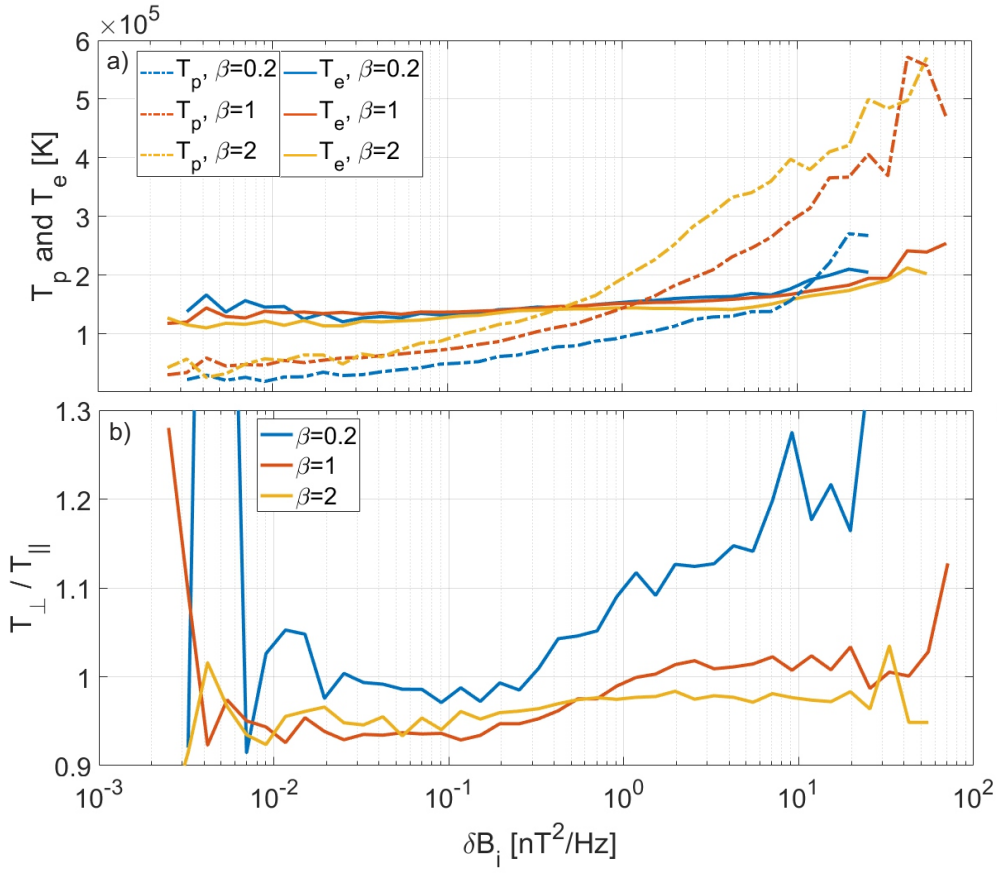

Figure 4.2: a) Cross sections of Figures 4.1a (dashed lines) and c (solid lines) along $\beta_{||p}$ =0.2, 1 and 2, respectively. b) Cross section of Figure 4.1b along $\beta_{||p}$ =0.2, 1 and 2, respectively.

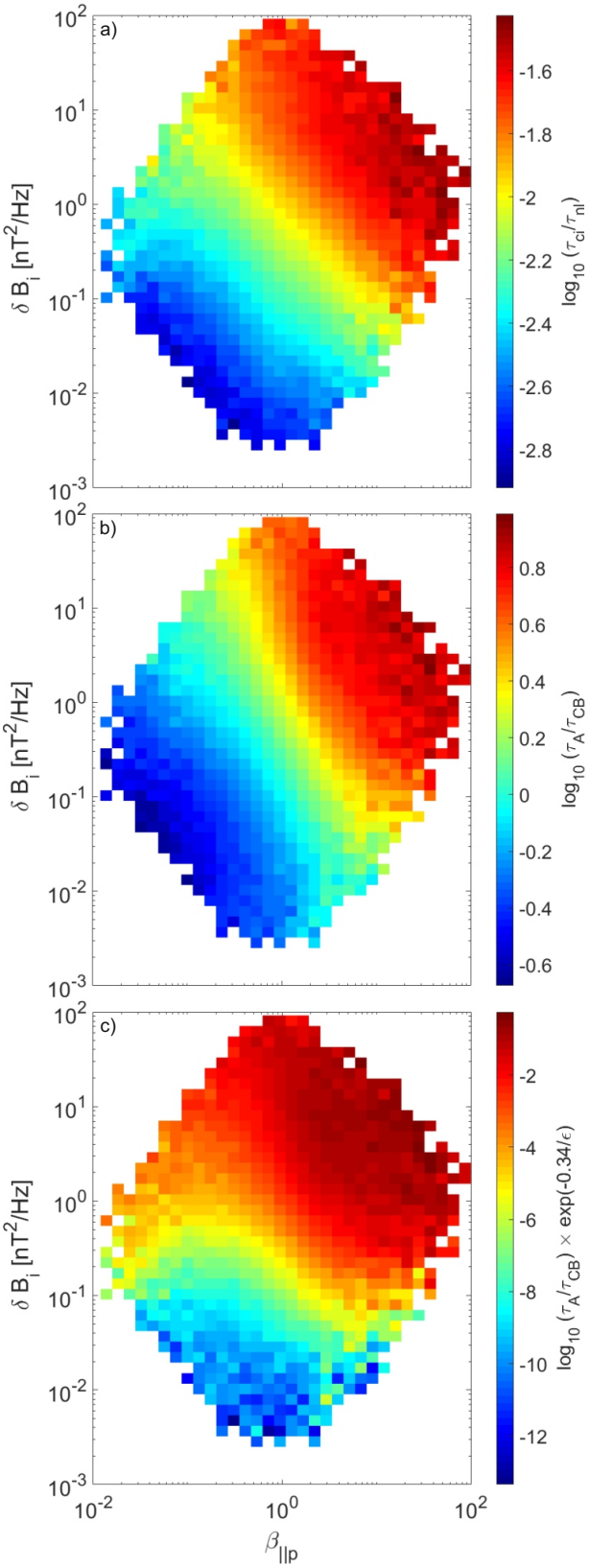

Figure 4.3: Median values of $\tau_{ci}/\tau_{nl}(d_i)$ (a), $\tau_A/\tau_{CB}(\rho_p)$ (b), $\tau_A/\tau_{CB}(\rho_p) \times exp(-0.34/\epsilon)$ (c) in the ($\beta_{||p}$, δB_i) space.

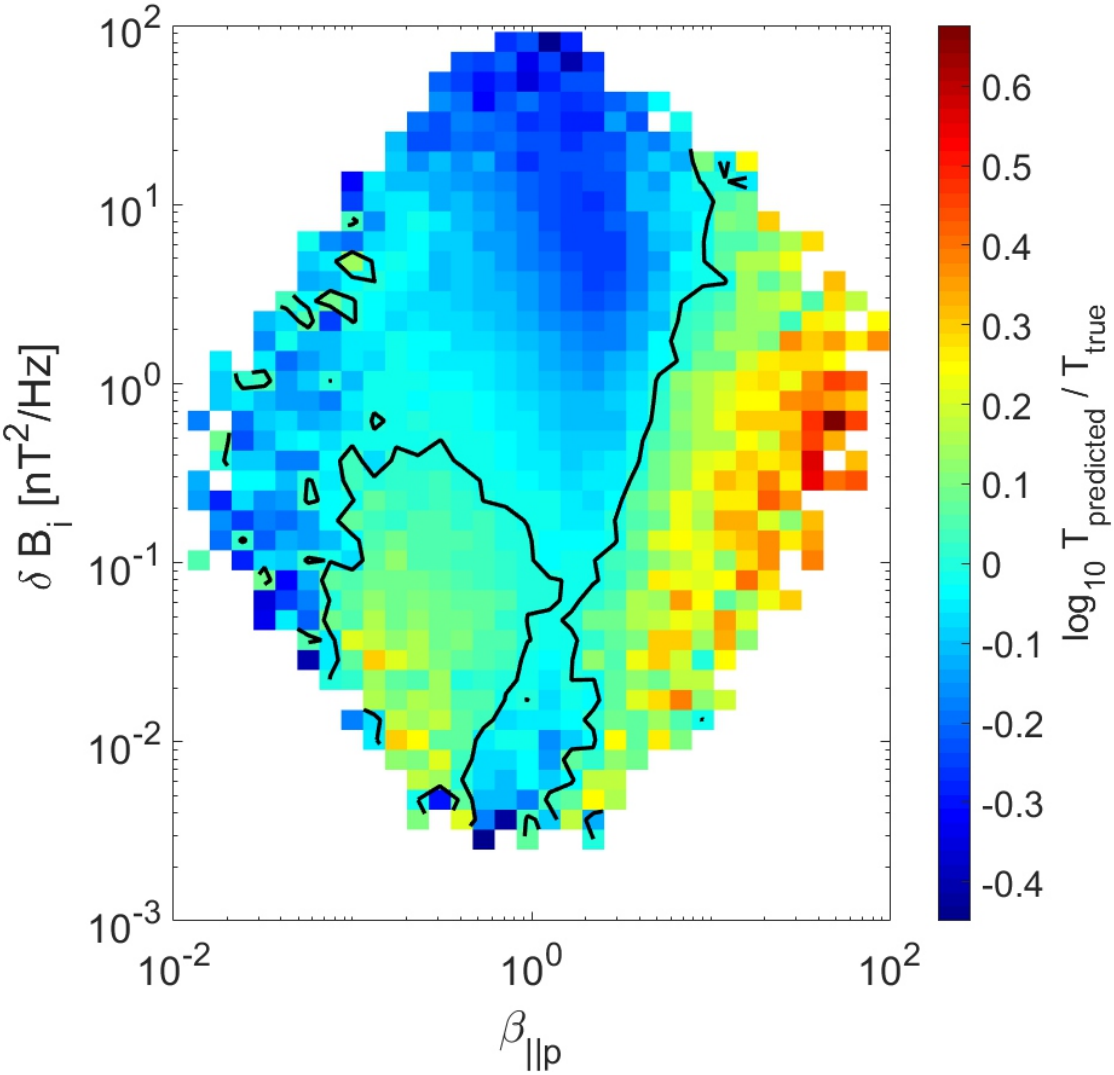

Figure 4.4: Median values of the $T_{predicted}/T_{true}$ ratios in the ($\beta_{||p}$, δB_i) space testing the $\beta_{||p}\delta B_i \sim T_p$ scaling. The contour indicates the $T_{true} = T_{predicted}$ boundary.

In Figure 4.1c the T_e distribution shows positive correlation with δB_i and the T_e values change with approximately a factor of three across the whole range of δB_i. In Figure 4.2a when δB_i <0.4 nT^2/ Hz, $T_p/T_e < 1$ while for the largest δB_i values the protons have a factor of 2.5 higher temperature than electrons. It is important to note that the proton-electron temperature equilibrium shows significant dependence on $\beta_{||p}$: as $\beta_{||p}$ changes from 0.2 to 2 the δB_i value corresponding to $T_p = T_e$ significantly decreases meaning that in a plasma with high $\beta_{||p}$ even relatively small magnetic fluctuations are sufficient to produce equal proton and electron temperatures.

In Figure 4.3 we calculate the value of three timescale ratios, $\tau_{ci}/\tau_{nl}(d_i)$, $\tau_A(\rho_p)/\tau_{CB}(\rho_p)$ and a "hybrid" timescale ratio defined as $\tau_A(\rho_p)/\tau_{CB}(\rho_p) \times \exp(-0.34/\epsilon)$ in the $(\beta_{||p}, \delta B_i)$ space. As expected, the distribution of all three ratios show similarities to the proton temperature shown in Figure 4.1a. The correlation between Figure 4.3 and 4.1a is weakest in the region where $\delta B_i \in$ [0.01; 3] nT^2/Hz and $\beta_{||p} > 1$. For a fixed $\beta_{||p}$ value there is positive correlation between proton temperature and the time scale ratios, which is in qualitative agreement with the prediction of Matthaeus et al. (2016). To estimate the uncertainties in Figure 4.3 we computed the ratio of the standard deviation and mean in each bin. The average uncertainties are 29%, 25%, 34% for Figure 4.3a,b,c, respectively. We note that the errors are the lowest (below 10%) for $\beta_{p||} > 1$ and $\delta B_i > 0.1$ nT^2/Hz.

To quantify the correlation between the three distributions in Figure 4.3 with Figure 4.1a we use the Spearman's rank correlation (R_S), which measures how well the relationship between the time scale ratios and T_p can be described with a monotonic function. The correlations between the binned time scale ratios and T_p are $R_s = 0.83, 0.82, 0.88$ for τ_{ci}/τ_{nl}, τ_A/τ_{CB} and $\tau_A/\tau_{CB}\exp(-0.34/\epsilon)$, respectively. We are therefore unable to distinguish between the predictive power of these timescale ratios in determining T_p.

As $T_p \sim \beta_{\|p} B^2 \sim \beta_{\|p}\delta B_i$, the proton temperature distribution may simply be a linear function of the abscissa and ordinate variables of Figure 4.1. To test this dependence we binned $0.03 \times \beta_{\|p}\delta B_i$ as a function of the $(\beta_{||p}, \delta B_i)$; the factor of 0.03 Hz corresponds to the center (in log space) of the frequency range where δB_i is measured. The values of $0.03 \times \beta_{\|p}\delta B_i$ data were multiplied

with a constant factor of 5.9×10^5 so it had the same mean as the mean of the observed proton temperature. Finally, a least-square fit ($y = 0.201x + 4.258$) was made between the logarithm of $0.03 \times \beta_{\|p}\delta B_i$ (x) and logarithm of the actual proton temperature (y) data. If the linear $\beta_{\|p}$ and δB_i dependencies are the only significant factors in the behavior of T_p then we expect that the predicted proton temperature ($T_{predicted}$) based on the power law fit to agree well with the the observed proton temperature (T_{true}). Figure 4.4 shows the ratio $T_{predicted}/T_{true}$ in the ($\beta_{\|p}, \delta B_i$) space. Three major features can be observed: for $\beta_{\|p} < 1$ and $\delta B_i < 0.2$ nT^2/Hz the observed proton temperature is lower than the predicted values with a factor of 1.5 while for $\delta B_i > 0.2$ nT^2/Hz the observed temperature is higher by a factor of two. The discrepancy is the most significant for high $\beta_{\|p}$ where the observed temperature is a factor of three lower than the predicted one. This is also the region with the lowest correlation between the timescale ratios and T_p. Therefore we conclude that the naive $T_p \sim \beta_{\|p}\delta B_i$ scaling is not sufficient to explain the variability of the T_p distribution in Figure 4.1a.

4.4 Conclusion

In this Chapter we have studied the connection between the inertial range of the turbulent cascade and the small scale dissipation in the solar wind as function of the inertial range turbulence amplitude δB_i and $\beta_{\|p}$. Our approach links directly the characteristics of the turbulence spectrum of magnetic fluctuations to heating mechanisms on kinetic scales therefore it could be potentially a simple and effective tool to diagnose heating in the solar wind and in plasma systems more generally.

Vech et al. (2017) identified the onset of stochastic heating when $\epsilon = \delta v_\rho / v_\perp$ reached 0.025 and 76% of the studied intervals had an ϵ value larger than this. Here we used the exact same time interval allowing a direct comparison between ϵ and δB_i: when δB_i is in the range of $0.1 - 0.3$ nT^2/Hz (e.g. approximately where the sudden perpendicular temperature enhancement is observed in Figure 4.2b) the median ϵ is 0.029 and 74% of the intervals had an δB_i value larger than 0.3

nT^2/Hz. Due to this excellent agreement between critical values of ϵ and δB_i we interpret the sudden enhancement of $T_\perp/T_\parallel$ as the onset of stochastic ion heating. The evolution of the temperature parameters in Figures 4.1-4.2 across a critical threshold of turbulence amplitude is in qualitative agreement with the stochastic ion heating model of Chandran et al. (2010).

We note that the model of Chandran et al. (2010) was parameterized for gyroscale velocity fluctuations to identify the critical turbulence amplitude when the gyromotion of protons is disrupted. Our findings suggest that stochastic heating is controlled by large-scale dynamics of the turbulent cascade and reaching the critical turbulence amplitude at gyroscale is a direct consequence of the increased energy cascade rate from larger scales.

For a fixed $\beta_{||p}$, the T_p/T_e ratio increases as a function of δB_i. When the turbulence amplitude is small ($\delta B_i < 0.3$ nT^2/Hz) electrons are hotter, while for larger turbulence amplitudes $T_p/T_e > 1$. As $\beta_{||p}$ increases $T_p = T_e$ occurs at smaller δB_i meaning that in a high $\beta_{||p}$ plasma even relatively small turbulence amplitudes can lead to equal proton and electron temperatures. These findings may be especially relevant for astrophysical plasmas where $\beta_p \gg 1$. Our results are in qualitative agreement with the predictions of Wu et al. (2013), however we note that the increased proton temperatures as a function of δB_i may be partially caused by stochastic ion heating, the effects of coherent structures in the proton heating, or both mechanisms.

The timescale ratios had similar distributions in the $(\beta_{||p}, \delta B_i)$ space and they all had strong correlation with the proton temperature data ($0.88 > R_S > 0.82$), thus in our data they are indistinguishable. For a fixed δB_i value, the T_p/T_e ratio increases as a function of all the timescale ratios, which is consistent with the prediction of Matthaeus et al. (2016). The weakest correlation between the timescale ratios and T_p was observed for high $\beta_{||p}$.

Finally, Cerri et al. (2017) suggested that the response of a plasma system is primarily driven by the amount of available energy at kinetic scales and $\beta_{||p}$. Our findings are in agreement with this concept and $\beta_{||p}$ may have the most significant influence on the proton-electron temperature ratio by restricting and enhancing the operation of certain heating mechanisms.

CHAPTER 5

Magnetic Reconnection May Control the Ion-scale Spectral Break of Solar Wind Turbulence

This Chapter is taken from Vech, D., A. Mallet, K. G. Klein, J. C. Kasper, Magnetic reconnection may control the ion-scale spectral break of solar wind turbulence, Astrophysical Journal Letters, DOI: 10.3847/2041-8213/aab351, 2018.

The power spectral density of magnetic fluctuations in the solar wind exhibits several power-law-like frequency ranges with a well defined break between approximately 0.1 and 1 Hz in the spacecraft frame. The exact dependence of this break scale on solar wind parameters has been extensively studied but is not yet fully understood. Recent studies have suggested that reconnection may induce a break in the spectrum at a "disruption scale" λ_D, which may be larger than the fundamental ion kinetic scales, producing an unusually steep spectrum just below the break. We present a statistical investigation of the dependence of the break scale on the proton gyroradius ρ_i, ion inertial length d_i, ion sound radius ρ_s, proton-cyclotron resonance scale ρ_c and disruption scale as a function of $\beta_{\perp i}$. We find that the steepest spectral indices of the dissipation range occur when β_e is in the range of 0.1-1 and the break scale is only slightly larger than the ion sound scale (a situation occurring 41% of the time at 1 AU), in qualitative agreement with the reconnection model. In this range the break scale shows remarkably good correlation with λ_D. Our findings suggest that, at least at low β_e, reconnection may play an important role in the development of the dissipation range turbulent cascade and causes unusually steep (steeper than -3) spectral indices.

5.1 Introduction

Below the ion kinetic break scale λ_B, in the so-called "dissipation range", the turbulent spectrum steepens – generally the spectral index is approximately -2.8 or steeper in this range (below but above a second break or exponential cutoff at electron kinetic scales) (Alexandrova et al., 2009; Sahraoui et al., 2010). This steepening of the spectrum has been explained (Schekochihin et al., 2009; Howes et al., 2011; Boldyrev and Perez, 2012) by the fact that below the characteristic ion kinetic scales, the dispersion relation of the characteristic fluctuations of the plasma changes. At moderate-to-high ion plasma beta ($\beta_i = 2\mu_0 n_i k_B T_i / B_0^2$), Alfvén waves (AW) transition into dispersive kinetic Alfvén waves (KAW) when the perpendicular wavenumber becomes comparable to the inverse gyroradius, $k_\perp \rho_i \sim 1$, where $\rho_i = v_{\mathrm{th}\perp i}/\Omega_i$, the ion's perpendicular thermal speed is $v_{\mathrm{th}\perp i} = \sqrt{2k_B T_{\perp i}/m_i}$ and the ion gyrofrequency is $\Omega_i = ZeB_0/m_i$. For $\beta_i \ll 1$ (and simultaneously, $\beta_e = 2\mu_0 n_e k_B T_e / B_0^2 \ll 1$), this transition occurs at $k_\perp \rho_s \sim 1$, where $\rho_s = \rho_i \sqrt{ZT_e/2T_i}$ is the ion sound radius. Thus, one might expect $\lambda_B \sim \rho_i$ at $\beta_i \gtrsim 1$ and $\sim \rho_s$ at $\beta_i \ll 1$. The former scaling appears in measurements of the break scale at $\beta_i \sim 1$ (Sahraoui et al., 2010; Alexandrova et al., 2009). However, Chen et al. (2014) studied the behavior of in two different regimes. For $\beta_i \gg 1$, they found $\lambda_B \sim \rho_i$ as expected from the KAW dispersion relation. On the other hand, for $\beta_i \ll 1$, they found that the break scale was much closer to the ion inertial length, $\sim d_i = c/\omega_{pi} = \rho_i/\sqrt{\beta_i}$ where $\omega_{pi} = \sqrt{n_i Z^2 e^2/\epsilon_0 m_i}$ is the ion plasma frequency; rather than $\sim \rho_s$ as would be expected from the KAW dispersion relation. Several studies have suggested that the break frequency in the $\beta_i \sim 1$ case can be well approximated with the proton-cyclotron resonance scale defined as $\rho_c = d_i + \sigma_i$ where the pseudo-gyroscale $\sigma_i = v_{th||i}/\Omega_i$ and $v_{th||i}$ is the ion's parallel thermal speed (e.g. Bruno and Trenchi, 2014; Bruno and Telloni, 2015; Woodham et al., 2018). This method relies on the cyclotron resonance condition for protons, which is satisfied when $k_{||}$ is large enough to allow resonance with the proton population. Since the turbulence is usually highly anisotropic ($k_\perp \gg k_{||}$) (e.g. Chen et al., 2010) the measured frequency spectrum generally corresponds to a $k_\perp$ wavenumber spectrum and so the proton-cyclotron resonance scale cannot explain the break without also posing an injection of energy into magnetic fluctuations at high $k_{||}$ (e.g. by

instabilities, see Klein and Howes (2015)).

The β_i-dependent behavior of the ion-scale break is thus somewhat of a mystery. The goal of this Chapter is to study the behavior of λ_B across the whole range of $\beta_{\perp i}$ in the solar wind, thus extending the work of Chen et al. (2014) on how λ_B behaves at extreme $\beta_{\perp i}$ values.

Recently, Mallet et al. (2017) and Loureiro and Boldyrev (2017) proposed that sheet-like turbulent structures naturally generated by the inertial range turbulence dynamics (Boldyrev, 2006; Chandran et al., 2015; Mallet et al., 2016; Howes, 2016; Mallet and Schekochihin, 2017; Verdini et al., 2018) may be disrupted by the onset of reconnection below a characteristic "disruption scale",

$$[n = 2] = C_D L_\perp^{1/9} (d_e \rho_s)^{4/9}, \tag{5.1}$$

where $d_e = c/\omega_{pe}$ is the electron inertial length, $\omega_{pe} = \sqrt{n_e e^2/\epsilon_0 m_e}$ is the electron plasma frequency and C_D is an undetermined dimensionless prefactor of order unity. $\lambda_D[n = 2]$ is the disruption scale of the so-called "$n = 2$" fluctuations, which determine the second-order structure function and power spectrum. Since a detailed study of intermittency (fluctuations with $n \neq 2$) is beyond the scope of this Chapter, we will adopt Equation 5.1 as a single disruption scale, henceforth denoted λ_D.

Besides Equation 5.1 there is an alternative scaling proposed by Loureiro and Boldyrev (2017) that relies on a different tearing profile

$$\lambda_D[n = 2] \sim L_\perp (d_e/L_\perp)^{8/21} (\rho_s/L_\perp)^{10/21}. \tag{5.2}$$

The two scalings are observationally indistinguishable from one another in our data set. Due to this close agreement, we elect to use Equation 5.1 in this Chapter.

Equation 5.1 is only valid when λ_D is larger than the fundamental ion kinetic scale at which the waves become dispersive (i.e., ρ_s), which happens for $\beta_e < \beta_e^{crit}$ given by

$$\beta_e^{\rm crit} = C_D^{9/2} \frac{Z m_e}{2 m_i} \left(\frac{L_\perp}{\rho_s} \right)^{1/2}, \tag{5.3}$$

thus, at low β_e, reconnection may induce a break to a steeper spectrum at a larger scale than one might expect solely on the basis of the KAW dispersion relation.

This reconnection model relies on the phenomenon of dynamic alignment, which leads to three-dimensionally (3-D) anisotropic eddies and a -3/2 spectral index in the inertial range (Boldyrev, 2006; Chandran et al., 2015; Mallet and Schekochihin, 2017). Although solar wind measurements indicate that the spectral index is closer to -5/3, several observational studies have found clear evidence for 3-D anisotropy of the turbulence (Chen et al., 2012; Vech and Chen, 2016; Verdini et al., 2018) suggesting that one might expect the structure to be unstable to the onset of reconnection at λ_D.

Mallet et al. (2017) suggested that the turbulent fluctuations are converted from sheet-like structures above λ_D to flux-rope-like (or vortex-like) structures just below λ_D – such "Alfvén vortex" structures have been observed in the solar wind just above the ion scales (Alexandrova, 2008; Lion et al., 2016; Perrone et al., 2016; Roberts et al., 2016; Perrone et al., 2017), although the exact mechanism generating these structures is a matter of debate. This significantly accelerates the cascade of the disrupted structures. In order to maintain constant energy flux through scale, the turbulent structures therefore adjust with a sudden drop in amplitude at the disruption scale. The flux-rope-like structures then cascade as is usual in Alfvénic turbulence, becoming progressively more sheet-like, and so on – until the scale at which the KAW dynamics take over, ρ_s. The relatively shallow spectral index associated with the usual Alfvénic dynamics present in this secondary cascade will act to "smooth out" the rapid drop in amplitude associated with disruption events. This smoothing is increasingly effective as the scale separation between λ_D and ρ_s increases; i.e., as the range of scales over which the usual Alfvénic dynamics apply becomes more important relative to the sudden drop in amplitude caused by disruption. Specifically, Mallet et al. (2017) predict that between λ_D and ρ_s, the power spectrum would be steeper than $k_\perp^{-3}$, becoming progressively steeper as $\lambda_D \to \rho_s$ from above (i.e., the spectrum is predicted to be steepest when β_e is only moderately low, so that is only slightly larger than ρ_s). Therefore, reconnection may fundamentally change the nature of the small scale fluctuations.

In this Chapter we use over 13 years of Wind spacecraft data to study the ion spectral break scale λ_B and dissipation-range spectral index, and how these depend on fundamental ion length scales ρ_i, ρ_s, d_i, ρ_c, and the disruption scale λ_D, as well as on the fundamental parameters $\beta_{\perp i}$ and β_e. We will show that, at least in terms of scalings, λ_D from the reconnection model Mallet et al. (2017) seems to correlate with the measured behavior of the break scale λ_B of the solar wind turbulent power spectrum better than any of the fundamental ion kinetic scales. In addition to this, the steepest spectral indices appear at moderately low β_e, and when λ_B is only slightly larger than ρ_s, as expected qualitatively from the reconnection model. Both of these observations suggest that reconnection may play an important role in the development of the dissipation range turbulent cascade.

5.2 Method

We use a statistical approach based on Wind spacecraft observations to study the variation of the break scale as a function of physical parameters. The investigated period extends from January 2004 to December 2016 during which Wind was in the pristine solar wind. The time series of the magnetic field (11 Hz) (Lepping et al., 1995), onboard ion moments, ion parameters (92 s cadence both) and electron moments (37 s cadence) (Lin et al., 1995; Ogilvie et al., 1995) were split into 10-min intervals ($\sim 5.8 \cdot 10^5$ intervals overall) and the averages of $\beta_{\perp i}$, β_e, d_i, ρ_i, ρ_s, and ρ_c in each interval were calculated.

To estimate λ_D, we use Equation 5.1, and assume that the break frequency between the energy-containing and inertial ranges is a constant 10^{-4} Hz (Podesta et al., 2007), calculating $L_\perp = V_{sw}/(2\pi 10^{-4})$. The average value of $L_\perp$ in our study is $7.4 \cdot 10^5$ km, in good agreement with previous studies, which suggest that $L_\perp \sim 10^6$ km under average solar wind conditions (Matthaeus et al., 2014). While we do not expect the outer scale to be truly constant over the 13 years of data, in practice this does not introduce a significant source of error in our estimate of , since it appears only as a nearly-constant factor of $L_\perp^{1/9}$ in Equation 5.1. We will determine the dimensionless

prefactor C_D in Equation 5.1 from the data.

For each interval, the power spectral density (PSD) of each magnetic field component was computed via Fourier transform and then the components were summed up to obtain the total PSD (Koval and Szabo, 2013). The spectral index and ion-scale break frequency (f_b) were identified using the approach of Vech et al. (2017). A sequence of 43 logarithmically spaced frequencies was generated from 0.1 to 5.17 Hz and 33 linear fits were made in frequency ranges between the ith and $i + 10$th elements of this sequence having a ratio of 2.55. From this set of fits, the steepest spectral index was selected and the low frequency end was identified as f_b. The overall distribution of f_b shows excellent agreement with the study of Markovskii et al. (2008) where f_b was identified manually for 454 solar wind intervals. The mean and standard deviation of the dissipation range spectral index is -2.99 ± 0.65 in excellent agreement with previous studies (e.g. Leamon et al., 1998; Smith et al., 2006). We note that we filtered out cases when the dissipation range spectral index and f_b were affected by the noise floor; see Vech et al. (2017).

5.3 Results

To study the scaling behavior of f_b as a function of physical parameters in Figure 5.1, we plot 2-D histograms of f_b normalized to frequencies corresponding to five scales of interest. In all panels, the data is binned in a 50x50 grid, and bins with fewer than 10 samples are discarded. For each 5% of the data (as binned by the quantity on the x-axis), the averages and standard deviation of the quantity on the $y-$axis are plotted, together with the best power law fit to the whole 2-D distribution of the raw data. These power-law exponents and their 95% confidence intervals from Figure 5.1 are summarized in Table 5.1.

Figures 5.1a and b show the ratio of the break frequency and the frequency corresponding to the convected ion gyroradius ($f_{\rho_i} = V_{sw}/(2\pi\rho_i)$) and ion inertial length ($f_{d_i} = V_{sw}/(2\pi d_i)$) as a function of $\beta_{\perp i}$, respectively. Our results agree with Chen et al. (2014): for solar wind intervals with $\beta_{\perp i} \ll 1$ the break closely aligns with f_{d_i} while in the $\beta_{\perp i} \gg 1$ case the break is closest

to f_{ρ_i}: however, this appears to be something of a coincidence – the white curves and the 2D histograms show no sign of "flattening" and becoming independent of $\beta_{\perp i}$ at high or low $\beta_{\perp i}$ in Figures 5.1a and b respectively. We therefore, find little evidence that the behavior of the break is truly explained by either ρ_i at $\beta_{\perp i} \gg 1$ or d_i at $\beta_{\perp i} \ll 1$. Indeed, the white lines in Figure 5.1 show no significant difference from the overall best fit power laws shown in black for any value of $\beta_{\perp i}$. Overall, the break frequency shows significantly stronger dependence on f_{ρ_i} than f_{d_i}: we will discuss one potential reason for the rather shallow dependence of f_b/f_{d_i} at the end of this section.

Figure 5.1c shows the ratio of f_b/f_{ρ_s} ($f_{\rho_s} = V_{sw}/(2\pi\rho_s)$) as a function of $\beta_{\perp i}$, respectively. Similarly to f_b/f_{ρ_i} and f_b/f_{d_i}, f_b/f_{ρ_s} has a clear dependence on $\beta_{\perp i}$. We therefore conclude that neither ρ_i, d_i, nor ρ_s can physically explain the behavior of the ion break scale in the solar wind.

On the other hand, Figures 5.1d shows that f_b/f_{λ_D} ($f_{\lambda_D} = V_{sw}/(2\pi\lambda_D)$) is nearly constant as a function of $\beta_{\perp i}$. This suggests that the ion break scale in the solar wind may be determined by λ_D given by Equation 5.1, as predicted by the reconnection model of Mallet et al. (2017). One obvious caveat to this is that the value of f_b/f_{λ_D} is significantly less than unity, by around half an order of magnitude, across the whole range of $\beta_{\perp i}$.

In Figure 5.1e, the frequency corresponding to the proton-cyclotron resonance scale ($f_c = V_{sw}/(2\pi\rho_c)$) also shows reasonable agreement with the break frequency across the entire distribution of $\beta_{\perp i}$: its best fit slope parameter is only slightly larger than that of f_b/f_{λ_D} (Table 5.1). Based on these observations alone, we can not conclusively identify if λ_D or ρ_c controls the break frequency.

Parameter	Fit	Confidence Interval
f_b/f_{ρ_i} vs. $\beta_{\perp i}$	0.377	[0.376, 0.379]
f_b/f_{d_i} vs. $\beta_{\perp i}$	-0.107	[-0.109, -0.106]
f_b/f_{ρ_s} vs. $\beta_{\perp i}$	0.219	[0.2183, 0.221]
f_b/f_{λ_D} vs. $\beta_{\perp i}$	0.046	[0.0454, 0.0479]
f_b/f_c vs. $\beta_{\perp i}$	0.099	[0.0979, 0.1005]
f_b/f_{λ_D} vs. $\beta_{\perp i}$	-1.9×10^{-4}	[-0.0020, 0.0016]
f_b/f_c vs. $\beta_{\perp i}$	0.1047	[0.1028, 0.1066]
β_i vs. T_e/T_p	-0.317	[-0.3200, -0.3156]

Table 5.1: Summary of the power-law fits shown in Figures 5.1,5.3 and 5.4.

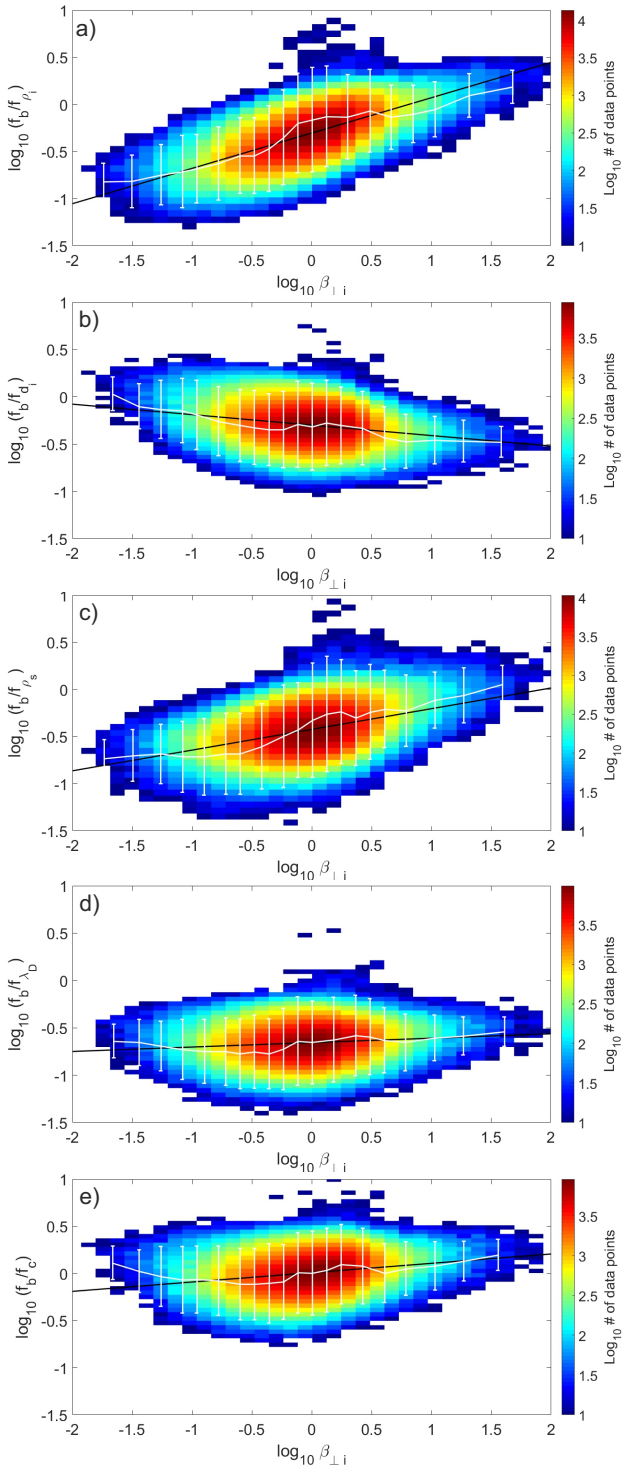

Figure 5.1: The 2-D histograms show the number of data points in each bin in the (a) (f_b/f_{ρ_i}, $\beta_{\perp_i}$), (b) (f_b/f_{d_i}, $\beta_{\perp_i}$), (c) (f_b/f_{ρ_s}, $\beta_{\perp i}$), (d) (f_b/f_{λ_D}, $\beta_{\perp i}$) and (e) (f_b/f_c, $\beta_{\perp i}$) grids, respectively. In each panel, least-square fits are indicated with black lines; their slopes are summarized in Table 5.1. For each 5% of the data (as binned by the quantity on the x-axis), the averages and standard deviation of the quantity on the $y-$axis are plotted in white.

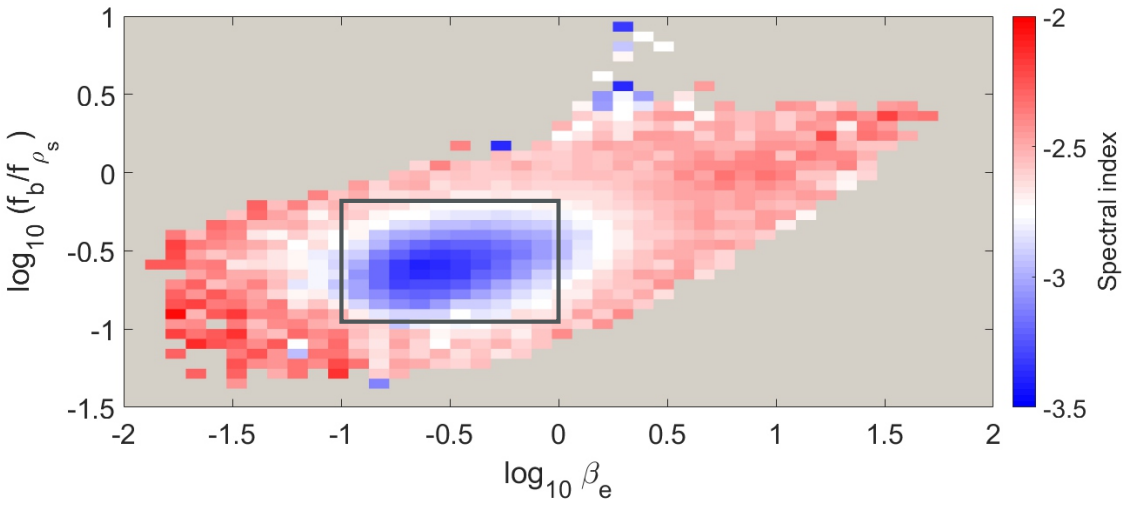

Figure 5.2: Spectral index of the dissipation range binned in the $(f_b/f_{\rho_s},\ \beta_e)$ plane. The black square marks the region with the steepest spectral indices in the range of $0.1 \lesssim \beta_e \lesssim 1$ and $0.12 \lesssim f_b/f_{\rho_s} \lesssim 0.63$.

In Figure 5.2 the $(f_b/f_{\rho_s}, \beta_e)$ plane is shown and the color represents the median dissipation range spectral index in each bin. The distribution indicates a significant steepening of the spectral index at "moderately" small β_e values between approximately 0.1 - 1, where f_b is slightly smaller than f_{ρ_s}. In this region the spectral indices are typically steeper than -3 in a narrow range just above the break (cf. Sahraoui et al., 2010). Mallet et al. (2017) predict that the steepest indices should be attained for β_e values just low enough that the reconnection-induced break occurs only just before the transition from AW to KAW (at the ion scale). Our technique (see Section 5.2) measures the spectral index over a fixed range of $[f_b, 2.55 \cdot f_b]$. If there is a steep subrange narrower than this just above the break, this approach cannot capture its true steepness. Due to this limitation in our fitting technique as well as the narrow range of scales involved, we are only able to claim qualitative similarity with the Mallet et al. (2017) prediction.

To resolve the ambiguous results obtained with Figure 5.1d and e, we repeat our analysis with the subset of the data within the black square in Figure 5.2, which encloses 41 % of the total data and is bounded by $0.1 \lesssim \beta_e \lesssim 1$ and $0.12 \lesssim f_b/f_{\rho_s} \lesssim 0.63$. The spectral indices are significantly steeper in this region, and if this is caused by reconnection then λ_B may have significantly better scaling with $_D$ in the marked region than with ρ_c. In Figure 5.3a the slope of the power-law fit for

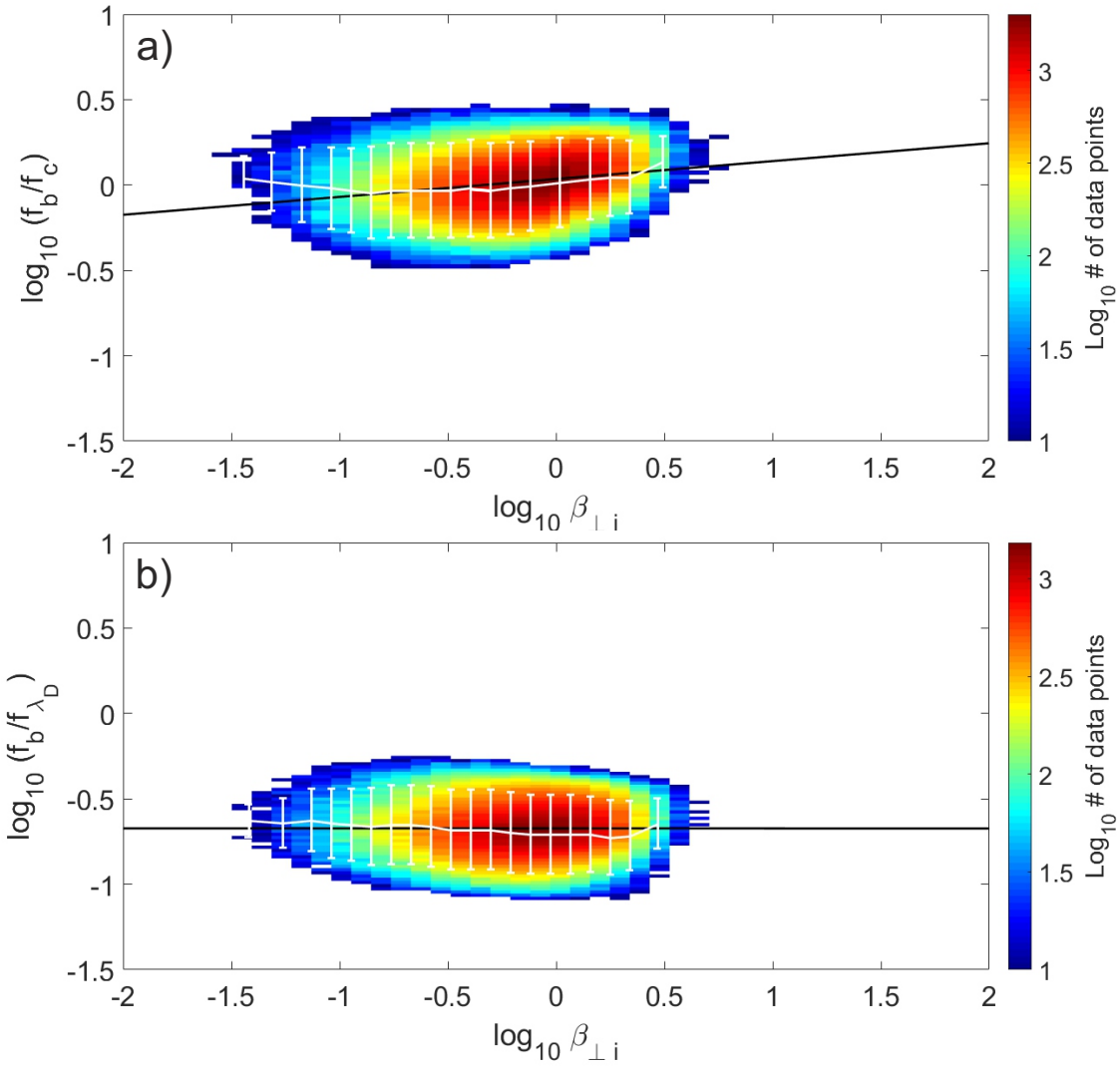

Figure 5.3: a) and b) are identical to Figure 5.1e and d, however they present the subset of measurements, which are within the black square in Figure 5.2 corresponding to 41% of the overall data points.

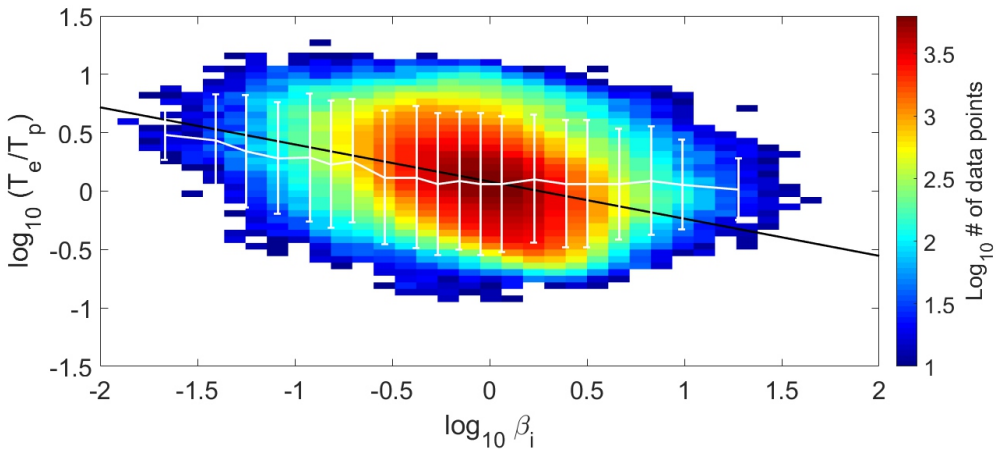

Figure 5.4: 2-D histogram showing the distribution of the measurements in the $(\beta_i, T_e/T_p)$ plane. The least-square fit is indicated with a black line and the average and standard deviation of each 5% of the data are marked in white.

f_b/f_c as a function of $\beta_{\perp i}$ closely agrees with the one based on the full distribution. In contrast, in Figure 5.3b the slope of the power-law fit for f_b/f as a function of $\beta_{\perp i}$ is remarkably close to 0. Based on this, we suggest that at least at low β_e magnetic reconnection may control the ion-scale break of the solar wind turbulence. The intercept of the power-law fit is $10^{-0.6728}$, implying $C_D = 4.7$ (see Equation 5.1).

Both f_b/f_{λ_D} and f_b/f_c were close to normally distributed in our data thus we use an F-test to investigate whether they have equal variance. The ratio of the sample variances is $F = \sigma^2_{(f_b/f_{\lambda_D})}/\sigma^2_{(f_b/f_c)} = 0.8398$ with 95 % confidence intervals of [0.8328; 0.8468]. Thus we reject the null hypothesis and conclude that λ_D predicts the break with smaller spread than ρ_c.

Finally, the scaling of f_b/f_{d_i} as a function of β_i, while significant over the whole range of β_i present in the data, is not particularly strong. With reference to the results of Chen et al. (2014), Mallet et al. (2017) pointed out that correlations between T_e/T_i and β_i could cause the scaling behavior of d_i to mimic that of λ_D. Neglecting a nearly constant factor $(L_\perp/\rho_s)^{1/9}$,

$$\frac{\lambda_D}{\rho_s} \propto \beta_e^{-2/9} \Rightarrow \frac{\lambda_D}{d_i} \propto \left(\beta_i \frac{T_e}{T_i}\right)^{5/18}, \tag{5.4}$$

and so if T_e/T_i were anticorrelated with β_i, the ratio λ_D/d_i would scale less strongly with β_i than

otherwise expected. Figure 5.4 shows that empirically, such an anticorrelation does in fact exist in the solar wind (at least at low β_i). Assuming that the break scale $\lambda_B \propto_D$ (as does appear to be the case: see Figures 5.1d and 5.3b), this contributes to the rather shallow scaling of f_b/f_{d_i} in Figure 5.1b. Similar consideration could contribute to the shallow scaling of f_b/f_c with $\beta_{\perp i}$.

5.4 Conclusion

In this Chapter we have presented a statistical study of the break scale λ_B between the inertial and dissipation ranges of the solar wind turbulence spectrum, and to what extent $_B$ agrees with the fundamental ion length scales ρ_i, d_i, ρ_s, ρ_c and the disruption scale λ_D (Equation 5.1), as a function of $\beta_{\perp i}$. Our results suggest that the ion-scale break of the solar wind turbulence may be controlled by magnetic reconnection in the low β_e (0.1-1) case, which is the main result of this Chapter.

The observed behavior of f_b/f_{ρ_i} and f_b/f_{d_i} as a function of $\beta_{\perp i}$ are consistent with previous studies based on more limited data sets (Chen et al., 2014; Wang et al., 2018): for $\beta_{\perp i} \ll 1$ the break occurs at the frequency of f_{d_i} and for $\beta_{\perp i} \gg 1$ the break is closest to f_{ρ_i}. However, both f_b/f_{ρ_i} and f_b/f_{d_i} showed significant dependence on $\beta_{\perp i}$ across the whole range of $\beta_{\perp i}$ present in the data, suggesting that the agreement with the break frequency in narrow ranges at the extremes of $\beta_{\perp i}$ is somewhat coincidental. Thus, we find little evidence that either ρ_i or d_i determine the break in the power spectrum. Similarly, f_b/f_{ρ_s} has a clear scaling with $\beta_{\perp i}$ and thus cannot explain the position of the break.

This contrasts with recent hybrid simulations by Franci et al. (2016) which found that for $\beta_{\perp i} \ll 1$, $\lambda_B \sim d_i$ independently of β_i, and for $\beta_{\perp i} \gg 1$, $\lambda_B \sim \rho_i$ independently of $\beta_{\perp i}$. We note, however, that their simulations may contain different physics than the true solar wind turbulence; they are two-dimensional, and also do not contain the electron inertial scale, which allows the reconnection to occur in the model of Mallet et al. (2017).

Comparing the break scale to the scale predicted by the reconnection model Mallet et al. (2017);

Loureiro and Boldyrev (2017), we found that f_b/f was nearly independent of $\beta_{\perp i}$. To obtain agreement in the magnitudes of λ_B and $_D$ a dimensionless prefactor $C_D = 4.7$ must be inserted into Equation 5.1 since this cannot be predicted from the simplified model in Mallet et al. (2017), which only predicts scalings. The ratio of the proton-cyclotron resonance scale ρ_c to the break scale showed a similarly shallow scaling with $\beta_{\perp i}$ and the best fit-slope was only a factor of 2.15 steeper than that of f_b/f_{λ_D}. Thus based on the whole distribution of the data we can not conclusively identify if λ_D or ρ_c controls the break frequency.

At high β_e, reconnection is not expected to cause a break (see Equation **??**); this could be why the agreement between λ_B and λ_D has a slight dependence on $\beta_{\perp i}$ using the whole dataset. We therefore repeated our analysis for a significant subset of the data (41 % overall) bounded by $0.1 \lesssim \beta_e \lesssim 1$ and $0.12 \lesssim f_b/f_{\rho_s} \lesssim 0.63$ displaying unusually steep spectral indices (steeper than -3), in qualitative agreement with the reconnection model of Mallet et al. (2017). For this subset of the data we found that λ_B scales with λ_D remarkably well while $\beta_{\perp i}$ changes two orders of magnitude. In contrast, ρ_c showed a clear correlation with $\beta_{\perp i}$ suggesting that at least at the low β_e case the break between the inertial and dissipation-range scales may be controlled by the onset of magnetic reconnection.

CHAPTER 6

Signatures of In-situ Generated Ion-scale Coherent Structures in the Solar Wind by Magnetic Reconnection

This Chapter is taken from Vech, D., A. Mallet, K. G. Klein, J. C. Kasper, Signatures of in-situ generated ion-scale coherent structures in the solar wind by magnetic reconnection, Submitted to the Monthly Notices of the Royal Astronomical Society.

The origin of ion-scale coherent structures in the solar wind is a matter of considerable debate, in particular whether they are passively advected from a distant source or are locally generated by non-linear processes. Here we investigate the possibility that disruption of Alfvénic turbulence by the onset of the tearing mode instability may lead to the formation of ion-scale coherent structures. We use a wavelet technique to identify ion-scale coherent structures with large amplitude magnetic fluctuations and study how their occurrence correlates with changes in the ion-scale spectral index and β_e. We find that ion-scale coherent structures occur most frequently when $0.2 < \beta_e < 0.8$ and the break scale is only slightly larger than the ion sound radius, which agrees with the parameters where magnetic reconnection may control the ion-scale spectral break of the turbulent spectrum. For these intervals the statistical properties of ion-scale turbulence are consistent with the presence of vortex-like structures. We suggest that the onset of collisionless magnetic reconnection significantly affects the nature of plasma turbulence around the ion gyroscale by generating small-scale

magnetic structures.

6.1 Introduction

Turbulence becomes progressively more inhomogeneous and nonuniform as energy cascades toward smaller scales (Frisch, 1995). These intermittent structures form sites for magnetic reconnection, particle heating, and particle acceleration; hence understanding their properties and origin is fundamentally important to describe the thermodynamics of the solar wind, solar corona and plasma systems more generally. Intermittency has been extensively studied both observationally (e.g. Sorriso-Valvo et al., 1999; Greco et al., 2009; Osman et al., 2010; Perri et al., 2012; Wang et al., 2013; Chasapis et al., 2015; Zheng and Hu, 2018; Chhiber et al., 2018) and numerically (e.g. Greco et al., 2008, 2012; Mallet and Schekochihin, 2016; Mallet et al., 2016; Cerri and Califano, 2017; Sorriso-Valvo et al., 2018; Camporeale et al., 2018). Intermittency arises as small-scale coherent structures including current sheets, rotational discontinuities and shocks. Recently much progress has been made toward the characterization and classification of ion-scale coherent structures (see Lion et al., 2016; Perrone et al., 2016; Roberts et al., 2016; Perrone et al., 2017; Wang et al., 2019). These studies found that intermittency, phase coherence and non-Gaussian fluctuations are strongly related. In addition to planar structures such as shocks and current sheets, vortex-like structures are also frequently observed, which may lead to unusually steep (approximately -4) spectral indices at ion-scale (Lion et al., 2016).

The origin of these intermittent structures in the solar wind is a matter of considerable debate, in particular whether they are passively advected by the solar wind or are locally generated by nonlinear processes. Bruno et al. (2001), Borovsky (2008) and Miao et al. (2011) argued that magnetic field rotations might be related to flux-tube boundaries, which are convected by the solar wind. In contrast, several studies found that the magnetic and velocity spectrum of solar wind turbulence (Boldyrev et al., 2012; Bowen et al., 2018) and the properties of discontinuities and intermittent structures such as their waiting times and angular distributions are consistent with self-generation

by magnetohydrodynamic (MHD) turbulence (Vasquez et al., 2007; Salem et al., 2009; Zhdankin et al., 2012; Zhdankin et al., 2013, 2016). Although these two models are not mutually exclusive, their relative importance is not well understood.

Vech et al. (2018) tested the reconnection model of Mallet et al. (2017) using 13 years of Wind data and found that λ_D has remarkably good correlation with the break scale when β_e is in the range of 0.1-1 and λ_D is only slightly larger than ρ_s; this situation occurrs 41 % of the time at 1 AU. The average of λ_D is approximately 218 km, which corresponds to $v_{sw}/(2\pi\lambda_D) \approx 0.31$ Hz in the spacecraft frame. We note that for this subset of the data β_i showed no preference and covered two orders of magnitude in the range of 0.03-3. During these intervals the ion-scale spectral index was steeper than -3 (measured in the frequency range of $[f_b, 2.55 \cdot f_b]$ where f_b is the break frequency), in qualitative agreement with the reconnection model. These results suggest that magnetic reconnection may control the ion-scale spectral break of solar wind turbulence, at least for the low β_e case.

In this Chapter we study the correlation between the spectral index, occurrence of ion-scale coherent structures and β_e. We find that 49% of the ion-scale coherent structures are observed when the ion-scale spectral index is steeper than -3, $0.2 < \beta_e < 0.8$ and the ratio of the break frequency and the frequency corresponding to the convected ion sound radius ($f_{\rho_s} = V_{sw}/2\pi\rho_s$) is in the range of 0.1-0.45 showing a complete overlap with the region where the model of Mallet et al. (2017) is thought to operate. Our results suggest that magnetic reconnection may be an important mechanism locally generating ion-scale coherent structures in the solar wind.

6.2 Method

To study ion-scale coherent structures we used Wind magnetic field (Lepping et al., 1995), ion (Ogilvie et al., 1995) and electron data (Lin et al., 1995) for a 2000 day period between 2005 January 1 and 2010 June 24. The background plasma parameters (ρ_s, β_e) were averaged for 10 min intervals and for each interval the frequency of the ion-scale spectral break and the spectral index

in the dissipation range was measured with the approach of Vech et al. (2017). For the further analysis of the magnetic field data, we split the 10 min intervals into 1 min intervals, the magnetic field components were rotated into the minimum variance (MVA) coordinate system (Sonnerup and Cahill, 1967) and the 1 min mean of each component was subtracted.

The magnitude-squared coherence (R_{ij}) between each pair of the magnetic field components ($R_{\perp_1||}$, $R_{\perp_2||}$, and $R_{\perp_1\perp_2}$) were computed using Morlet wavelets and the average magnitude-squared coherence was obtained in the range of $[0.4; 0.7]$ Hz. This frequency range was chosen such that it is comparable to the scale of the convected proton gyroradii and low enough so the noise floor does not affect the analysis. This technique identifies coherent structures, which affect at least two components of the magnetic field. To automatically identify ion-scale coherent structures we set the following two thresholds: $\delta b_{tot}^2 = \sum_{i=1}^{3} \delta b_i^2 > 1.37$ nT^2 where δb_i corresponds to the magnetic field components in the MVA frame after the mean has been subtracted and $R_{ij} > 0.76$ (see Lion et al., 2016; Perrone et al., 2017). Both thresholds correspond to 2σ of the measured distributions of R_{ij} and δb_{tot}^2, respectively.

For each one-minute interval we calculated the percentage of the measurements satisfying our two selection criteria and identified, which pair of magnetic field components had the highest coherence during that interval. Since the direction of the minimum variance is a very good approximation of the local magnetic field direction (e.g. Horbury et al., 1995) we suggest that the measured coherence can be used to differentiate between wave-like (e.g. ion-cyclotron waves) and coherent structures (e.g. Alfvén vortices). Ion-cyclotron waves (e.g. Jian et al., 2009; Wicks et al., 2016) are plane waves propagating along the magnetic field lines thus the two perpendicular magnetic components are phase coupled with high coherence between them. In contrast, coherent structures appear both in the field aligned and perpendicular components (Lion et al., 2016). We classified intervals as "coherent structures" when $\delta b_{tot}^2 > 1.37$ nT^2 and the largest magnitude-squared coherence is measured between the field aligned and any of the perpendicular components (e.g. $R_{||\perp_1}$ or $R_{||\perp_2} > R_{\perp_1\perp_2}$) while intervals with the highest coherence between the two perpendicular components are labeled as wave-like structures.

For each 10 min interval, the magnetic field time series were transformed with Morlet wavelet and the averaged PSD was obtained separately for the "coherent", "wave" and "non-coherent" intervals, an approach previously used by Lion et al. (2016). The contribution of the coherent structures to the global PSD was quantified at the break frequency (f_b), via

$$\Lambda = \frac{E(f_b)_{coherent}}{E(f_b)_{coherent} + E(f_b)_{non-coherent} + E(f_b)_{waves}}. \tag{6.1}$$

Changes in the magnetic field direction are either pure rotations or rotations with change in the strength of the magnetic field, which is closely related to the compressibility of the turbulence at the scale of interest. We use the proxy introduced by Zhdankin et al. (2012) and later also used by Chen et al. (2015) to understand the nature of the magnetic field rotations at ion-scale,

$$\chi(t,\tau) = \frac{|\delta B/B - 2\sin(\alpha/2)|}{\delta B/B} \tag{6.2}$$

where $\delta B/B = |\boldsymbol{B}(t+\tau) - \boldsymbol{B}(t)|/|\boldsymbol{B}(t)|$, $\tau = 2$ second (corresponding to the scale where R_{ij} and δb^2_{tot} are estimated) and α is the magnetic field rotation angle over time *t* and scale τ,

$$\alpha(t,\tau) = \cos^{-1}\left[\frac{\boldsymbol{B}(t)\cdot\boldsymbol{B}(t+\tau)}{|\boldsymbol{B}(t)|\cdot|\boldsymbol{B}(t+\tau)|}\right] \tag{6.3}$$

The value of χ is bounded by 0 and 1 where 0 corresponds to pure rotation while $0 < \chi \leq 1$ implies rotation with change in field strength.

6.3 Results

To study the occurrence of ion-scale coherent structures we used a 2D histogram with 50x50 bins in the (β_e, f_b/f_{ρ_s}) space. In each bin the median value was selected and bins with less than 10 data points were discarded. Figure 6.1 shows the distribution of the dissipation range spectral index estimated in the frequency range [f_b,2.55f_b], i.e. $\sim$ [0.3,0.8] Hz and the coherent time/total time ratios in the (β_e, f_b/f_{ρ_s}) space. Figure 6.1a indicates that the spectral indices steepen for the

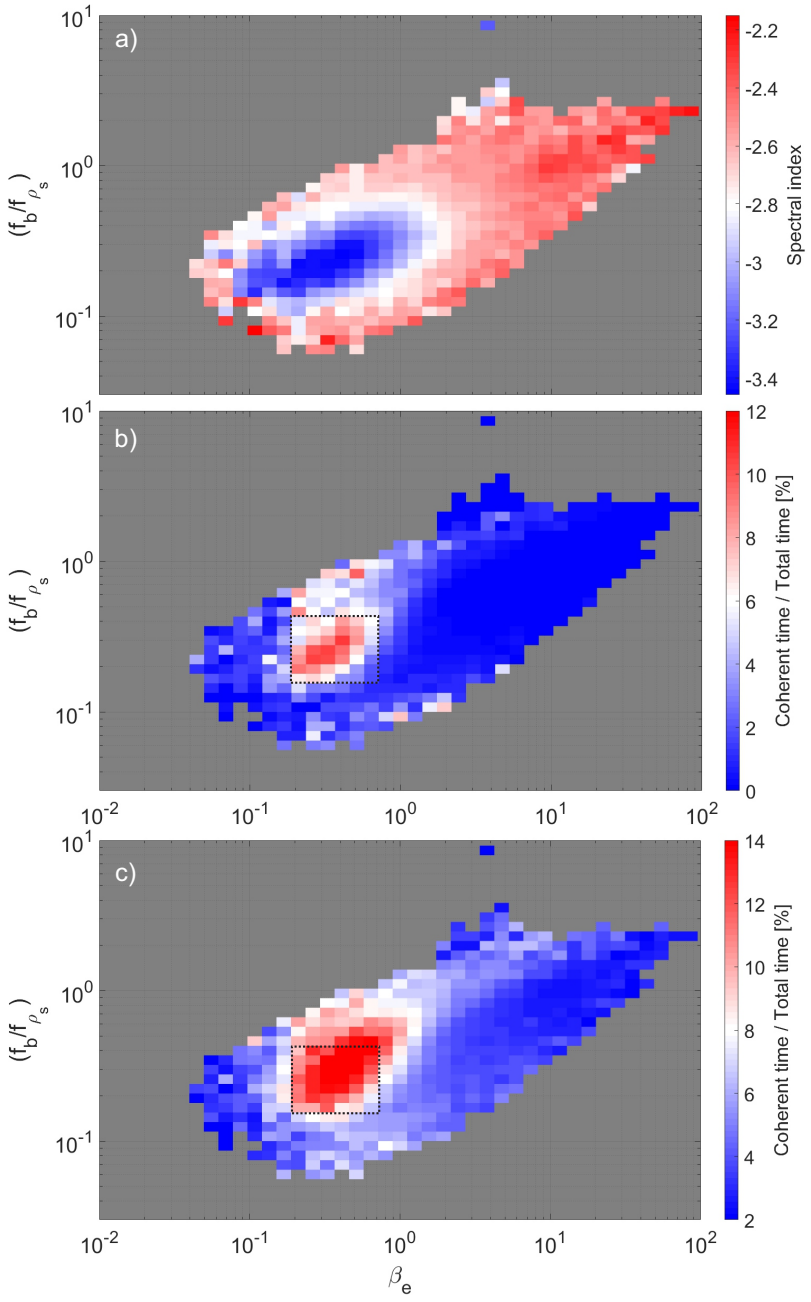

Figure 6.1: 2D histograms showing the distribution of the spectral index (a) and coherent time/total time ratios (excluding wave-like structures) (b) in the $(f_b/f_{\rho_s}, \beta_e)$ space. The dashed square in panel b) includes 20% of all data points and 49% of the observed coherent structures. Panel (c) shows the distribution of the coherent time/total time ratios when the $\delta b^2_{tot} > 1.37$ nT^2 selection criteria was dropped and all ion-scale coherent structures were identified (excluding wave-like structures). The dashed square includes 32% of the observed coherent structures

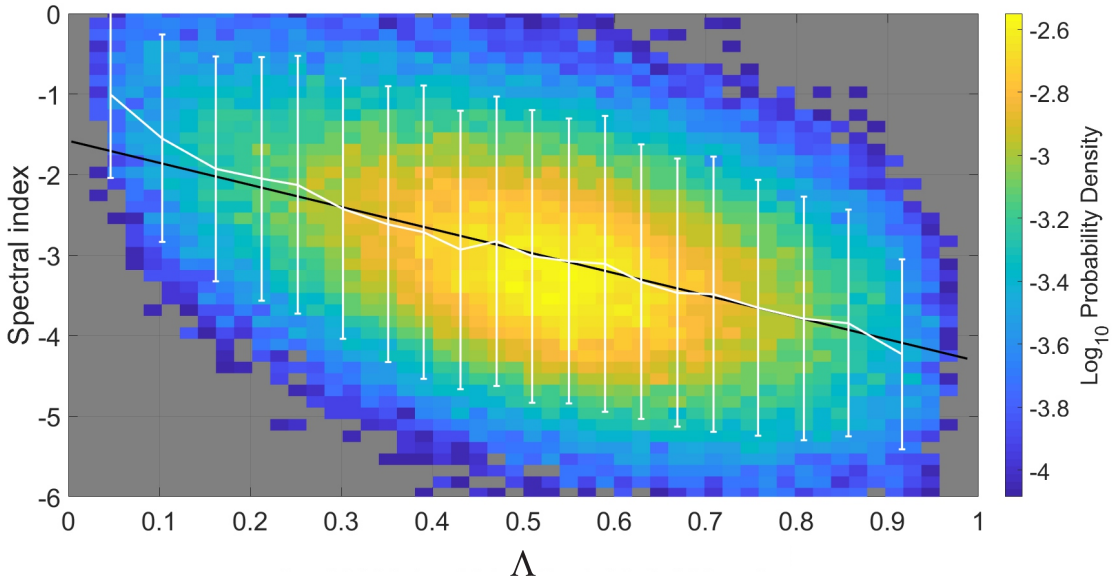

Figure 6.2: 2D histogram showing the probability density in the spectral index vs. Λ (Equation 6.1) space.

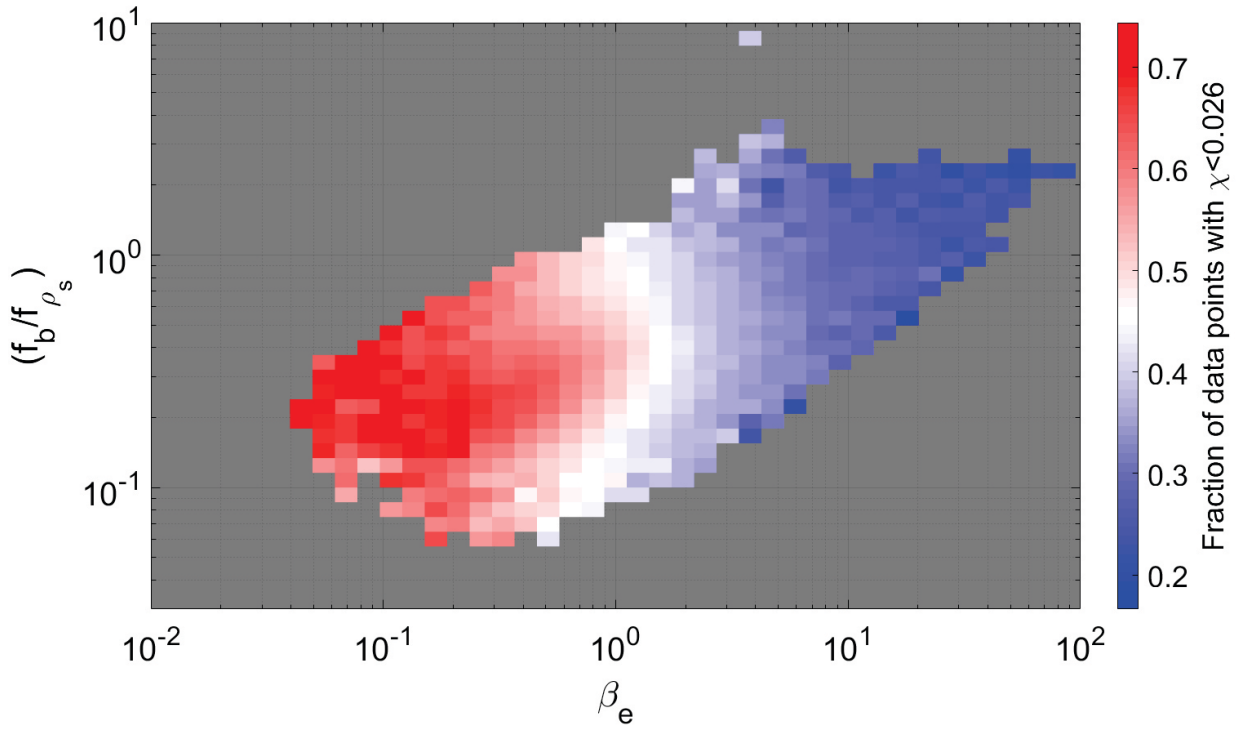

Figure 6.3: 2D histogram showing the fraction of data points with pure rotations at ion kinetic scale.

$0.1 < \beta_e < 1$, $0.1 < f_b/f_{\rho_s} < 0.5$ cases and reach approximately -3.5. Previously Vech et al. (2018) found that within that region the disruption scale (Equation **??**) has remarkably good correlation with the break scale while β_i changes two orders of magnitude (0.03-3), which is consistent with the hypothesis that magnetic reconnection may control the ion-scale spectral break for those plasmas. The distribution of the coherent time/total time ratio in the (β_e, f_b/f_{ρ_s}) space is shown in Figure 6.1b. The peak of the 2D histogram is approximately $\sim 12\%$ and aligns remarkably well with the region of the steepest spectral indices; outside the $0.1 < \beta_e < 1$ range the coherent time/total time ratio is typically below 2%. The dashed square in panel b) ($0.2 < \beta_e < 0.8$ and $0.1 < f_b/f_{\rho_s} < 0.45$) includes 20% of all data points and 49% of the observed coherent structures. We note that overall "coherent" and "wave-like" structures are observed in 4.3% and 1.3% of the time, respectively. The distribution of the wave time/total time ratio in the (β_e, f_b/f_{ρ_s}) space is qualitatively similar to Figure 6.1b with a peak wave time/total time ratio of approximately 2% in the region marked with the dashed square. In order to complement the analysis in Figure 6.1b the $\delta b^2_{tot} > 1.37$ nT^2 selection criteria was dropped therefore all ion-scale coherent structures were identified (excluding wave-like structures). The distribution of the coherent time/total time ratios in Figure 6.1c shows a slightly broader peak and there are signatures of small amplitude ion-scale coherent structures in the $\beta_e > 1$ range as well, which were not identified in Figure 6.1b. The black square includes 32% of the observed coherent structures.

The effect of the ion-scale coherent structures on the spectral index is shown in Figure 6.2: the data was binned in a 50x50 grid defined by the spectral index and Λ (Equation 6.1), the colors represent the probability density of the data points in each bin, for each 5% of the data the mean and standard deviation are plotted on the y-axis, the least-square fit ($y = -2.73x - 1.58$) is indicated with a black line. The y intercept of the least-square fit shows that in the absence of coherent structures the spectral index is in the range of [-5/3, -3/2] implying that for these rare cases there may be no well-defined spectral break in the studied frequency range ($[f_b, 2.55 \cdot f_b]$) of the turbulent spectrum. The peak of the distribution at $\Lambda = 0.5$ (which has a corresponding coherent time/total time ratio of $\sim$ 7% for the $\delta b^2_{tot} > 1.37$ nT^2 data set) also shows that on average the ion-scale

coherent structures contribute approximately half of the PSD at the break frequency.

While Figure 6.1 characterized the nature of Alfvénic fluctuations in the (β_e, f_b/f_{ρ_s}) space, in Figure 6.3 we investigate the compressibility of the ion-scale magnetic field fluctuations. Figure 6.3 shows the fraction of data points with $\chi \leq 0.026$, which effectively means the fraction of data points with pure rotations when the field strength is nearly constant. The 0.026 threshold corresponds to the median value of χ based on all the data points. In Figure 6.3 the ion-scale turbulence becomes progressively more Alfvénic with decreasing β_e. The region with the highest coherent time/total time ratios in Figure 6.1b are characterized primarily by pure rotations of the magnetic field, suggesting that any structures might be generated by reconnection are incompressible. We note that if β_e is replaced with β_i the overall distribution is qualitatively similar, however there is significantly more scattering. Previously, Perrone et al. (2016) presented case studies of ion-scale coherent structures in a solar wind stream with $\beta_e \sim 1.3$ and found that some of those structures are compressible ($\delta b_{||} \gg \delta b_{\perp}$). Later Perrone et al. (2017) investigated a solar wind stream with $\beta_e \sim 0.35$ and found that the ion-scale turbulence was dominated by Alfvénic structures with low compressibility ($\delta b_{||} < \delta b_{\perp}$). Figure 6.3 is consistent with these observations and shows that the nature of the ion-scale field rotations significantly depends on β_e.

6.4 Conclusions

In this Chapter we found that the occurrence of ion-scale coherent structures coincides with the region where the reconnection model of Mallet et al. (2017) may operate. The unusually steep spectral indices and properties of ion-scale turbulence such as significant magnetic field rotations and incompressible fluctuations are consistent with the presence of vortex-like structures, which have an expected spectral index of -4 Alexandrova (2008). Current sheets may also contribute to the power of the turbulent spectrum at the break scale, since a large fraction of the energy of magnetic fluctuations is concentrated in the vicinity of those structures Borovsky and Podesta (2015). Our statistical results about the spectral steepening and ion-scale coherent structures are

also consistent with the case studies of Lion et al. (2016) and Perrone et al. (2016).

We found a simple linear relationship between the contribution of ion-scale coherent structures to the power spectrum and the spectral index, which implies that in the absence of those small-scale structures there may be no ion-scale break in the turbulent spectrum in the frequency range of 0.1-1 Hz. On average the ion-scale coherent structures contribute approximately 50% to the power spectrum of magnetic fluctuations at the break scale. The characteristics of the ion-scale coherent structures show significant variability in the (f_b/f_{ρ_s}, β_e) space: first, in the high β_e limit ($\beta_e > 1$), ion-scale coherent structures occur rarely (coherent time/total time ratio was below 2%), turbulence is highly compressible at ion-scales and magnetic field rotations are typically accompanied with a change in the strength of the field. When the selection criteria on δb^2_{tot} was dropped we found signatures of ion-scale coherent structures in the $\beta_e > 1$ range suggesting that formation of current sheets may affect the turbulence in those intervals as well. Secondly, the "moderately low" β_e ($0.2 < \beta_e < 0.8$ and $0.1 < f_b/f_{\rho_s} < 0.45$) region is where 49% of the arge amplitude ($\delta b^2_{tot} > 1.37$ nT^2) ion-scale coherent structures are observed, the coherent time/total time ratio reaches approximately 12% and the ion-scale turbulence is dominated by Alfvénic structures.

In the near future Parker Solar Probe Fox et al. (2016) will provide measurements from the inner-heliosphere and our analysis will be extended to the $\beta_e \ll 1$ range. A study of the radial dependence of ion-scale coherent structures will provide conclusive evidence whether they are locally generated by turbulence or are primarily convected by the solar wind.

CHAPTER 7

Kinetic Scale Spectral Features of Cross Helicity and Residual Energy in the Inner Heliosphere

This Chapter is taken from Vech, D., J.C. Kasper, K. G. Klein , J. Huang, M.L. Stevens, C.H.K. Chen, A.W. Case, K. Korreck, S.D. Bale, T.A. Bowen, P. Whittlesey, R. Livi, D.E. Larson, D.M. Malaspina, M. Pulupa, J.W. Bonnell, P.R. Harvey, K. Goetz, T.D. de Wit, R. MacDowall, Kinetic Scale Spectral Features of Cross Helicity and Residual Energy in the Inner Heliosphere, Under Review in the Astrophysical Journal Supplement Series, 2020.

In this Chapter, we present the first results from the Flux Angle operation mode of the Faraday Cup instrument onboard Parker Solar Probe. The Flux Angle mode allows rapid measurements of phase space density fluctuations close to the peak of the proton velocity distribution function with a cadence of 293 Hz. This approach provides an invaluable tool for understanding kinetic scale turbulence in the solar wind and solar corona. We describe a technique to convert the phase space density fluctuations into vector velocity components and compute several turbulence parameters such as spectral index, residual energy and cross helicity during two intervals the Flux Angle mode was used in Parker Solar Probe's first encounter at 0.174 AU distance from the Sun.

7.1 Introduction

The solar wind is a hot, tenuous plasma propagating away from the Sun's surface, which is ubiquitously observed in a turbulent state (Coleman Jr, 1968). Turbulence in the solar wind is modelled as a cascade of energy from the outer scales to the much smaller dissipative scales through an inertial range. In the inertial range the velocity and magnetic fluctuations are largely perpendicular to the local magnetic field direction and the spectral index of the power spectra of the magnetic and velocity fluctuations are close to -5/3 and -3/2, respectively (Coleman Jr, 1968; Matthaeus and Goldstein, 1982; Podesta et al., 2007; Boldyrev et al., 2011). Below this range roughly coincident with the convected ion kinetic scales the magnetic energy spectrum steepens and Alfvénic turbulence undergoes a transition into dispersive kinetic Alfvén waves (KAW) (Bale et al., 2005; Chen et al., 2013). Between ion and electron scales the spectral index of the magnetic fluctuations is typically between -2 and -4 (Leamon et al., 1998; Smith et al., 2006; Alexandrova et al., 2009; Matteini et al., 2016).

In contrast to magnetic fields, the power spectrum of velocity fluctuations in the kinetic range is much less understood due largely to the fact that high cadence plasma moment measurements in the solar wind became only recently available. Studies based on Spektr-R data (proton moments with 31 ms cadence measured by six Faraday Cups) presented the first results on the high frequency part (up to 2 Hz) of the velocity power spectrum including break frequency and spectral indices (Šafránková et al., 2013, 2016; Riazantseva et al., 2017). Unfortunately the lack of an operating magnetic field instrument of Spektr-R made it impossible to study correlation between high frequency velocity and magnetic fluctuations and compute cross helicities and residual energies.

Cross helicity is defined as $\sigma_c = (E^+ - E^-)/(E^+ + E^-)$ where $E^{\pm}$ corresponds to the power spectra of the Elsasser variables $\mathbf{z}^{\pm} = \delta\mathbf{v} \pm \delta\mathbf{b}/\sqrt{\mu_0 \rho}$ where $\delta\mathbf{v}$ and $\delta\mathbf{b}$ are the fluctuations of the velocity and magnetic fields in Alfvén units, respectively and ρ is the mean mass density of protons (Wicks et al., 2013; Chen et al., 2013). Cross helicity is normalized in such a way that it is 1 and -1 for anti-Sunward and Sunward propagating waves, respectively. Cross helicity is conserved in the absence of dissipation and corresponds to the linkages between lines of vorticity

and magnetic field lines, both of which are frozen to the fluid flow in the absence of dissipation (Chandran, 2008).

Residual energy is the difference between the kinetic and magnetic energy $\sigma_r = (E^v - E^b)/(E^v + E^b)$. Unlike for pure Alfvén waves (Alfvén, 1942) where the energy of velocity and magnetic fluctuations are in equipartition, in the solar wind the magnetic energy is typically larger than the energy of velocity fluctuations (Wicks et al., 2013; Chen et al., 2013). The origin of this difference is a matter of considerable debate: potential explanations include the role of magnetic structures with solar origin and local generation of residual energy by counterpropagating Alfvén wave packets (Wang et al., 2011; Boldyrev et al., 2012; Bowen et al., 2018).

Understanding the scaling of σ_r and σ_c in the kinetic-scale solar wind fluctuations is fundamentally important for describing heating and dissipation in the solar wind, solar corona and plasma systems more generally. Previous turbulence models (e.g. Boldyrev, 2006; Matthaeus et al., 2008) described the coupling between velocity and magnetic field fluctuations in the inertial range, however the main assumptions underlying these models are violated at the kinetic scales where the MHD approximation breaks down and the quadratic integral invariants are no longer retained (Matthaeus and Goldstein, 1982). To the best of our knowledge no theory exists that describes the correlation between velocity and magnetic fluctuations in the kinetic range. The first attempt to measure σ_c and σ_r in the kinetic range was presented by (Parashar et al., 2018) using Magnetospheric Multiscale Mission (MMS) data. They found that σ_r and σ_c converge to 1 and 0, respectively from the inertial range to the smallest observable scales (20-40 km). The loss of alignment between $\delta\mathbf{v}$ and $\delta\mathbf{b}$ (quantified by the metric $cos(\theta) = \sigma_c/\sqrt{(1-\sigma_r^2)} \approx 0$) was explained by the demagnetization of protons.

The Faraday Cup (SPC) instrument (Kasper et al., 2016; Case and the SWEAP team, 2019) onboard NASA's Parker Solar Probe (PSP) (Fox et al., 2016) is equipped with a novel Flux Angle (FA) operation mode that allows rapid measurements of the phase space density fluctuations with an unprecedented 293 Hz cadence providing a new tool to understand kinetic scale turbulence in the solar wind and solar corona. SPC was operated in FA mode twice for approximately a total

of 110 seconds during the first perihelion of PSP on 4th November 2018 and captured the fine structure of a magnetic switchback. Magnetic switchbacks are one of the most prominent features of the solar wind in the inner heliosphere; they are characterized by short, large amplitude velocity enhancements that are accompanied with 90-180° rotation of the magnetic field (Gosling et al., 2011; Horbury et al., 2018; Horbury et al., 2019). These structures might be direct signatures of impulsive chromospheric or coronal energy release (Horbury et al., 2018; Bale and the FIELDS team, 2019).

In this Chapter, we present the first results from the FA operation mode of SPC and study σ_c and σ_r in the kinetic range of the turbulent cascade. Our study complements the ones by Chen et al. (2019) and Parashar et al. (2019), which focus on magnetic and velocity fluctuations on MHD scales in the inner heliosphere. In Section 7.2 we describe the conversion of phase space fluctuations into vector velocity fluctuations, with particular emphasis on the underlying assumptions and limitations of the data product. In Section 7.3, we discuss the properties of kinetic scale turbulence in the observed magnetic switchback such as spectral index of the power spectrum, residual energy and cross helicity. Finally, Section 7.4 contains a summary and a discussion of the results.

7.2 Method

The Faraday Cup instrument of PSP measures fluxes and flow angles as a function of energy from 50 eV/q to 8 keV/q for ions (Kasper et al., 2016; Case and the SWEAP team, 2019) based on the currents detected by four collector plates. In typical operation mode SPC scans through 128 energy per charge windows in 0.87 seconds (1.14 Hz); higher cadence data products ($\sim$5-19.6 Hz) are available for shorter intervals as well. In FA mode SPC measures a single energy/charge window near the center of the proton velocity distribution function (VDF) with 293 Hz cadence.

Figure 7.1 shows an overview of the components of the magnetic field (293 Hz cadence based on fluxgate magnetometer data, (Bale et al., 2016)) and velocity for a 3 hr period starting on November 4th 2018 14:00:00 UT when PSP was approximately at 0.174 AU distance from the Sun.

The vector components are in the RTN coordinate system where R points radially outward from the Sun, N is along the ecliptic North and T completes the right hand coordinate system. A magnetic switchback was observed from 15:24:01 to 15:43:07 and was accompanied with a sudden reversal of the radial magnetic field component and enhanced (toward the positive T direction) tangential velocity component. The duration of the studied magnetic switchback (e.g. interval with $B_R > 0$ nT) is approximately 19 minutes, which is considered to be an above average structure (see Kasper and the SWEAP team, 2019). In Figure 7.1 the shaded region marks the two intervals where SPC was operated in FA mode between 15:31:54-15:32:53 and 15:33:30-15:34:22 UT.

Figure 7.2 shows 15-second averages of proton VDFs before each FA mode interval where x-axis is the phase speed and y-axis is the phase space density (P) in arbitrary units (for the conversion of the axes see Case and the SWEAP team (2019)). The FA mode achieves unprecedented temporal resolution by scanning a single window in phase space near the peak of the VDF, which are marked with blue (446-457 km/s) and red (426-437 km/s) for the first and second FA mode intervals, respectively. Significant changes in the solar wind parameters shift the VDF hence the blue and red regions do not align with the peak, which makes the interpretation of the FA mode measurements more complicated. To ensure that the FA mode interval is not affected by those large changes, we studied the variability of the solar wind parameters and compared 15-second averages of the solar wind speed (V_{sw}), core proton density (n_p), core thermal velocity (V_{th}), ratio of thermal to magnetic pressure (β_p) and Alfvén speed (V_A), which are summarized in Table 1. The solar wind parameters were very steady during the studied periods and none of them show variations of more than 5% suggesting that SPC measured approximately the same part of the VDF throughout in the FA mode intervals. We note that the proton core temperature anisotropy ($T_\perp/T_{||}$ estimated with 10-sec cadence, for details see Huang and the SWEAP team (2019)) was in the range of 0.96-1.07 for both intervals.

The measured P fluctuations during the FA mode might be caused by changes in V_{sw} and n_p. We use the following approach to disentangle the relative importance of these two parameters: full proton VDFs from 15:31:39 to 15:34:37 UT (starting 15 seconds before the first and ending 15

Parameter	Before #1	After #1	Before #2	After #2
V_{sw} [km/s]	423.5 $\pm$5.3	415.9 $\pm$12.1	406.7 $\pm$4.1	421 $\pm$4.2
n_p [cm^{-3}]	231.5 $\pm$16.9	230.1 $\pm$19.4	241.3 $\pm$9.8	231.7 $\pm$16.7
V_{th} [km/s]	78.0 $\pm$5.7	82.7 $\pm$5.9	85.9 $\pm$3.4	81.7 $\pm$5.7
β_p	0.6 $\pm$0.17	0.63 $\pm$0.16	0.71 $\pm$0.08	0.77 $\pm$0.2
V_A [km/s]	102.1 $\pm$5.1	104.7 $\pm$4.6	102.3 $\pm$2.2	96.9 $\pm$3.5

Table 7.1: 15-second averages and standard deviations of solar wind parameters before and after each FA mode interval.

seconds after the second FA mode interval) were selected where plasma moments (including V_{sw} and n_p) were available. Multiple linear regression was used to measure the dependence of P in the 445-457 km/s and 426-437 km/s windows on V_{sw} and n_p (e.g. Myers and Myers, 1990). The predictor (V_{sw} and n_p) and response (P) variables were standardized (subtracting the mean and dividing by the standard deviation) to ensure the correct interpretation of the coefficients. We used the $P = c_0 + c_1 V_{sw} + c_2 n_p + \epsilon$ linear model where ϵ is the error term. For the first FA mode interval we found that $c_{V_{sw}}$ =0.955 [0.90; 1.00] and c_{n_p} = 0.05 [-0.01; 0.11], respectively while for the second interval $c_{V_{sw}}$ = 0.57 [0.48; 0.67] and c_{n_p} = 0.04 [-0.04; 0.12]. These results suggest that the observed phase space density fluctuations in the FA mode intervals are primarily due to changes in V_{sw} and the contribution of n_p fluctuations is negligible.

A linear fit was used to estimate the scaling of P with V_{sw} based on the full proton VDF measurements from 15:31:39 to 15:34:37 UT. For the fitting, the phase space densities in the 445-457 km/s and 426-437 km/s windows were normalized by their mean values based on the entire interval ($\tilde{P}$ = $P/< P >$). We used the V_{sw} = (L$\cdot\tilde{P}$) + M linear model and found that for the first and second intervals the slopes ($L_{1,2}$) and intercepts ($M_{1,2}$) of the fits are: L_1 = 111.3 $\pm$ 3.96 km/s, M_1 = 313.8 km/s and L_2 = 89.1 $\pm$ 11.6 km/s, M_2 = 335.5 km/s, respectively.

Finally, the vector velocity components in the RTN frame were obtained as

$$V_R = [cos(\phi) \cdot cos(\theta) \cdot ((L_{1,2} \cdot \tilde{P}_{FA_{1,2}}) + M_{1,2})] - V_{R_{S/C}} \tag{7.1}$$

$$V_T = [cos(\phi) \cdot sin(\theta) \cdot ((L_{1,2} \cdot \tilde{P}_{FA_{1,2}}) + M_{1,2})] - V_{T_{S/C}} \tag{7.2}$$

$$V_N = [sin(\phi) \cdot ((L_{1,2} \cdot \tilde{P}_{FA_{1,2}}) + M_{1,2})] - V_{N_{S/C}} \tag{7.3}$$

$$\phi = \frac{2\pi}{180}[\frac{(C+D)-(A+B)}{A+B+C+D}] \tag{7.4}$$

$$\theta = \frac{2\pi}{180}[\frac{(A+D)-(B+C)}{A+B+C+D}] \tag{7.5}$$

where ϕ and θ are the elevation (angle measured from the R-T plane toward the N+ direction) and azimuth (angle measured in the R-T plane from the R+ direction toward T+ direction) angles of the flow, which are derived based on the current differences between the four collector plates (A,B,C,D) of SPC (for details see Case and the SWEAP team (2019)). $\tilde{P}_{FA}$ is the normalized phase space density during each FA mode interval, and $V_{i_{SC}}$ is the i^{th} component of the spacecraft velocity in the RTN frame ($V_{R_{SC}}$ = 18.17 km/s, $V_{T_{SC}}$ = -90.7 km/s, $V_{N_{SC}}$ = -4.1 km/s during both intervals).

The amplitude of the derived vector velocity fluctuations is validated the following way: we selected 190 seconds of data between 15:28:44-15:31:54 and 15:34:33-15:37:32 (e.g. measurements right before and after the first and second FA mode intervals, respectively) when SPC measured full VDFs with 19.6 Hz cadence. The length of this interval was chosen such that it is long enough to cover the inertial range of the fluctuations but also all data points are within the magnetic switchback. The trace power spectrum of the velocity fluctuations was computed for the 19.6 Hz data in the magnetic switchback and compared to the spectrum of fluctuations derived from the FA mode data. The results in Figure 7.3 suggest that two data sets have remarkably good agreement for low frequencies (below 1 Hz) for both the first (a) and second (b) FA mode intervals. The power spectrum of the 19.6 Hz cadence data reaches the noise floor at approximately 0.7 Hz and spectrum becomes shallow while the FA mode spectrum reaches the noise floor at approximately 7 Hz for the first and second intervals, respectively.

We compared the measured (based on the moments derived from the full VDFs) and estimated

(using the phase space densities in the 445-457 km/s and 426-437 km/s ranges) vector velocity components for 15:28:44-15:31:54 and 15:34:33-15:37:32. Table 2 summarizes the linear correlation coefficients, median offsets (δV=|V$_{measured}$ - V$_{estimated}$|) and spread of the δV distributions (σ). The results suggest that the estimated velocity components are in good qualitative and quantitative agreement with the velocity moments derived from the full VDFs.

Parameter	Correlation	Median δV	σ
V_R	0.78 / 0.43	0.70 / 0.02 km/s	6.29 / 10.5 km/s
V_T	0.67 / 0.58	5.14 /5.17 km/s	3.97 /4.0 km/s
V_N	0.85 / 0.85	3.06 / 3.05 km/s	4.35 / 4.37 km/s

Table 7.2: Correlation of the measured and estimated velocity components for the first and second FA mode intervals, respectively.

7.3 Spectral features of kinetic scale turbulence

Figure 7.4a and b show the power spectrum of the trace velocity and magnetic fluctuations. The magnetic field fluctuations were converted into Alfvén units normalizing by $(\mu_0\rho)^{1/2}$. The vertical lines mark the scale of the convected ion inertial length ($V_{sw}/2\pi d_i$) and proton gyoradius ($V_{sw}/2\pi\rho_i$) where $d_i = c/\omega_p$ and $\rho_i = mv_\perp/qB$. The black and green dots show the V and B-field spectral indices based on a fitting window, which has a size of a factor of 3.7; the dots are placed at the center of each fitting window.

In the inertial range (0.1-1 Hz) the spectral indices of the velocity and magnetic fluctuations are -1.51 / -1.61 and -1.60 / -1.74 for the first and second intervals, respectively. These values are close to the observations at 1 AU where magnetic field spectrum is typically steeper than the velocity (Boldyrev et al., 2011; Chen et al., 2013; Bowen et al., 2018). The ion-scale spectral break of the magnetic field power spectrum is approximately 5 and 2 Hz in the first and second intervals, respectively, which are at least a factor of six larger than the typical values at 1 AU ($\approx$ 0.3 Hz, (e.g. Markovskii et al., 2008; Vech et al., 2017)). This suggests again that the FA mode is essential to study the δ**v**-δ**b** coupling in the kinetic range since velocity fluctuations at these scales are not

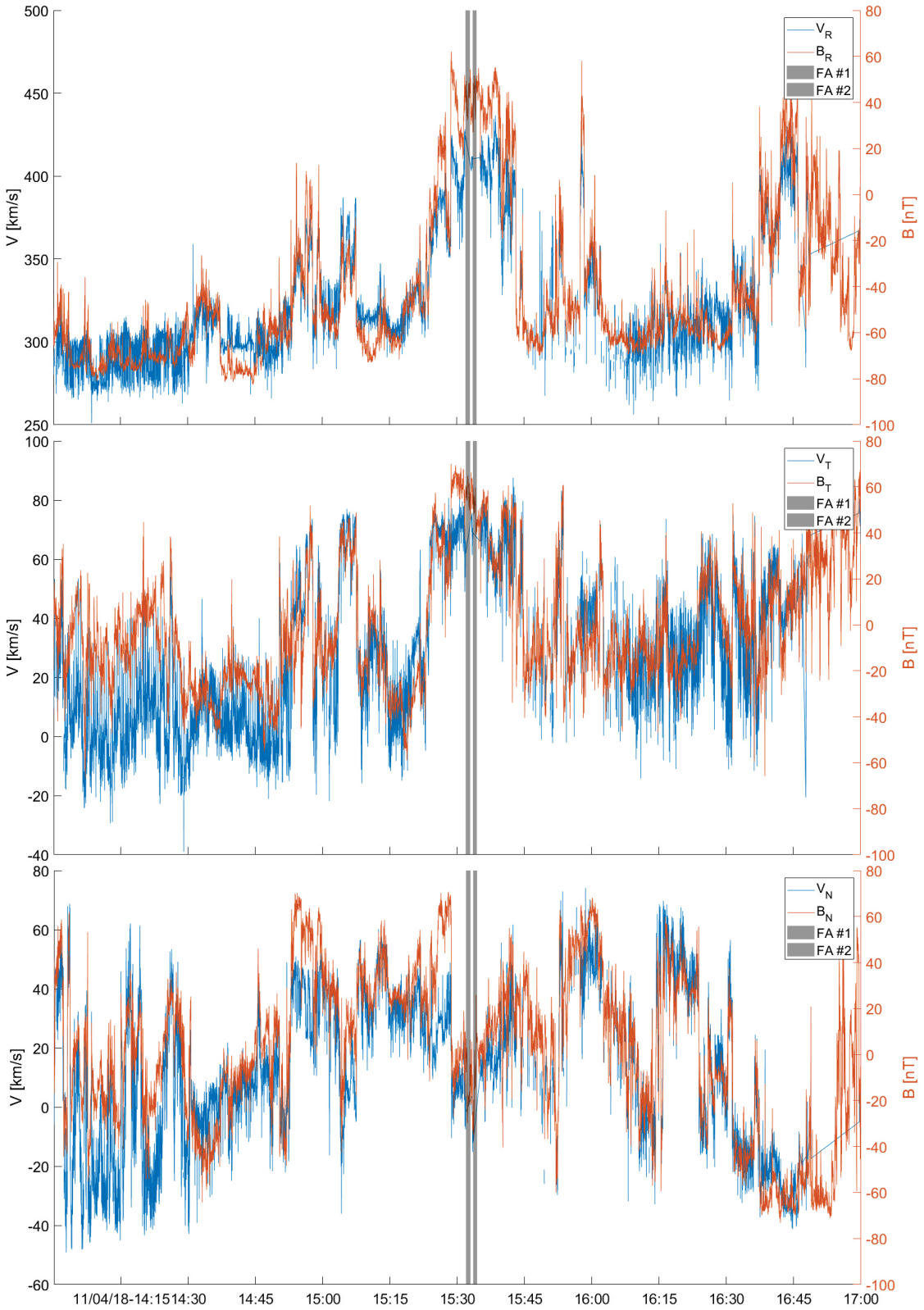

Figure 7.1: Overview of the magnetic and velocity components in a 3hr interval centered at the FA mode data.

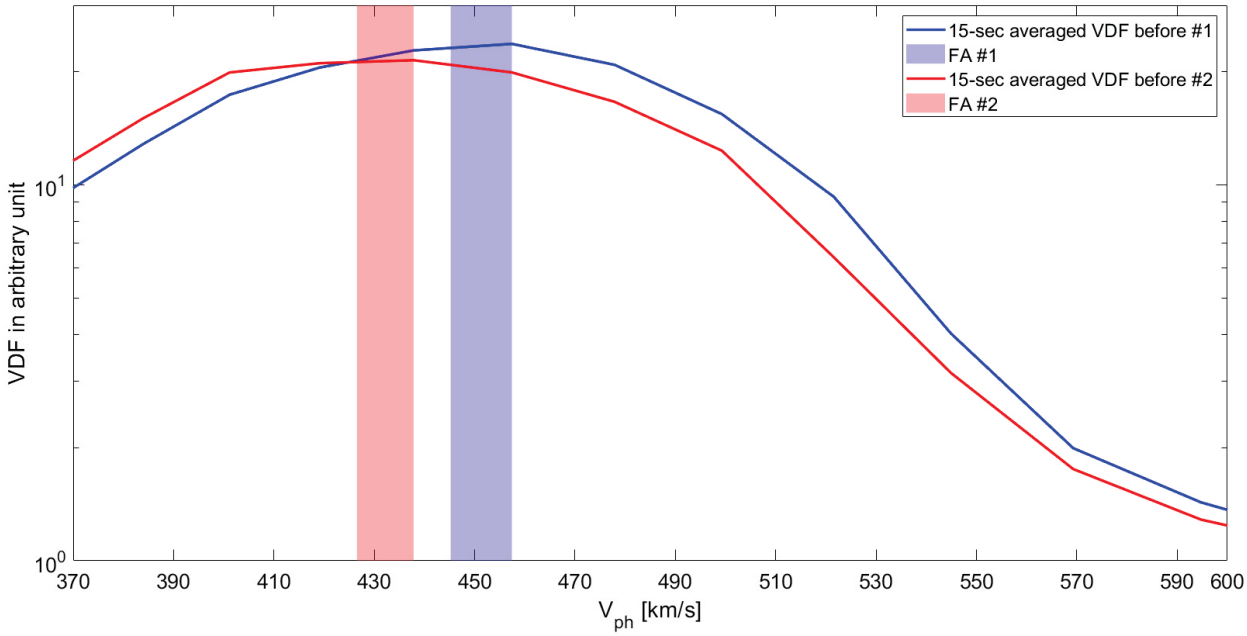

Figure 7.2: 15-second averages of full VDFs before each FA mode interval, respectively. The shaded areas mark the range in phase speed, which are measured in the FA mode.

measured with other operation modes of SPC.

The V and B-field spectral indices show good correlation in the inertial range; at kinetic scales the B-field spectral index is around -2.5 and -3, which is similar to the observations at 1 AU (e.g. Alexandrova et al., 2009; Leamon et al., 1998), in contrast at kinetic scales we find no signatures of spectral steepening in the V-field power spectrum. Previous studies found that the power spectrum of ion fluxes show very wide range of features: Riazantseva et al. (2017) categorized power spectrums of ion fluxes into five groups using Spektr-R data at 1 AU. The most frequently occurring spectra (50% of the cases) showed two slopes and one break point between them at ion-scale, the second most frequent class (32%) showed flattening in the vicinity of the break. In contrast, 6.3% of power spectras did not show steepening at kinetic scales at all. Riazantseva et al. (2017) did not find clear trend (such as V_{sw} or β_p dependence) in the underlying solar wind parameters that may explain this feature. Based on previous studies (e.g. Chen and Boldyrev, 2017) we expect the steepening of the velocity spectra and it is possible that the noise floor of the FA mode data is not low enough to measure such a break scale.

Figure 7.5 shows the normalized cross helicity, residual energy and cosine of the alignment

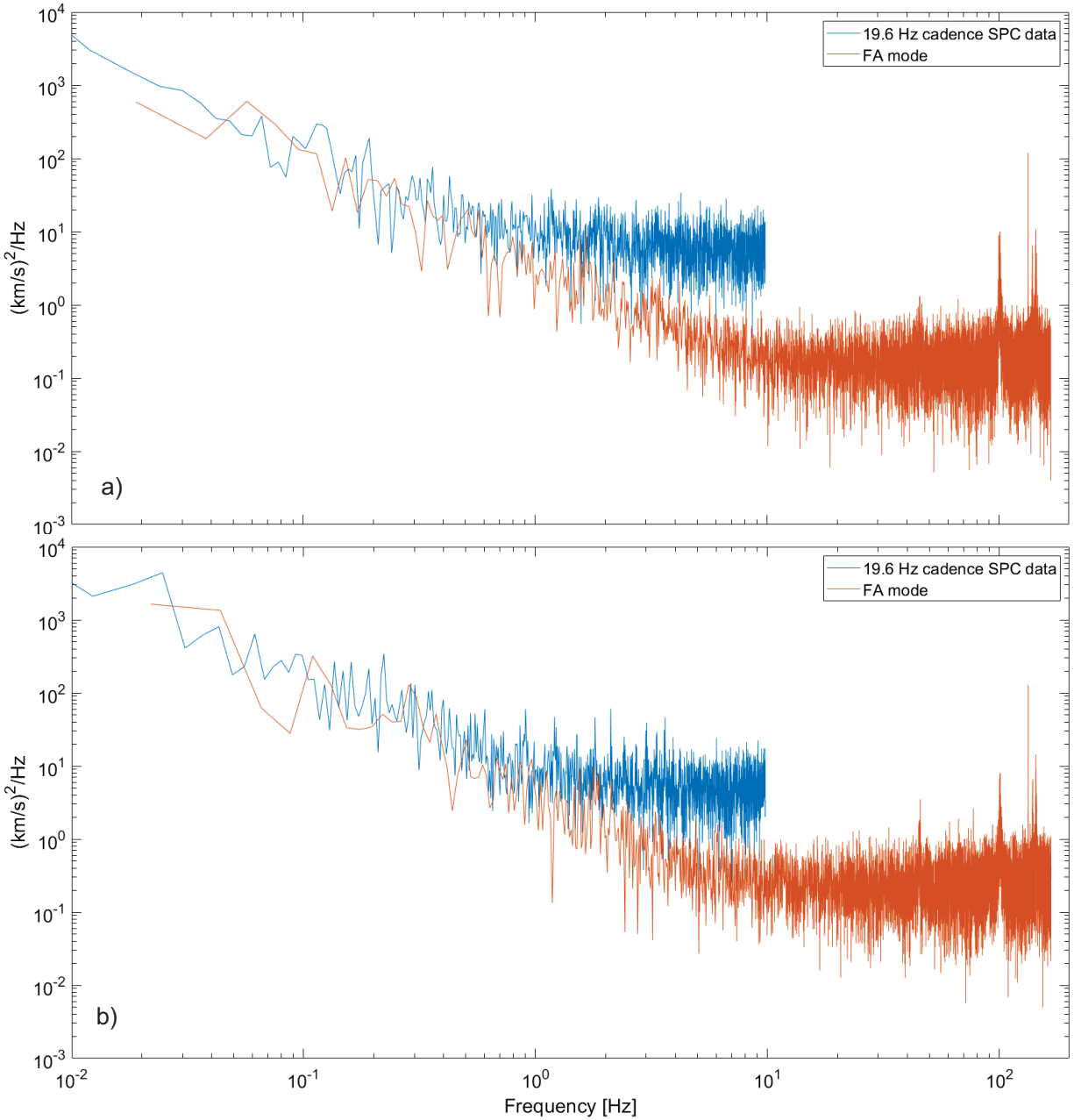

Figure 7.3: Comparison of the trace power spectrum of velocity fluctuations for the 19.6 Hz cadence data when full VDFs were measured and the FA mode data in interval #1 and #2. For frequencies below 1 Hz the FA mode data shows remarkably good agreement with the 19.6 Hz data for both intervals.

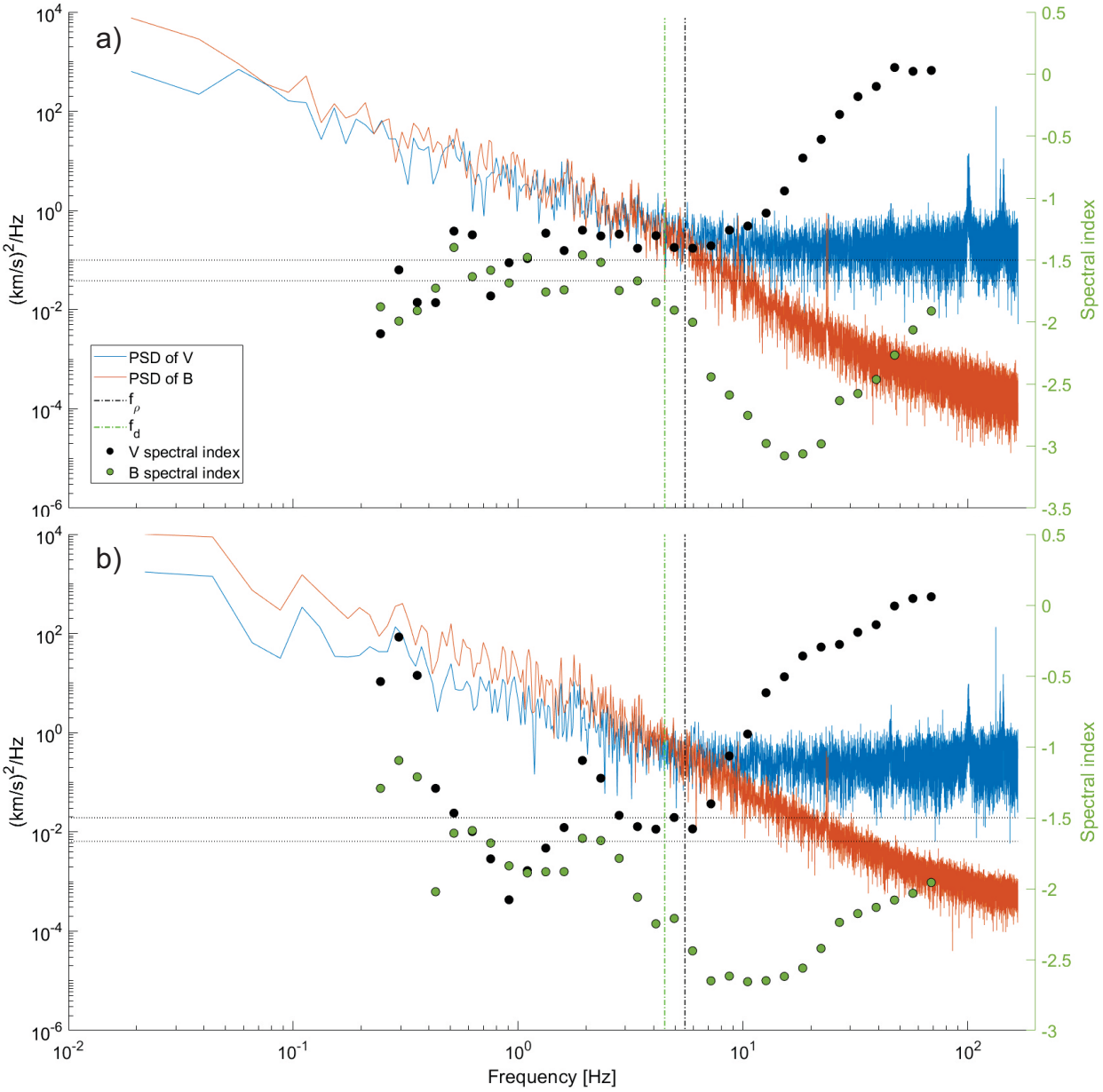

Figure 7.4: Power spectrums of velocity and magnetic field fluctuations during the first (a) and second (b) FA mode intervals, respectively.

angle. In Figure 7.5a, the normalized cross helicity shows some fluctuations in the inertial range ($\sigma_c \approx 0.4$), which is followed by a sudden decrease near the ion-scale spectral break and convergence to 0 at kinetic scales. In Figure 7.5b, the magnetic energy is larger than the energy of velocity fluctuations in the inertial range and σ_r increases gradually toward kinetic scales. Finally, Figure 7.5c suggests that the magnetic and velocity fluctuations are aligned in the inertial range and $cos(\theta) = \sigma_c/\sqrt{(1-\sigma_r^2)} = 0.5$, however this alignment drops at approximately 1.4 Hz ($\approx$ 3.1d$_i$), which is comparable to the values found by Parashar et al. (2018) in the solar wind (4.4d$_i$) at 1 AU and in the terrestrial magnetosheath (6.5d$_i$). Disruption of current sheets with the size of a few d$_i$ may affect the turbulent cascade and lead to the lack of alignment between $\delta\mathbf{v}$ and $\delta\mathbf{b}$ (see Mallet et al., 2017; Loureiro and Boldyrev, 2017; Vech et al., 2018). Another explanation for the loss of alignment is that the turbulence transitions into kinetic Alfvén range where the polarisation of the fluctuations changes and the alignment between $\delta\mathbf{b}$ and $\delta\mathbf{v}$ cease to exist (e.g. Schekochihin et al., 2009).

The sudden decrease of the cosine of the alignment angle in Figure 7.5c is close to the flattening of the proton velocity spectra hence we used the following test to quantify the effect of noise. An artificial test velocity data ($\mathbf{V}_{test}$) was computed by adding Gaussian noise to the magnetic field measurements. The amplitude of the noise was empirically chosen such that the trace power spectra of $\mathbf{V}_{test}$ is in good agreement with the real one in Figure 7.4. We calculated $cos(\theta)$ using $\mathbf{V}_{test}$ and compared it to the real measurements. We found that in the artificial test data the alignment drops to zero at a factor of 3 times higher frequency than the real measurements therefore we suggest that the observed changes of $cos(\theta)$ near the break scale are primarily physical and not caused by Gaussian noise.

7.4 Conclusion

In this Chapter, we presented the first results from the Flux Angle operation mode of the Faraday Cup instrument onboard Parker Solar Probe. This operation mode allows rapid (up to

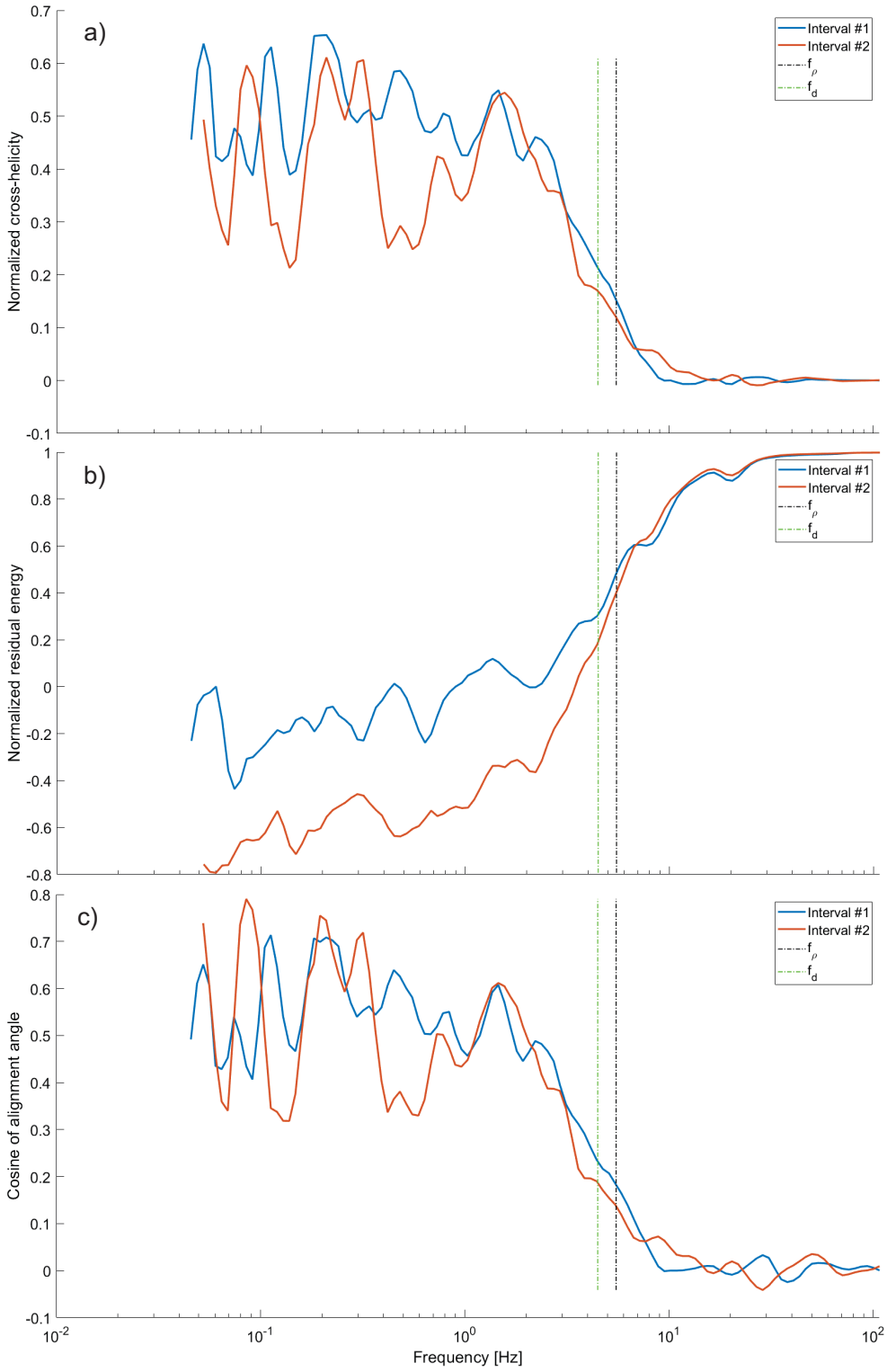

Figure 7.5: Normalized cross helicity, residual energy and cosine of the alignment angle for the first and second FA mode intervals, respectively

293 Hz) measurements of phase space density fluctuations close to the peak of the proton velocity distribution function. We described an approach to convert the measured phase space density fluctuations into vector velocity components, which were found to be reliable up to 7 Hz, which was above the ion-scale spectral break of the magnetic spectrum.

In the inertial range the velocity and magnetic power spectras were similar to the observations at 1 AU, at kinetic scales the magnetic power spectra steepened (spectral index was -2.5 / -3) while the velocity power spectra showed no clear break, which is rarely observed at 1 AU. The scaling of σ_c and σ_r in the inertial range was similar to larger statistical studies at 1 AU (Podesta et al., 2009; Parashar et al., 2018; Verdini et al., 2018): signatures of alignment between velocity and magnetic fluctuations was found in the inertial range, however near the ion-scale spectral break (at the scale of 3.4d_i) we found loss of alignment between velocity and magnetic fluctuations, which might be due to demagnetization of protons.

We expect that with decreasing perihelion distance the SPC signal-to-noise ratio will improve nearly one order of magnitude and the FA mode will be used several times each day during encounter allowing us to prepare a statistical study and investigate proton velocity fluctuations beyond ion-kinetic scales.

CHAPTER 8

Conclusion

8.1 Summary of Guiding Science Questions

This section presents a summary of the Guiding Science Questions discussed in Section 1.5. The major findings are briefly described and it is also highlighted how other researchers used these results.

Q1. How does stochastic ion heating operate in the solar wind?

We have characterized the proton and electron temperature variations as a function of gyroscale and inertial range turbulence amplitudes based on 14 years of Wind plasma and magnetic field data. The results - for the first time - revealed a critical turbulence amplitude where significant perpendicular proton heating was observed in agreement with stochastic ion heating. The variation of plasma temperature as a function of $\beta_{||}$ and turbulence amplitude was consistent with the Chandran et al. (2010) turbulence model and we found that stochastic heating operates 76% of the time at 1 AU meaning that it has a significant contribution to the non-adiabatic temperature profile of the solar wind.

The findings presented in Chapter 3 were cited by several independent researchers of the field: Parashar et al. (2018); Pezzi et al. (2019); Artemyev et al. (2019); Arzamasskiy et al. (2019); Schekochihin et al. (2018). For example, Parashar et al. (2018) conducted simulations with a fully kinetic particle-in-cell code and found that the variations of proton and electron temperature as a

function of turbulence amplitude and β are consistent with the findings in Chapter 3. Artemyev et al. (2019) presented a statistical study of solar wind measurement by the ARTEMIS spacecraft and suggested that unusually high proton-to-electron temperatures ratios ($T_i/T_e > 2$) are consistent with stochastic proton heating.

Q2. What controls the ion-scale break of the turbulent power spectrum?

We found that the Mallet et al. (2017) turbulence model may explain three major features of the transition range of the solar wind turbulence spectrum including 1) the ion-scale spectral break, 2) the steepening of the power spectra and 3) the formation of ion-scale coherent structures. The tearing mode instability may control the ion-scale spectral break in 41% of the solar wind intervals at 1 AU. The subsequent study found that the occurrence of ion-scale coherent structures overlap remarkably well with the parameter range where reconnection operates. The onset of tearing mode instability may lead to a fundamentally different route to energy dissipation than that predicted by the Kolmogorov model summarized in Chapter 1.1.

The findings presented in Chapter 5 were cited by several independent researchers of the field: Walker et al. (2018); Boldyrev and Loureiro (2018); Califano et al. (2018); Schekochihin (2019); González et al. (2019); Cerri et al. (2019); Chandran and Perez (2019); Kowal et al. (2019); Boldyrev and Loureiro (2019); Loureiro and Boldyrev (2019). For example, Loureiro and Boldyrev (2019) studied energy dissipation by reconnecting current sheets. They directly addressed the regime studied in Chapter 5 and concluded that at the ion-scale spectral break the tearing does not lead to full reconnection (e.g. the tearing does not reach the highly non-linear stage where energy conversion occurs) and therefore there may be no significant energy dissipation at those scales.

Q3. What are the capabilities of the PSP's Faraday Cup instrument to study kinetic scale velocity fluctuations?

The Flux Angle mode is a novel operation mode of PSP's Faraday Cup instrument to mea-

sure phase space density fluctuations in a narrow range of the proton velocity distribution function with 293 Hz cadence. We developed a new technique to convert these data into vector velocity components. Our approach extended the frequency range of the SPC data, which is fundamentally important since in the inner heliosphere the break scale, d_i and ρ_i are at higher frequencies (approximately 2-10 Hz in the spacecraft frame) than at 1 AU and the other operation modes of the Faraday Cup (e.g. 1.14 and 19.6 Hz cadence data) are not sufficient to measure these high frequency fluctuations. Based on the initial results from the first perihelion of PSP, we found signatures of loss of alignment between magnetic and velocity fluctuations, which might be a signature of demagnetization of protons and the onset of kinetic effects.

8.2 Future work

The advent of Parker Solar Probe offers an excellent opportunity to extend the studies presented in this dissertation.

1) Very little is known about the importance of stochastic ion heating in the inner heliosphere. As pointed out in the Conclusion of Chapter 3, the apparent correlation between proton temperature and turbulence amplitude could be a remnant of energy transfer taking place much closer to the Sun (Kasper et al., 2017) where the Alfvénic fluctuations have sufficient amplitude to break the first adiabatic invariant. Parker Solar Probe will make it possible to study the radial scaling of ϵ within 0.3 AU thus extend the work of Bourouaine and Chandran (2013).

2) Chapter 6 provided some in-direct evidence for local generation of ion-scale coherent structures, however studying the radial dependence of these structures is necessary to obtain conclusive results. We will investigate the radial dependence of the waiting times (WT, e.g. elapsed time between two consecutive ion-scale coherent structures) and compare them to the simple model suggesting that all small-scale coherent structures have solar origin (e.g the Sun/solar corona emits a certain number coherent structures, which are distributed on a sphere with increasing radius). If the WTs are found to be longer in the inner-heliosphere than expected based on the simple radial

model, then it implies that not all coherent structures could be traced back to the corona but local generation occurs as well.

3) The Flux Angle mode in Chapter 7 has a broad range of implications to characterize kinetic scale processes in the inner heliosphere. The wealth of available data will make it possible to study kinetic scale physics in magnetic switchbacks and the background solar wind. Furthermore, the Flux Angle data will be analyzed with the high frequency electric field measurements and the field-particle energy exchange will be quantified based on the approach of Chen et al. (2019). It is important to note that the Flux Angle mode can measure phase space density fluctuations at any phase speed, which means that signatures of Landau damping might be detected by measuring the VDF at approximately the proton thermal speed (in the range of 80-120 km/s phase speed).

BIBLIOGRAPHY

Alexandrova, O. (2008). Solar wind vs. magnetosheath turbulence and Alfven vortices. *Nonlin. Proc. Geophys. 15*, 95.

Alexandrova, O., J. Saur, C. Lacombe, A. Mangeney, J. Mitchell, S. J. Schwartz, and P. Robert (2009, October). Universality of solar-wind turbulent spectrum from MHD to electron scales. *Physical Review Letters 103*, 165003.

Alfvén, H. (1942). Existence of electromagnetic-hydrodynamic waves. *Nature 150*(3805), 405.

Antonucci, E., M. A. Dodero, and S. Giordano (2000). Fast solar wind velocity in a polar coronal hole during solar minimum. *Solar Physics 197*(1), 115–134.

Artemyev, A., V. Angelopoulos, I. Vasko, A. Runov, L. Avanov, B. Giles, C. Russell, and R. Strangeway (2019). On the kinetic nature of solar wind discontinuities. *Geophysical Research Letters 46*(3), 1185–1194.

Arzamasskiy, L., M. Kunz, B. Chandran, and E. Quataert (2019). Hybrid-kinetic simulations of ion heating in alfvénic turbulence. *arXiv preprint arXiv:1901.11028*.

Aschwanden, M. (2006). *Physics of the solar corona: an introduction with problems and solutions*. Springer Science & Business Media.

Balbus, S. and J. Hawley (1998). Instability, turbulence, and enhanced transport in accretion disks. *Reviews of Modern Physics 70*(1), 1.

Bale, S., K. Goetz, P. Harvey, P. Turin, J. Bonnell, T. D. De Wit, R. Ergun, R. MacDowall, M. Pulupa, M. André, et al. (2016). The fields instrument suite for solar probe plus. *Space Science Reviews 204*(1-4), 49–82.

Bale, S., P. Kellogg, F. Mozer, T. Horbury, and H. Reme (2005). Measurement of the electric fluctuation spectrum of magnetohydrodynamic turbulence. *Physical Review Letters 94*(21), 215002.

Bale, S. and the FIELDS team (2019). The Magnetic Structure and Electrodynamics of the Emerging Solar Wind. *Under Review in Nature*.

Bandyopadhyay, R., A. Chasapis, R. Chhiber, T. Parashar, B. Maruca, W. Matthaeus, S. Schwartz, S. Eriksson, O. Le Contel, H. Breuillard, et al. (2018). Solar wind turbulence studies using mms fast plasma investigation data. *The Astrophysical Journal 866*(2), 81.

Barnes, A. (1968). Collisionless heating of the solar-wind plasma. i. theory of the heating of collisionless plasma by hydromagnetic waves. *The Astrophysical Journal 154*, 751.

Biskamp, D. (2003). *Magnetohydrodynamic turbulence*. Cambridge University Press.

Boldyrev, S. (2006). Spectrum of magnetohydrodynamic turbulence. *Physical Review Letters 96*, 115002.

Boldyrev, S. and N. Loureiro (2018). Calculations in the theory of tearing instability. In *Journal of Physics: Conference Series*, Volume 1100, pp. 012003. IOP Publishing.

Boldyrev, S. and N. Loureiro (2019). Role of reconnection in inertial kinetic-alfvén turbulence. *arXiv preprint arXiv:1901.10096*.

Boldyrev, S., J. Perez, J. Borovsky, and J. J. Podesta (2011). Spectral scaling laws in magneto-hydrodynamic turbulence simulations and in the solar wind. *The Astrophysical Journal Letters 741*(1), L19.

Boldyrev, S., J. Perez, and V. Zhdankin (2012). Residual energy in mhd turbulence and in the solar wind. In *AIP Conference Proceedings*, Volume 1436, pp. 18–23. AIP.

Boldyrev, S. and J. C. Perez (2012, October). Spectrum of kinetic-Alfvén turbulence. *Astrophysical Journal Letters 758*, L44.

Borovsky, J. (2008). Flux tube texture of the solar wind: Strands of the magnetic carpet at 1 au? *Journal of Geophysical Research: Space Physics 113*(A8).

Borovsky, J. and J. Podesta (2015). Exploring the effect of current sheet thickness on the high-frequency fourier spectrum breakpoint of the solar wind. *Journal of Geophysical Research: Space Physics 120*(11), 9256–9268.

Bourouaine, S. and B. Chandran (2013). Observational test of stochastic heating in low-β fast-solar-wind streams. *The Astrophysical Journal 774*(2), 96.

Bowen, T., A. Mallet, J. Bonnell, and S. Bale (2018). Impact of residual energy on solar wind turbulent spectra. *The Astrophysical Journal 865*(1), 45.

Breech, B., W. Matthaeus, S. Cranmer, J. Kasper, and S. Oughton (2009). Electron and proton heating by solar wind turbulence. *Journal of Geophysical Research: Space Physics 114*(A9).

Bruno, R., V. Carbone, P. Veltri, E. Pietropaolo, and B. Bavassano (2001). Identifying intermittency events in the solar wind. *Planetary and Space Science 49*(12), 1201–1210.

Bruno, R. and D. Telloni (2015). Spectral analysis of magnetic fluctuations at proton scales from fast to slow solar wind. *Astrophysical Journal Letters 811*(2), L17.

Bruno, R. and L. Trenchi (2014). Radial dependence of the frequency break between fluid and kinetic scales in the solar wind fluctuations. *The Astrophysical Journal Letters 787*(2), L24.

Burlaga, L. and K. Ogilvie (1973). Solar wind temperature and speed. *Journal of Geophysical Research 78*(13), 2028–2034.

Califano, F., S. Cerri, M. Faganello, D. Laveder, and M. Kunz (2018). Electron-only magnetic reconnection in plasma turbulence. *arXiv preprint arXiv:1810.03957*.

Camporeale, E., L. Sorriso-Valvo, F. Califano, and A. Retinò (2018). Coherent structures and spectral energy transfer in turbulent plasma: a space-filter approach. *Physical Review Letters 120*(12), 125101.

Case, A. C. and the SWEAP team (2019). The Solar Probe Cup on Parker Solar Probe. *Under review in the Astrophysical Journal*.

Cerri, S., L. Franci, F. Califano, S. Landi, and P. Hellinger (2017). Plasma turbulence at ion scales: a comparison between particle in cell and eulerian hybrid-kinetic approaches. *Journal of Plasma Physics 83*(2).

Cerri, S., D. Grošelj, and L. Franci (2019). Kinetic plasma turbulence: recent insights and open questions from 3d3v simulations. *arXiv preprint arXiv:1909.11525*.

Cerri, S. S. and F. Califano (2017, February). Reconnection and small-scale fields in 2D-3V hybrid-kinetic driven turbulence simulations. *New Journal of Physics 19*, 025007.

Chandran, B. (2008). Strong anisotropic mhd turbulence with cross helicity. *The Astrophysical Journal 685*(1), 646.

Chandran, B., B. Li, B. Rogers, E. Quataert, and K. Germaschewski (2010). Perpendicular ion heating by low-frequency alfvén-wave turbulence in the solar wind. *The Astrophysical Journal 720*(1), 503.

Chandran, B. and J. Perez (2019). Reflection-driven magnetohydrodynamic turbulence in the solar atmosphere and solar wind. *Journal of Plasma Physics 85*(4).

Chandran, B. D. G., A. A. Schekochihin, and A. Mallet (2015, July). Intermittency and alignment in strong RMHD turbulence. *Astrophysical Journal 807*, 39.

Chasapis, A., A. Retinò, F. Sahraoui, A. Vaivads, Y. V. Khotyaintsev, D. Sundkvist, A. Greco, L. Sorriso-Valvo, and P. Canu (2015). Thin current sheets and associated electron heating in turbulent space plasma. *The Astrophysical Journal Letters 804*(1), L1.

Chaston, C., J. Bonnell, C. Carlson, J. McFadden, R. Ergun, R. Strangeway, and E. Lund (2004). Auroral ion acceleration in dispersive alfvén waves. *Journal of Geophysical Research: Space Physics 109*(A4).

Chen, C., S. Bale, C. Salem, and B. Maruca (2013). Residual energy spectrum of solar wind turbulence. *The Astrophysical Journal 770*(2), 125.

Chen, C. and S. Boldyrev (2017). Nature of kinetic scale turbulence in the earth's magnetosheath. *The Astrophysical Journal 842*(2), 122.

Chen, C., K. Klein, and G. Howes (2019). Evidence for electron landau damping in space plasma turbulence. *Nature communications 10*(1), 740.

Chen, C., L. Matteini, D. Burgess, and T. Horbury (2015). Magnetic field rotations in the solar wind at kinetic scales. *Monthly Notices of the Royal Astronomical Society: Letters 453*(1), L64–L68.

Chen, C., SWEAP, and FIELDS (2019). Radial evolution of solar wind turbulence from 35 RS to 1 AU. *Under review in the Astrophysical Journal*.

Chen, C. H. K. (2016, December). Recent progress in astrophysical plasma turbulence from solar wind observations. *Journal of Plasma Physics 82*, 535820602.

Chen, C. H. K., S. Boldyrev, Q. Xia, and J. C. Perez (2013). Nature of subproton scale turbulence in the solar wind. *Physical Review Letters*.

Chen, C. H. K., T. S. Horbury, A. A. Schekochihin, R. T. Wicks, O. Alexandrova, and J. Mitchell (2010). Anisotropy of solar wind turbulence between ion and electron scales. *Physical Review Letters*.

Chen, C. H. K., L. Leung, S. Boldyrev, B. A. Maruca, and S. D. Bale (2014, November). Ion-scale spectral break of solar wind turbulence at high and low beta. *Geophysical Research Letters 41*, 8081–8088.

Chen, C. H. K., A. Mallet, A. A. Schekochihin, T. S. Horbury, R. T. Wicks, and S. D. Bale (2012, October). Three-dimensional structure of solar wind turbulence. *The Astrophysical Journal 758*, 120.

Chen, C. H. K., A. Mallet, T. A. Yousef, A. A. Schekochihin, and T. S. Horbury (2011). Anisotropy of Alfvénic turbulence in the solar wind and numerical simulations. *Monthly Notices of the Royal Astronomical Society*.

Chhiber, R., A. Chasapis, R. Bandyopadhyay, T. Parashar, W. Matthaeus, B. Maruca, T. Moore, J. Burch, R. Torbert, C. Russell, et al. (2018). Higher-order turbulence statistics in the earth's magnetosheath and the solar wind using magnetospheric multiscale observations. *Journal of Geophysical Research: Space Physics 123*(12), 9941–9954.

Cho, J. and E. T. Vishniac (2000). The Anisotropy of Magnetohydrodynamic Alfvénic Turbulence. *The Astrophysical Journal*.

Coburn, J., C. Smith, B. Vasquez, J. Stawarz, and M. Forman (2012). The turbulent cascade and proton heating in the solar wind during solar minimum. *The Astrophysical Journal 754*(2), 93.

Coleman Jr, P. J. (1968). Turbulence, viscosity, and dissipation in the solar-wind plasma. *The Astrophysical Journal 153*, 371.

Cranmer, S. (2000). Ion cyclotron wave dissipation in the solar corona: The summed effect of more than 2000 ion species. *The Astrophysical Journal 532*(2), 1197.

Cranmer, S., W. Matthaeus, B. Breech, and J. Kasper (2009). Empirical constraints on proton and electron heating in the fast solar wind. *The Astrophysical Journal 702*(2), 1604.

Cranmer, S. and A. Van Ballegooijen (2003). Alfvénic turbulence in the extended solar corona: Kinetic effects and proton heating. *The Astrophysical Journal 594*(1), 573.

Cranmer, S., A. Van Ballegooijen, and R. Edgar (2007). Self-consistent coronal heating and solar wind acceleration from anisotropic magnetohydrodynamic turbulence. *The Astrophysical Journal Supplement Series 171*(2), 520.

De Pontieu, B., S. McIntosh, M. Carlsson, V. Hansteen, T. Tarbell, C. Schrijver, R. Shine, S. Tsuneta, Y. Katsukawa, K. Ichimoto, et al. (2007). Chromospheric alfvénic waves strong enough to power the solar wind. *Science 318*(5856), 1574–1577.

Dong, Y., A. Verdini, and R. Grappin (2014). Evolution of turbulence in the expanding solar wind, a numerical study. *The Astrophysical Journal 793*(2), 118.

Drake, J., M. Swisdak, T. Phan, P. Cassak, M. Shay, S. Lepri, R. Lin, E. Quataert, and T. Zurbuchen (2009). Ion heating resulting from pickup in magnetic reconnection exhausts. *Journal of Geophysical Research: Space Physics 114*(A5).

Fitzpatrick, R. (2008). Introduction to plasma physics. *The University of Texas at Austin: sn*, 242.

Fox, N., M. Velli, S. Bale, R. Decker, A. Driesman, R. Howard, J. Kasper, J. Kinnison, M. Kusterer, D. Lario, et al. (2016). The solar probe plus mission: humanity's first visit to our star. *Space Science Reviews 204*(1-4), 7–48.

Franci, L., S. Landi, L. Matteini, A. Verdini, and P. Hellinger (2016). Plasma beta dependence of the ion-scale spectral break of solar wind turbulence: high-resolution 2d hybrid simulations. *The Astrophysical Journal 833*(1), 91.

Frisch, U. (1995). *Turbulence: the legacy of AN Kolmogorov*. Cambridge university press.

Galtier, S., S. V. Nazarenko, A. C. Newell, and A. Pouquet (2000, June). A weak turbulence theory for incompressible magnetohydrodynamics. *Journal of Plasma Physics 63*, 447–488.

Gary, S., R. Hughes, and J. Wang (2016). Whistler turbulence heating of electrons and ions: Three-dimensional particle-in-cell simulations. *The Astrophysical Journal 816*(2), 102.

Gary, S. and K. Nishimura (2004). Kinetic alfvén waves: Linear theory and a particle-in-cell simulation. *Journal of Geophysical Research: Space Physics 109*(A2).

Goldreich, P. and S. Sridhar (1995). Toward a theory of interstellar turbulence. 2: Strong alfvenic turbulence. *The Astrophysical Journal*.

González, C., T. Parashar, D. Gomez, W. Matthaeus, and P. Dmitruk (2019). Turbulent electromagnetic fields at sub-proton scales: two-fluid and full-kinetic plasma simulations. *Physics of Plasmas 26*(1), 012306.

Gosling, J., H. Tian, and T. Phan (2011). Pulsed alfven waves in the solar wind. *The Astrophysical Journal Letters 737*(2), L35.

Grappin, R., A. Mangeney, and E. Marsch (1990). On the origin of solar wind mhd turbulence: Helios data revisited. *Journal of Geophysical Research: Space Physics 95*(A6), 8197–8209.

Greco, A., P. Chuychai, W. Matthaeus, S. Servidio, and P. Dmitruk (2008). Intermittent mhd structures and classical discontinuities. *Geophysical Research Letters 35*(19).

Greco, A., W. Matthaeus, S. Servidio, P. Chuychai, and P. Dmitruk (2009). Statistical analysis of discontinuities in solar wind ace data and comparison with intermittent mhd turbulence. *Astrophysical Journal Letters 691*(2), L111.

Greco, A., F. Valentini, S. Servidio, and W. Matthaeus (2012). Inhomogeneous kinetic effects related to intermittent magnetic discontinuities. *Physical Review E 86*(6), 066405.

Gruzinov, A. V. (1998). Radiative efficiency of collisionless accretion. *The Astrophysical Journal 501*(2), 787.

He, J., L. Wang, C. Tu, E. Marsch, and Q. Zong (2015). Evidence of landau and cyclotron resonance between protons and kinetic waves in solar wind turbulence. *The Astrophysical Journal Letters 800*(2), L31.

Hellinger, P., L. Matteini, Š. Štverák, P. M. Trávníček, and E. Marsch (2011). Heating and cooling of protons in the fast solar wind between 0.3 and 1 au: Helios revisited. *Journal of Geophysical Research: Space Physics 116*(A9).

Hellinger, P., P. Trávníček, J. C. Kasper, and A. J. Lazarus (2006). Solar wind proton temperature anisotropy: Linear theory and wind/swe observations. *Geophysical Research Letters 33*(9).

Hollweg, J. (1971). Nonlinear landau damping of alfvén waves. *Physical Review Letters 27*(20), 1349.

Hoppock, I. W., B. D. Chandran, K. G. Klein, A. Mallet, and D. Verscharen (2018). Stochastic proton heating by kinetic-alfvén-wave turbulence in moderately high-β plasmas. *Journal of Plasma Physics 84*(6).

Horbury, T., A. Balogh, R. Forsyth, and E. Smith (1995). Anisotropy of inertial range turbulence in the polar heliosphere. *Geophysical research letters 22*(23), 3405–3408.

Horbury, T., M. Forman, and S. Oughton (2008). Anisotropic scaling of magnetohydrodynamic turbulence. *Physical Review Letters 101*(17), 175005.

Horbury, T., L. Matteini, and D. Stansby (2018). Short, large-amplitude speed enhancements in the near-sunfast solar wind. *Monthly Notices of the Royal Astronomical Society 478*(2), 1980–1986.

Horbury, T., SWEAP, and FIELDS (2019). Sharp Alfvenic impulses in the near-Sun solar wind. *Under review in the Astrophysical Journal*.

Horbury, T., R. Wicks, and C. Chen (2012). Anisotropy in space plasma turbulence: solar wind observations. *Space Science Reviews 172*(1-4), 325–342.

Howes, G., S. Bale, K. Klein, C. Chen, C. Salem, and J. TenBarge (2012). The slow-mode nature of compressible wave power in solar wind turbulence. *The Astrophysical Journal Letters 753*(1), L19.

Howes, G. G. (2016, August). The Dynamical Generation of Current Sheets in Astrophysical Plasma Turbulence. *Astrophysical Journal Letters 827*, L28.

Howes, G. G., J. M. Tenbarge, W. Dorland, E. Quataert, A. A. Schekochihin, R. Numata, and T. Tatsuno (2011, July). Gyrokinetic Simulations of Solar Wind Turbulence from Ion to Electron Scales. *Physical Review Letters 107*(3), 035004.

Huang, J. and the SWEAP team (2019). Proton Temperature Anisotropy in the near-Sun Solar Wind. *Under review in the Astrophysical Journal*.

Hundhausen, A., S. Bame, J. Asbridge, and S. Sydoriak (1970). Solar wind proton properties: Vela 3 observations from july 1965 to june 1967. *Journal of Geophysical Research 75*(25), 4643–4657.

Iroshnikov, P. (1964). Turbulence of a conducting fluid in a strong magnetic field. *Soviet Astronomy 7*, 566.

Jian, L., C. Russell, J. Luhmann, R. Strangeway, J. Leisner, and A. Galvin (2009). Ion cyclotron waves in the solar wind observed by stereo near 1 au. *The Astrophysical Journal Letters 701*(2), L105.

Johnson, J. and C. Cheng (2001). Stochastic ion heating at the magnetopause due to kinetic alfvén waves. *Geophysical Research Letters 28*(23), 4421–4424.

Kasper, J., R. Abiad, G. Austin, M. Balat-Pichelin, S. Bale, J. Belcher, P. Berg, H. Bergner, M. Berthomier, J. Bookbinder, et al. (2016). Solar wind electrons alphas and protons (sweap) investigation: design of the solar wind and coronal plasma instrument suite for solar probe plus. *Space Science Reviews 204*(1-4), 131–186.

Kasper, J., K. Klein, T. Weber, M. Maksimovic, A. Zaslavsky, S. Bale, B. Maruca, M. Stevens, and A. Case (2017, in press). A zone of preferential heating extends tens of solar radii from sun. *The Astrophysical Journal*.

Kasper, J., A. Lazarus, J. Steinberg, K. Ogilvie, and A. Szabo (2006). Physics-based tests to identify the accuracy of solar wind ion measurements: A case study with the wind faraday cups. *Journal of Geophysical Research: Space Physics 111*(A3).

Kasper, J. C. and the SWEAP team (2019). Young Solar Wind in the Grip of the Sun's Corona. *Accepted in Nature*.

Kiyani, K., K. Osman, and S. Chapman (2015). Dissipation and heating in solar wind turbulence: from the macro to the micro and back again. *The Royal Society Publishing*.

Klein, K. and B. Chandran (2016). Evolution of the proton velocity distribution due to stochastic heating in the near-sun solar wind. *The Astrophysical Journal 820*(1), 47.

Klein, K. G. and G. G. Howes (2015). Predicted impacts of proton temperature anisotropy on solar wind turbulence. *Physics of Plasmas 22*(3), 032903.

Kohl, J., G. Noci, E. Antonucci, G. Tondello, M. Huber, S. Cranmer, L. Strachan, A. Panasyuk, L. Gardner, M. Romoli, et al. (1998). Uvcs/soho empirical determinations of anisotropic velocity distributions in the solar corona. *The Astrophysical Journal Letters 501*(1), L127.

Kolmogorov, A. N. (1941). Dissipation of energy in locally isotropic turbulence. In *Akademiia Nauk SSSR Doklady*, Volume 32, pp. 16.

Koval, A. and A. Szabo (2013). Magnetic field turbulence spectra observed by the wind spacecraft. In *AIP Conference Proceedings*, Volume 1539, pp. 211–214. AIP.

Kowal, G., D. A. Falceta-Gonçalves, A. Lazarian, and E. T. Vishniac (2019). Kelvin-helmholtz versus tearing instability: What drives turbulence in stochastic reconnection? *arXiv preprint arXiv:1909.09179*.

Kraichnan, R. H. (1967). Inertial ranges in two-dimensional turbulence. *The Physics of Fluids 10*(7), 1417–1423.

Kulsrud, R. and E. Zweibel (2008). On the origin of cosmic magnetic fields. *Reports on Progress in Physics 71*(4), 046901.

Landau, L. (1946). On the vibrations of the electronic plasma. *Zh. Eksp. Teor. Fiz. 10*, 25.

Leamon, R., C. Smith, N. Ness, W. Matthaeus, and H. Wong (1998). Observational constraints on the dynamics of the interplanetary magnetic field dissipation range. *Journal of Geophysical Research: Space Physics 103*(A3), 4775–4787.

Leamon, R., C. Smith, N. Ness, and H. Wong (1999). Dissipation range dynamics: Kinetic alfvén waves and the importance of β e. *Journal of Geophysical Research: Space Physics 104*(A10), 22331–22344.

Lepping, R., M. Acũna, L. Burlaga, W. Farrell, J. Slavin, K. Schatten, F. Mariani, N. Ness, F. Neubauer, Y. Whang, et al. (1995). The wind magnetic field investigation. *Space Science Reviews 71*(1-4), 207–229.

Lin, R., K. Anderson, S. Ashford, C. Carlson, D. Curtis, R. Ergun, D. Larson, J. McFadden, M. McCarthy, G. Parks, et al. (1995). A three-dimensional plasma and energetic particle investigation for the wind spacecraft. *Space Science Reviews 71*(1), 125–153.

Lion, S., O. Alexandrova, and A. Zaslavsky (2016, June). Coherent events and spectral shape at ion kinetic scales in the fast solar wind turbulence. *The Astrophysical Journal 824*, 47.

Loureiro, N. and S. Boldyrev (2019). Nonlinear reconnection in magnetized turbulence. *arXiv preprint arXiv:1907.09610*.

Loureiro, N. F. and S. Boldyrev (2017). Collisionless reconnection in magnetohydrodynamic and kinetic turbulence. *The Astrophysical Journal 850*(2), 182.

Mallet, A. and A. Schekochihin (2016). A statistical model of three-dimensional anisotropy and intermittency in strong alfvénic turbulence. *Monthly Notices of the Royal Astronomical Society 466*(4), 3918–3927.

Mallet, A., A. Schekochihin, and B. Chandran (2017). Disruption of alfvnic turbulence by magnetic reconnection in a collisionless plasma. *Journal of Plasma Physics 83*, 905830609.

Mallet, A. and A. A. Schekochihin (2017). A statistical model of three-dimensional anisotropy and intermittency in strong alfvénic turbulence. *Monthly Notices of the Royal Astronomical Society 466*, 3918.

Mallet, A., A. A. Schekochihin, B. D. G. Chandran, C. H. K. Chen, T. S. Horbury, R. T. Wicks, and C. C. Greenan (2016, June). Measures of three-dimensional anisotropy and intermittency in strong Alfvénic turbulence. *MNRAS 459*, 2130.

Markovskii, S. and B. Vasquez (2010). The effect of spectral anisotropy of fast magnetosonic turbulence on the plasma heating at the proton kinetic scales. *Physics of Plasmas 17*(11), 112902.

Markovskii, S., B. Vasquez, and C. Smith (2008). Statistical analysis of the high-frequency spectral break of the solar wind turbulence at 1 au. *The Astrophysical Journal 675*(2), 1576.

Maron, J. and P. Goldreich (2001). Simulations of incompressible magnetohydrodynamic turbulence. *The Astrophysical Journal 554*(2), 1175.

Marsch, E. (2006). Kinetic physics of the solar corona and solar wind. *Living Reviews in Solar Physics 3*(1), 1.

Marsch, E., X. Ao, and C. Tu (2004). On the temperature anisotropy of the core part of the proton velocity distribution function in the solar wind. *Journal of Geophysical Research: Space Physics 109*(A4).

Martinez, D., S. Chen, G. Doolen, R. Kraichnan, L. Wang, and Y. Zhou (1997). Energy spectrum in the dissipation range of fluid turbulence. *Journal of Plasma Physics 57*(1), 195–201.

Mason, J., F. Cattaneo, and S. Boldyrev (2006). Dynamic alignment in driven magnetohydrodynamic turbulence. *Physical Review Letters 97*(25), 255002.

Matteini, L., O. Alexandrova, C. Chen, and C. Lacombe (2016). Electric and magnetic spectra from mhd to electron scales in the magnetosheath. *Monthly Notices of the Royal Astronomical Society 466*(1), 945–951.

Matthaeus, W., B. Breech, P. Dmitruk, A. Bemporad, G. Poletto, M. Velli, and M. Romoli (2007). Density and magnetic field signatures of interplanetary 1/f noise. *The Astrophysical Journal Letters 657*(2), L121.

Matthaeus, W. and M. Goldstein (1982). Measurement of the rugged invariants of magnetohydrodynamic turbulence in the solar wind. *Journal of Geophysical Research: Space Physics 87*(A8), 6011–6028.

Matthaeus, W. and M. Goldstein (1986). Low-frequency 1 f noise in the interplanetary magnetic field. *Physical Review Letters 57*(4), 495.

Matthaeus, W. and S. Lamkin (1986). Turbulent magnetic reconnection. *The Physics of Fluids 29*(8), 2513–2534.

Matthaeus, W., S. Oughton, K. Osman, S. Servidio, M. Wan, S. Gary, M. Shay, F. Valentini, V. Roytershteyn, H. Karimabadi, et al. (2014). Nonlinear and linear timescales near kinetic scales in solar wind turbulence. *The Astrophysical Journal 790*(2), 155.

Matthaeus, W., T. Parashar, M. Wan, and P. Wu (2016). Turbulence and proton-electron heating in kinetic plasma. *The Astrophysical Journal Letters 827*(1), L7.

Matthaeus, W., A. Pouquet, P. Mininni, P. Dmitruk, and B. Breech (2008). Rapid alignment of velocity and magnetic field in magnetohydrodynamic turbulence. *Physical Review Letters 100*(8), 085003.

Matthaeus, W. and M. Velli (2011). Who needs turbulence? *Space science reviews 160*(1-4), 145.

McChesney, J., R. Stern, and P. Bellan (1987). Observation of fast stochastic ion heating by drift waves. *Physical Review Letters 59*(13), 1436.

McComas, D., N. Alexander, N. Angold, S. Bale, C. Beebe, B. Birdwell, M. Boyle, J. Burgum, J. Burnham, E. Christian, et al. (2016). Integrated science investigation of the sun (isis): Design of the energetic particle investigation. *Space Science Reviews 204*(1-4), 187–256.

McKee, C. and E. Ostriker (2007). Theory of star formation. *Annu. Rev. Astron. Astrophys. 45*, 565–687.

Miao, B., B. Peng, and G. Li (2011). Current sheets from ulysses observation. In *Annales Geophysicae*, Volume 29, pp. 237. Copernicus GmbH.

Mistry, R., J. Eastwood, T. Phan, and H. Hietala (2017). Statistical properties of solar wind reconnection exhausts. *Journal of Geophysical Research: Space Physics*.

Miyamoto, K. (2006). *Plasma physics and controlled nuclear fusion*, Volume 38. Springer Science & Business Media.

Montgomery, D. and L. Turner (1981). Anisotropic magnetohydrodynamic turbulence in a strong external magnetic field. *The Physics of Fluids 24*(5), 825–831.

Myers, R. and R. Myers (1990). *Classical and modern regression with applications*, Volume 2. Duxbury press Belmont, CA.

Ogilvie, K., D. Chornay, R. Fritzenreiter, F. Hunsaker, J. Keller, J. Lobell, G. Miller, J. Scudder, E. Sittler, R. Torbert, et al. (1995). Swe, a comprehensive plasma instrument for the wind spacecraft. *Space Science Reviews 71*(1), 55–77.

Osman, K., W. Matthaeus, J. Gosling, A. Greco, S. Servidio, B. Hnat, S. C. Chapman, and T. Phan (2014). Magnetic reconnection and intermittent turbulence in the solar wind. *Physical Review Letters 112*(21), 215002.

Osman, K., W. Matthaeus, A. Greco, and S. Servidio (2010). Evidence for inhomogeneous heating in the solar wind. *The Astrophysical Journal Letters 727*(1), L11.

Osman, K., W. Matthaeus, B. Hnat, and S. Chapman (2012). Kinetic signatures and intermittent turbulence in the solar wind plasma. *Physical Review Letters 108*(26), 261103.

Parashar, T., A. Chasapis, R. Bandyopadhyay, R. Chhiber, W. Matthaeus, B. Maruca, M. Shay, J. Burch, T. Moore, B. Giles, et al. (2018). Kinetic range spectral features of cross helicity using the magnetospheric multiscale spacecraft. *Physical Review Letters 121*(26), 265101.

Parashar, T., M. Shay, P. Cassak, and W. Matthaeus (2009). Kinetic dissipation and anisotropic heating in a turbulent collisionless plasma. *Physics of Plasmas 16*(3), 032310.

Parashar, T. N., SWEAP, and FIELDS (2019). Alfvenicity in PSP Measurements: Comparing Different Measures. *Under review in the Astrophysical Journal*.

Perez, J. and B. Chandran (2013). Direct numerical simulations of reflection-driven, reduced magnetohydrodynamic turbulence from the sun to the alfvén critical point. *The Astrophysical Journal 776*(2), 124.

Perri, S., M. Goldstein, J. Dorelli, and F. Sahraoui (2012). Detection of small-scale structures in the dissipation regime of solar-wind turbulence. *Physical Review Letters 109*(19), 191101.

Perrone, D., O. Alexandrova, A. Mangeney, M. Maksimovic, C. Lacombe, V. Rakoto, J. C. Kasper, and D. Jovanovic (2016, August). Compressive coherent structures at ion scales in the slow solar wind. *The Astrophysical Journal 826*, 196.

Perrone, D., O. Alexandrova, O. Roberts, S. Lion, C. Lacombe, A. Walsh, M. Maksimovic, and I. Zouganelis (2017). Coherent structures at ion scales in fast solar wind: Cluster observations. *The Astrophysical Journal 849*(1), 49.

Pezzi, O., D. Perrone, S. Servidio, F. Valentini, L. Sorriso-Valvo, and P. Veltri (2019). Proton-proton collisions in the turbulent solar wind: Hybrid boltzmann-maxwell simulations. *arXiv preprint arXiv:1903.03398*.

Phan, T., J. Eastwood, M. Shay, J. Drake, B. Ö. Sonnerup, M. Fujimoto, P. Cassak, M. Øieroset, J. Burch, R. Torbert, et al. (2018). Electron magnetic reconnection without ion coupling in earths turbulent magnetosheath. *Nature 557*(7704), 202.

Podesta, J. and A. Bhattacharjee (2010). Theory of incompressible magnetohydrodynamic turbulence with scale-dependent alignment and cross-helicity. *The Astrophysical Journal 718*(2), 1151.

Podesta, J., B. Chandran, A. Bhattacharjee, D. Roberts, and M. Goldstein (2009). Scale-dependent angle of alignment between velocity and magnetic field fluctuations in solar wind turbulence. *Journal of Geophysical Research: Space Physics 114*(A1).

Podesta, J., D. Roberts, and M. Goldstein (2007). Spectral exponents of kinetic and magnetic energy spectra in solar wind turbulence. *The Astrophysical Journal 664*(1), 543.

Podesta, J. J. (2009, June). Dependence of Solar-Wind Power Spectra on the Direction of the Local Mean Magnetic Field. *Astrophys. J. 698*, 986–999.

Politano, H., A. Pouquet, and P. Sulem (1989). Small scale dynamics of an incompressible mhd flow. In *Turbulence and Nonlinear Dynamics in MHD Flows*, pp. 233–240.

Pollock, C., T. Moore, A. Jacques, J. Burch, U. Gliese, Y. Saito, T. Omoto, L. Avanov, A. Barrie, V. Coffey, et al. (2016). Fast plasma investigation for magnetospheric multiscale. *Space Science Reviews 199*(1-4), 331–406.

Pope, S. (2001). *Turbulent flows*. IOP Publishing.

Pulupa, M., S. Bale, C. Salem, and K. Horaites (2014). Spin-modulated spacecraft floating potential: Observations and effects on electron moments. *Journal of Geophysical Research: Space Physics 119*(2), 647–657.

Quataert, E. (1998). Particle heating by alfvenic turbulence in hot accretion flows. *The Astrophysical Journal 500*(2), 978.

Retinò, A., D. Sundkvist, A. Vaivads, F. Mozer, M. André, and C. Owen (2007). In situ evidence of magnetic reconnection in turbulent plasma. *Nature Phys. 3*, 236.

Reynolds, O. (1883). Xxix. an experimental investigation of the circumstances which determine whether the motion of water shall be direct or sinuous, and of the law of resistance in parallel channels. *Philosophical Transactions of the Royal society of London* (174), 935–982.

Riazantseva, M., V. Budaev, L. Rakhmanova, G. Zastenker, Y. Yermolaev, I. Lodkina, J. Šafránková, Z. Němeček, and L. Přech (2017). Variety of shapes of solar wind ion flux spectra: Spektr-r measurements. *Journal of Plasma Physics 83*(4).

Richardson, J. and C. Smith (2003). The radial temperature profile of the solar wind. *Geophysical Research Letters 30*(5).

Richardson, L. F. (1922, July). Weather prediction by numerical process. *Quarterly Journal of the Royal Meteorological Society 48*, 282–284.

Roberts, O., X. Li, O. Alexandrova, and B. Li (2016). Observation of an mhd alfvén vortex in the slow solar wind. *Journal of Geophysical Research: Space Physics 121*(5), 3870–3881.

Šafránková, J., Z. Němeček, F. Němec, L. Přech, C. Chen, and G. Zastenker (2016). Power spectral density of fluctuations of bulk and thermal speeds in the solar wind. *The Astrophysical Journal 825*(2), 121.

Šafránková, J., Z. Němeček, F. Němec, L. Přech, A. Pitňa, C. Chen, and G. Zastenker (2015). Solar wind density spectra around the ion spectral break. *The Astrophysical Journal 803*(2), 107.

Šafránková, J., Z. Němeček, L. Přech, and G. Zastenker (2013). Ion kinetic scale in the solar wind observed. *Physical Review Letters 110*(2), 025004.

Šafránková, J., Z. Němeček, L. Přech, G. Zastenker, I. Čermák, L. Chesalin, A. Komárek, J. Vaverka, M. Beránek, J. Pavl, et al. (2013). Fast solar wind monitor (bmsw): Description and first results. *Space Science Reviews 175*(1-4), 165–182.

Sahraoui, F., M. L. Goldstein, G. Belmont, P. Canu, and L. Rezeau (2010). Three dimensional anisotropic k spectra of turbulence at subproton scales in the solar wind. *Physical Review Letters*.

Sahraoui, F., M. L. Goldstein, P. Robert, and Y. V. Khotyaintsev (2009). Evidence of a cascade and dissipation of solar-wind turbulence at the electron gyroscale. *Physical Review Letters 102*, 231102.

Saito, S., S. Gary, H. Li, and Y. Narita (2008). Whistler turbulence: Particle-in-cell simulations. *Physics of Plasmas 15*(10), 102305.

Salem, C., A. Mangeney, S. Bale, and P. Veltri (2009). Solar wind magnetohydrodynamics turbulence: anomalous scaling and role of intermittency. *The Astrophysical Journal 702*(1), 537.

Schekochihin, A., S. Cowley, W. Dorland, G. Hammett, G. Howes, E. Quataert, and T. Tatsuno (2009). Astrophysical gyrokinetics: kinetic and fluid turbulent cascades in magnetized weakly collisional plasmas. *The Astrophysical Journal Supplement Series 182*(1), 310.

Schekochihin, A., S. Cowley, R. Kulsrud, M. Rosin, and T. Heinemann (2008). Nonlinear growth of firehose and mirror fluctuations in astrophysical plasmas. *Physical Review Letters 100*(8), 081301.

Schekochihin, A., Y. Kawazura, and M. Barnes (2018). Constraints on ion vs. electron heating by plasma turbulence at low beta. *arXiv preprint arXiv:1812.09792*.

Schekochihin, A. A. (2019). Mhd turbulence: a biased review. *Journal of Plasma Physics 45*.

Schekochihin, A. A., S. C. Cowley, W. Dorland, G. W. Hammett, G. G. Howes, E. Quataert, and T. Tatsuno (2009, May). Astrophysical gyrokinetics: kinetic and fluid turbulent cascades in magnetized weakly collisional plasmas. *Astrophysical Journal Supplements 182*, 310.

Schwartz, S., W. Feldman, and S. Gary (1981). The source of proton anisotropy in the high-speed solar wind. *Journal of Geophysical Research: Space Physics 86*(A2), 541–546.

Servidio, S., A. Greco, W. Matthaeus, K. Osman, and P. Dmitruk (2011). Statistical association of discontinuities and reconnection in magnetohydrodynamic turbulence. *Journal of Geophysical Research: Space Physics 116*(A9).

Servidio, S., W. Matthaeus, M. Shay, P. Cassak, and P. Dmitruk (2009). Magnetic reconnection in two-dimensional magnetohydrodynamic turbulence. *Physical review letters 102*(11), 115003.

Servidio, S., F. Valentini, F. Califano, and P. Veltri (2012). Local kinetic effects in two-dimensional plasma turbulence. *Physical Review Letters 108*(4), 045001.

Smith, C., K. Hamilton, B. Vasquez, and R. Leamon (2006). Dependence of the dissipation range spectrum of interplanetary magnetic fluctuationson the rate of energy cascade. *The Astrophysical Journal Letters 645*(1), L85.

Sonnerup, B. and L. Cahill (1967). Magnetopause structure and attitude from explorer 12 observations. *Journal of Geophysical Research 72*(1), 171–183.

Sorriso-Valvo, L., F. Carbone, S. Perri, A. Greco, R. Marino, and R. Bruno (2018). On the statistical properties of turbulent energy transfer rate in the inner heliosphere. *Solar Physics 293*(1), 10.

Sorriso-Valvo, L., V. Carbone, P. Veltri, G. Consolini, and R. Bruno (1999). Intermittency in the solar wind turbulence through probability distribution functions of fluctuations. *Geophysical Research Letters 26*(13), 1801–1804.

Stawicki, O., S. Gary, and H. Li (2001). Solar wind magnetic fluctuation spectra: Dispersion versus damping. *Journal of Geophysical Research: Space Physics 106*(A5), 8273–8281.

Sundkvist, D., A. Retinò, A. Vaivads, and S. Bale (2007). Dissipation in turbulent plasma due to reconnection in thin current sheets. *Physical Review Letters 99*(2), 025004.

Taylor, G. (1938). The spectrum of turbulence. *Proceedings of the Royal Society of London. Series A-Mathematical and Physical Sciences 164*(919), 476–490.

Telloni, D. and R. Bruno (2016). Linking fluid and kinetic scales in solar wind turbulence. *Monthly Notices of the Royal Astronomical Society: Letters 463*(1), L79–L83.

TenBarge, J. and G. Howes (2012). Evidence of critical balance in kinetic alfvén wave turbulence simulations. *Physics of Plasmas 19*(5), 055901.

Uzdensky, D. and N. Loureiro (2016). Magnetic reconnection onset via disruption of a forming current sheet by the tearing instability. *Physical Review Letters 116*(10), 105003.

van der Holst, B., I. Sokolov, X. Meng, M. Jin, W. Manchester IV, G. Tóth, and T. Gombosi (2014). Alfvén wave solar model (awsom): coronal heating. *The Astrophysical Journal 782*(2), 81.

Vasquez, B., V. Abramenko, D. Haggerty, and C. Smith (2007). Numerous small magnetic field discontinuities of bartels rotation 2286 and the potential role of alfvénic turbulence. *Journal of Geophysical Research: Space Physics 112*(A11).

Vassilicos, J. (2015). Dissipation in turbulent flows. *Annual Review of Fluid Mechanics 47*, 95–114.

Vech, D. and C. Chen (2016). Testing the effects of expansion on solar wind turbulence. *Astrophysical Journal Letters 832*(1), L16.

Vech, D., K. Klein, and J. Kasper (2017). Nature of stochastic ion heating in the solar wind: testing the dependence on plasma beta and turbulence amplitude. *The Astrophysical Journal Letters 850*(1), L11.

Vech, D., A. Mallet, K. Klein, and J. Kasper (2018). Magnetic reconnection may control the ion-scale spectral break of solar wind turbulence. *The Astrophysical Journal Letters 855*(2), L27.

Velli, M., R. Grappin, and A. Mangeney (1989). Turbulent cascade of incompressible unidirectional alfvén waves in the interplanetary medium. *Physical Review Letters 63*(17), 1807.

Verdini, A. and R. Grappin (2015, August). Imprints of expansion on the local anisotropy of solar wind turbulence. *Astrophys. J. Lett. 808*, L34.

Verdini, A., R. Grappin, O. Alexandrova, and S. Lion (2018). 3d anisotropy of solar wind turbulence, tubes, or ribbons? *The Astrophysical Journal 853*(1), 85.

Verdini, A. and M. Velli (2007). Alfvén waves and turbulence in the solar atmosphere and solar wind. *The Astrophysical Journal 662*(1), 669.

Voitenko, Y. and M. Goossens (2004). Cross-field heating of coronal ions by low-frequency kinetic alfvén waves. *The Astrophysical Journal Letters 605*(2), L149.

Vourlidas, A., R. A. Howard, S. Plunkett, C. Korendyke, A. Thernisien, D. Wang, N. Rich, M. Carter, D. Chua, D. Socker, et al. (2016). The wide-field imager for solar probe plus (wispr). *Space Science Reviews 204*(1-4), 83–130.

Walker, J., S. Boldyrev, and N. Loureiro (2018). Influence of tearing instability on magnetohydrodynamic turbulence. *Physical Review E 98*(3), 033209.

Wan, M., W. Matthaeus, V. Roytershteyn, H. Karimabadi, T. Parashar, P. Wu, and M. Shay (2015). Intermittent dissipation and heating in 3d kinetic plasma turbulence. *Physical Review Letters 114*(17), 175002.

Wan, M., W. Matthaeus, V. Roytershteyn, T. Parashar, P. Wu, and H. Karimabadi (2016). Intermittency, coherent structures and dissipation in plasma turbulence. *Physics of Plasmas 23*(4), 042307.

Wang, T., O. Alexandrova, D. Perrone, M. Dunlop, X. Dong, R. Bingham, Y. Khotyaintsev, C. Russell, B. Giles, R. Torbert, et al. (2019). Magnetospheric multiscale observation of kinetic signatures in the alfvén vortex. *The Astrophysical Journal Letters 871*(2), L22.

Wang, X., C. Tu, J. He, E. Marsch, and L. Wang (2013). On intermittent turbulence heating of the solar wind: differences between tangential and rotational discontinuities. *The Astrophysical Journal Letters 772*(2), L14.

Wang, X., C. Tu, J. He, and L. Wang (2018). Ion-scale spectral break in the normal plasma beta range in the solar wind turbulence. *Journal of Geophysical Research: Space Physics*.

Wang, Y., S. Boldyrev, and J. Perez (2011). Residual energy in magnetohydrodynamic turbulence. *The Astrophysical Journal Letters 740*(2), L36.

Wicks, R., R. Alexander, M. Stevens, L. Wilson III, P. Moya, A. Viñas, L. Jian, D. Roberts, S. OModhrain, J. Gilbert, et al. (2016). A proton-cyclotron wave storm generated by unstable proton distribution functions in the solar wind. *The Astrophysical Journal 819*(1), 6.

Wicks, R., T. Horbury, C. Chen, and A. Schekochihin (2010). Power and spectral index anisotropy of the entire inertial range of turbulence in the fast solar wind. *Monthly Notices of the Royal Astronomical Society: Letters 407*(1), L31–L35.

Wicks, R., T. Horbury, C. Chen, and A. Schekochihin (2011). Anisotropy of imbalanced alfvénic turbulence in fast solar wind. *Physical Review Letters 106*(4), 045001.

Wicks, R. T., D. A. Roberts, A. Mallet, A. A. Schekochihin, T. S. Horbury, and C. H. K. Chen (2013, December). Correlations at Large Scales and the Onset of Turbulence in the Fast Solar Wind. *The Astrophysical Journal 778*, 177.

Wilson III, L., M. Stevens, J. Kasper, K. Klein, B. Maruca, S. Bale, T. Bowen, M. Pulupa, and C. Salem (2018). The statistical properties of solar wind temperature parameters near 1 au. *The Astrophysical Journal Supplement Series 236*(2), 41.

Wolfe, J., R. Silva, and M. Myers (1966). Observations of the solar wind during the flight of imp 1. *Journal of Geophysical Research 71*(5), 1319–1340.

Woodham, L. D., R. T. Wicks, D. Verscharen, and C. J. Owen (2018). The Role of Proton-Cyclotron Resonance as a Dissipation Mechanism in Solar Wind Turbulence: A Statistical Study at Ion-Kinetic Scales. *ArXiv e-prints*.

Wu, P., M. Wan, W. Matthaeus, M. Shay, and M. Swisdak (2013). von kármán energy decay and heating of protons and electrons in a kinetic turbulent plasma. *Physical Review Letters 111*(12), 121105.

Xia, Q., J. Perez, B. Chandran, and E. Quataert (2013). Perpendicular ion heating by reduced magnetohydrodynamic turbulence. *The Astrophysical Journal 776*(2), 90.

Yamada, M., R. Kulsrud, and H. Ji (2010). Magnetic reconnection. *Reviews of Modern Physics 82*(1), 603.

Zhdankin, V., S. Boldyrev, and C. H. K. Chen (2016, March). Intermittency of energy dissipation in Alfvénic turbulence. *Mon. Not. R. Astron. Soc. 457*, L69.

Zhdankin, V., S. Boldyrev, and J. Mason (2012). Distribution of magnetic discontinuities in the solar wind and in magnetohydrodynamic turbulence. *The Astrophysical Journal Letters 760*(2), L22.

Zhdankin, V., D. A. Uzdensky, J. C. Perez, and S. Boldyrev (2013, July). Statistical analysis of current sheets in three-dimensional magnetohydrodynamic turbulence. *The Astrophysical Journal 771*, 124.

Zheng, J. and Q. Hu (2018). Observational evidence for self-generation of small-scale magnetic flux ropes from intermittent solar wind turbulence. *Astrophysical Journal Letters 852*(2), L23.